Effects of Foreign Object Damage on Fatigue Behavior of Two Metallic Materials used in a Concentrating Solar Power Plant

by

Nirmal Dobaria

A Thesis Presented in Partial Fulfillment
of the Requirements for the Degree
Master of Science

Approved November 2016 by the
Graduate Supervisory Committee:

Pedro Peralta, Chair
Kiran Solanki
Karl Sieradzki

ARIZONA STATE UNIVERSITY

December 2016

ABSTRACT

Structural stability and performance of structural materials is important for energy production, whether renewable or non renewable, to have uninterrupted energy supply, that is economically feasible and safe. High temperature metallic materials used in the turbines of AORA, an Israel-based clean energy producer, often experience high temperature, high stress and foreign object damage (FOD). In this study, efforts were made to study the effects of FOD on the fatigue life of these materials and to understand their failure mechanisms. The foreign objects/debris recovered by AORA were characterized using Powder X-ray Diffraction (XRD) and Energy Dispersive Spectroscopy (EDS) to identify composition and phases. To perform foreign object damage experiment a gas gun was built and results of XRD and EDS were used to select particles to mimic FOD in lab experiments for two materials of interest to AORA: Hastelloy X and SS 347. Electron Backscattering Diffraction, hardness and tensile tests were also performed to characterize microstructure and mechanical properties. Fatigue tests using at high temperature were performed on dog bone samples with and without FOD and the fracture surfaces and well as the regions affected by FOD were analyzed using Scanning Electron Microscopy (SEM) to understand the failure mechanism. The findings of these study indicate that FOD is causing multiple secondary cracks at and around the impact sites, which can potentially grow to coalesce and remove pieces of material, and the multisite damage could also lead to lower fatigue lives, despite the fact that the FOD site was not always the most favorable for initiation of the fatal fatigue crack. It was also seen by the effect of FOD on fatigue life that SS 347 is more susceptible to FOD than Hastelloy X.

ACKNOWLEDGMENTS

Firstly, I would like to express my deepest gratitude to my advisor Dr. Pedro Peralta, for constant guidance and support he has given in my work. I have evolved in many ways as a student, an engineer, a person and the valuable lessons learned working under him will stay forever. I would also like to thank Harn Lim, Robert McDonald, Jay Patel and all the lab members for helping me in my work. Many thanks to Dr. Dallas Kingsbury for the support in running my experiments.

We gratefully acknowledge the use of facilities with the LeRoyEyring Center for Solid State Science at Arizona State University.

TABLE OF CONTENTS

Page

CHAPTER Page

CHAPTER Page

APPENDIX

LIST OF TABLES

LIST OF FIGURES

Figure Page

Figure Page

Figure Page

Figure Page

Figure Page

Figure Page

Figure Page

Figure Page

Figure Page

1. INTRODUCTION

1.1 Solar Power

Current climate change is being driven by the ever-increasing CO_2 in the atmosphere, 90% of this is due to burning of fossil fuels for power generation and transportation [1]. This escalating build up of carbon dioxide in the atmosphere has resulted in a rise of the average temperature of the Earth, melting of polar ice and extreme climatic conditions in various parts of the world [1]. Consequently many people, especially in under developed countries, have a risk of hunger, water scarcity, flooding, desertification etc. Although oil prices have plummeted for the past year, petroleum prices are projected to move forward over $215/barrel in 2035 and its use is expecting to increase, especially by developing countries; hence, the CO_2 emission and associated dangers are going to worsen [1]. Catastrophic nuclear and radiation events in past has pushed many countries to review their policies for using nuclear energy. For all these reasons more countries are agreeing to the idea that a part of electric power generation be from renewable sources, specifically solar energy[1].

Energy is essential for all forms of life and the sun is the most important and abundant source of energy available to human kind, there is no life possible without it. This solar energy is partly or wholly responsible for all other forms of energy like geothermal energy, tidal energy, wind energy, etc., as each are derived indirectly from the sun [2]. The sun's energy is produced by a fusion nuclear reaction between three single hydrogen nuclei to form helium and is available to the Earth's surface in the form of electromagnetic radiation [2]. This energy can be used to generate electricity by exploiting, e.g., the electromagnetic energy present in the sun's radiation. Each year an average of 3,400,000 exajoule (EJ) of sun's radiation is directed towards the

earth by sun, out of which 6% is reflected by atmosphere, 20% is reflected by clouds, 4% is reflected by the earth's surface, 16% is absorbed by atmosphere, 3% is absorbed by clouds and 51% is absorbed by the earth's surface and water[3]. If 0.1% of this energy could be converted to electricity with 10% efficiency, it would generate four times the electricity than is globally produced [3].

Due to the ever-increasing demand of energy and not enough supply, humans have started looking for alternative sources of energy production since long ago. The total consumption of energy in the world is predicted to increase by 44% from 2006 to 2030, as shown in Figure 1 [4].

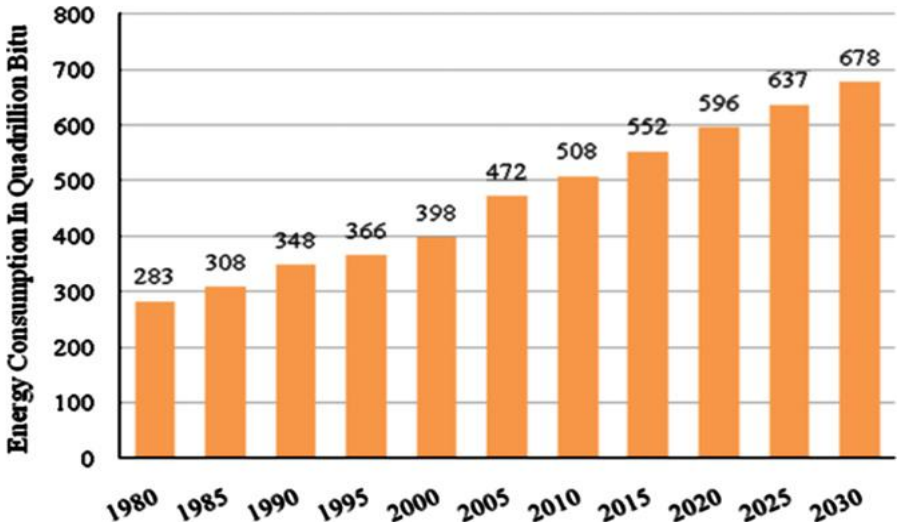

Figure 1. World marketed energy consumption 1980–2030[4].

Early attempts to apply solar energy to generate electricity were made in 19th century by using parabolic reflectors to concentrate the sun's energy to run a steam engine. The early attempts did not help in materializing the efforts and saw setback as it was related to the fluctuating market energy prices, which plummeted later on[2]. However, the oil crisis of the 1970s caused the world to undertake efforts to push

research and development in solar energy power generation [5]. With advancements in research and increased understanding, scientists and researchers have been able to harness the power of the sun to convert it to electricity in many different ways. There are two main ways to capture sunlight and use it as an energy source to generate electricity. The first one is solar thermal generation where the sun is used primarily as a source of heat [6]. In solar thermal energy the sun's heat energy is captured, concentrated and used to drive a heat engine. This heat engine could be a gas turbine, steam turbine or Stirling engine [7]. The second is by using photovoltaic or solar cells, which are solid state devices made of semiconducting materials exhibiting the photovoltaic effect, which converts sunlight directly into electricity [4]. Each of these two ways can be further classified into different sub-types, but using the same principle for generating electricity, one of which is concentrating solar power (CSP). This is a type of solar thermal power generation which has gained lot of interest in recent time due to its potential of becoming world's main source of electricity in the future[8].

1.2 Impact on environment and socio-economic benefits of solar energy

Industrialization and all other human activities that use fossil energy have led to the problem of atmospheric and environmental pollution. This, in turn, has given rise to the problem of global warming, greenhouse effect, climate change, ozone layer depletion and acid rain [2]. A viable alternative to avoid further damage and address this issue is the substitution of renewable energy to fossil energy. Since solar energy is easily captured and present in copious amount compared to other renewable energies, its use provides several benefits [9]:

- Lowers the amount of CO_2, NO_x, SO_2 and other toxic contaminants.

- Reclamation of degraded land
- Indirectly improves the quality of the water resources

Solar energy not only provides advantages in making the environment clean and green, but also has a positive impact on society and economy of the country [10-11]:

- Decreases dependency of a nation on others to buy resources for generating energy in a conventional manner.
- Provides great work opportunities to the locals and other small-scale industries.
- Decreases administrative, operation and management costs. Generates free electricity after investment cost is recovered.
- Expedite the electrification process of rural areas in developing countries.

1.3 Concentrating solar power (CSP)

Concentrating solar power is a promising sustainable renewable energy technology. In the last decade, CSP has gained more and more interest, as it uses solar radiation to generate electricity and is carbon free, cost effective, thus has a very promising chance to be the future of renewable energy. The CSP consist of three main major components: the heliostate field, the receiver and power conversion unit shown in Figure 2[12]. Currently there are five types of CSP technologies: 1) Solar power towers, 2) Parabolic trough collector, 3) Linear Fresnel reflector, 4) Parabolic dish system, and 5) Concentrated solar thermo-electrics[13]. All these technologies apply many of the same principles for generating electricity, depending upon its structure and focus to generate different temperature ranges.

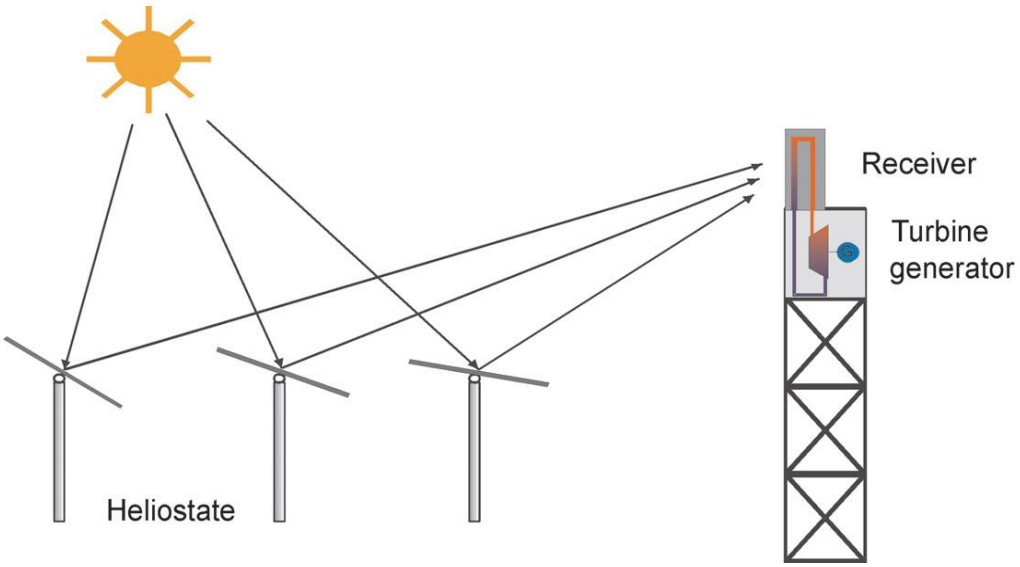

Figure 2. Concentrated solar power tower[14].

AORA, an Israel based clean renewable energy producing company with other facilities in Spain and South Africa, has a platform of hybrid solar power towers that can be operated in solar mode during the day time and with other conventional fuels during night time when there is not solar radiation available to ensure 24/7 uninterrupted power supply [15]. The facility has a central tower or central receiver that uses a distributed heliostat field that are computer controlled reflective mirrors that tracks the sun on its movement through out the day. These mirrors reflects the sun's radiation onto the central receiver on the top a tower, which has very high concentration up to 600 to 1000 times than the normal sunlight that reaches the earth surface and thus producing a very high temperature from 800°C to above 1000°C depending on the receiver design and heat transfer medium[16]. This concentrated heat is transferred to the medium like oil, molten salt, water, air, hydrogen or helium. Different types of receiver have been developed like tubular receiver, volumetric air receiver and solid particle receiver out of which the volumetric air receiver has proved to be more effective and efficient where pressurized air is used as a heat transfer fluid

which is then directly passed to a gas microturbine to generate electricity conventionally.

1.4 Role of Volumetric air receiver

A multiple of porous interlocking, wire mesh, foam or pins, in the case of a special porcupine type absorber, made of ceramics, with specific porosity are installed behind the quartz window near the front or deep inside the cavity of the volumetric air receiver[17]. The quartz window needs to withstand high temperature and pressure in order to help the supplied air to remain pressurized inside the receiver as it gets heated. Different parts of the volumetric receiver and the flow of hot air are shown in Figure 3. The absorbers and the quartz window get heated up due to concentrated solar radiation and when the air passes through the pores or pins it behaves as a convective heat exchanger and air absorbs the heat by means of convection. Volumetric air receivers are capable of generating very high exit temperature[18]. To achieve high temperatures, e.g., from 1200 °C to 1500 °C, ceramics like alumina and silicon carbide are the most appropriate materials.

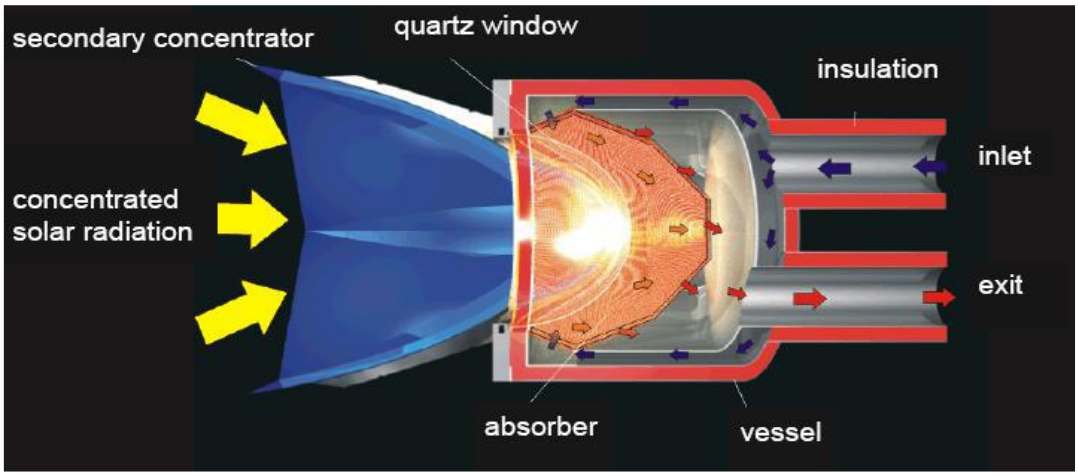

Figure 3. Schematic of volumetric air receiver[19].

There is an instability that occurs when there is a pressure difference between the two sides of the ceramic absorber, leading to unstable airflow and non-uniform heating in the receiver. Thus instability is caused by the change in viscosity and density of the air, which are temperature dependent, resulting in the cracking of the absorber material[20]. In addition, micro-defects present inside the materials can grow due to thermal cycling and due to thermal shock and there is chance for cracking to occur. These cracked materials in the form of debris then enter the air stream and flow along with it to enter the microturbine.

1.5 Microturbine

Microturbines, i.e.,miniature versions of gas turbines, are the prime movers and play a key role in CSP plants. Their compact size makes them ideal to mount with solar radiation receiver inside the top of the tower eliminating the gearbox and linked moving parts [21]. The majority of the microturbines incorporate a single shaft with the generator rotor shaft directly connected to the compressor and turbine rotor; Figures 4 and 5 show the different parts and a block diagram of a microturbine[22-23]. High velocity hot air enters through the centrifugal compressor raising the pressure and temperature of the air, then it passes through the recuperator where air gets heated further, since the recuperator is a heat exchanger[24]. This air then enters the combustion chamber inside which fuel is injected to ignite the combustion which raises temperature up to 800-900°C and pressure, to achieve this high temperature most of the parts exposed to high temperature are made of high temperature alloys like nickel-based superalloys and some high grade stainless steels [25-26]. Now, the high energy gets directed to the turbine where it is converted into kinetic energy of the rotor.

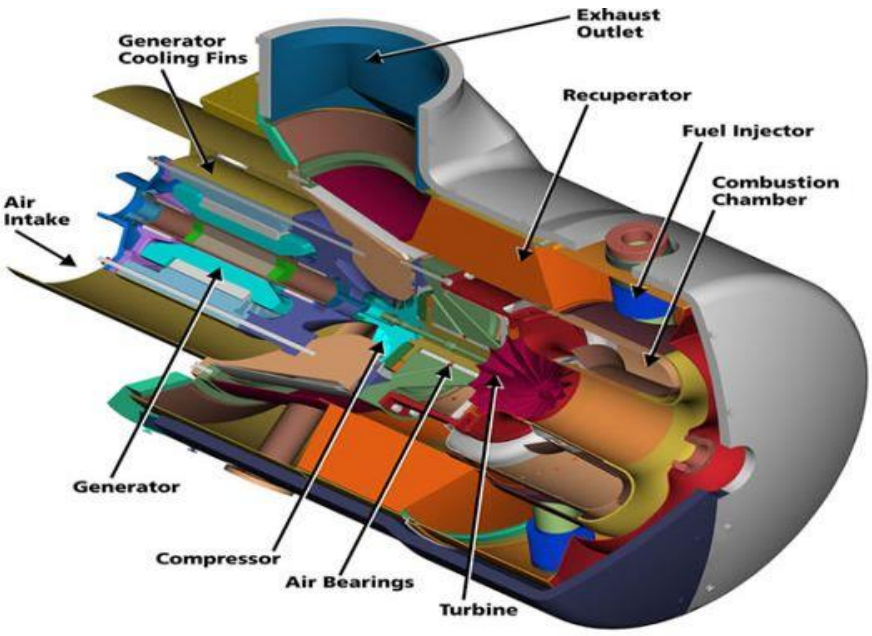

Figure 4. Different parts of a microturbine[27].

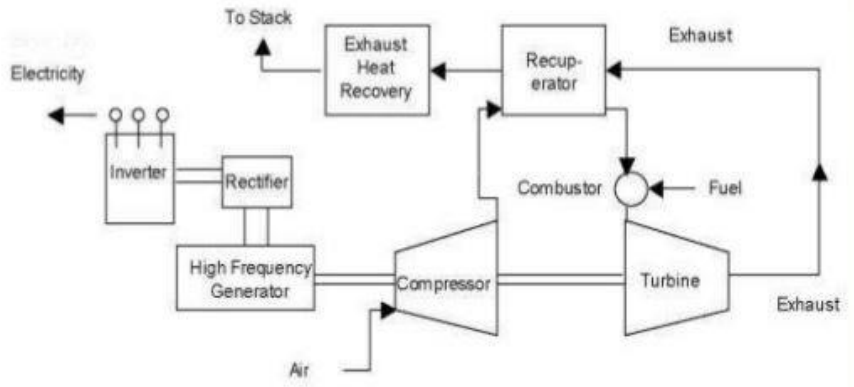

Figure 5. Block diagram for power generation with a microturbine[28].

Since the generator is connected to the compressor and the radial turbine on the same shaft (see Figure 5), it rotates at high speed, from 40,000 rpm to 100,000 rpm, which helps producing useful electrical energy. The air leaving the turbine is then allowed to enter the recuperator where its heat helps increasing the temperature of next incoming air mixture. The heat recovery system adjacent to the recuperator then extracts remaining heat and can be used for secondary operation[21,28].

Complications start arising when the broken debris from the radiation absorber in the receiver or any other external foreign objects enter the air flow path, which is also a concern in AORA's CSP system. These debris particles could be in the range of micrometer to millimeters in size of alumina and silica, which are ceramic materialswith very high compressive strength, sothey are very hard in nature even at high temperature. In regular turbines, the relative velocity of the debris can be 100 m/s to 300m/s when it strikes the surface of the turbine blade or any other metal parts; AORA expects even higher velocities in their system.

Impacts from these debris/objects leave depressions or indents on the surface of the metal that can become sites for fatigue crack initiation, when the temperature is below the creep range of the material, or can results in combined fatigue/creep damage, when creep is an important mechanism[29]. The impact can accelerate the propagation rate of existing cracks and the component might fail before its intended life[30]. In technical terms this type of damage mechanism is termed foreign object damage (FOD) and is well known especially in turbines used for power generation or aircraft propulsion[31]. Nickel-based superalloys and high grade stainless steels are often the victims of FOD in turbines[32]. Work presented in this thesis is focused on specific grades of the nickel-based super alloy-Hastelloy X and stainless steel alloy-SS 347.

2. LITERATURE RIVEW

2.1 Nickel-based superalloys

Nickel based superalloys are an unusual class of material and are most commonly used in aircraft and power generation turbines, rocket engines and in other challenging environments due to their excellent combination of high temperature strength, toughness and resistance to degradation in corrosive or oxidizing environment. These alloys are strengthened by the following mechanisms:

Solid solution hardening (SSH)/carbide hardening

It is a gain in the matrix strength by adding different soluble elements such as molybdenum and tungsten. The addition of the elements causes misfit in atomic radius that inhibits dislocation movement. Using high melting point elements as solute imparts stronger cohesion and reduces diffusion at high temperature. Solid solution hardening also decreases the stacking fault energy in the crystal lattice, which prevents dislocation cross-slip, a dominant deformation mode at high temperature[33].

The following equation represents the basic parameters behind SSH[34]:

$$\Delta \tau = Gb\sqrt{c}\,\varepsilon^{3/2} \quad (1)$$

where c is the concentration of the solute atom, G is the shear modulus, b is the magnitude of the Burgers vector, and ε is the lattice strain.

In alloys where molybdenum and tungsten have limited solubility, carbides are used to impart strengthening at high temperature.

Precipitation hardening (PH)

For high temperature applications, creep strength of nickel-based alloys increases by precipitation hardening. Elements like aluminum, titanium and niobium which has limited solubility in the alloy matrix are used, as the temperature decreases the solubility of these elements is reduced and hence finely distributed precipitates are produced from the solid solution during heat treatment. The intermetallic coherent precipitates produced are γ '-Ni_3(Ti,Al) and γ "-Ni_3Nb, both of which prevent dislocation movement. Controlling factor in PH are: Coherency strain between the γ -matrix and the γ ' precipitate, volume fraction of the precipitate and particle size[35].

Oxide dispersion strengthening (ODS)

Oxide dispersion strengthening has a mechanism similar to PH, but the strengthening elements are added to the alloy and do not precipitate from the matrix. In ODS, the oxide particles are incoherent with the matrix and work with different mechanisms in blocking dislocation movement[33].

The microstructure of nickel superalloys is really intricate with different phases present like dispersed intermetallics plus other various secondary phases that affect the alloy behavior and properties by their composition, morphology and location. They typically have a face centered cubic (fcc) γ -phase matrix and secondary phases include ordered fcc gamma prime (γ ') Ni_3(Al,Ti); ordered body centered tetragonal (bct) gamma double prime (γ ") Ni_3Nb; ordered hexagonal eta (η) Ni_3Ti; ordered orthorhombic delta (δ) Ni_3Nb and fcc carbides such as MC, $M_{23}C_6$, M_6C, M_7C_3 (M stands for metal atom) and many more[36][37], although not all of these phases are present in all superalloys. Nickel superalloys, as mentioned earlier,

gain their strength from solid solution strengthening, dispersion hardening or precipitated phases[36]. The morphology of these precipitates is an important factor in determining the properties of the alloy. Heat treatment is used to modify the precipitates intentionally during the manufacturing, but changes can also be seen in service[38].

The (γ ') $Ni_3(Al,Ti)$ is the most important and useful strengthening intermetallic phase having the $L1_2$type crystal structure and it precipitates coherently with the γ matrix[39]. It is stable over a small range of compositions and enables to achieve an increase in the alloy's yield strength at temperatures up to 800 °C. This occurs in spheroidal and cuboidal shapes depending upon the matrix-precipitate mismatch[40].

Figure 6 shows the different morphology of γ ' precipitates. These precipitates help to withstand high temperature and allow the material to retain the required microstructure during long exposures to high temperatures. The γ ' size also plays an important role in hardening, as it generally increases with the precipitate size until certain point, beyond which the mode of dislocation movement changes from cutting to bypassing causing loss in hardness and strength.

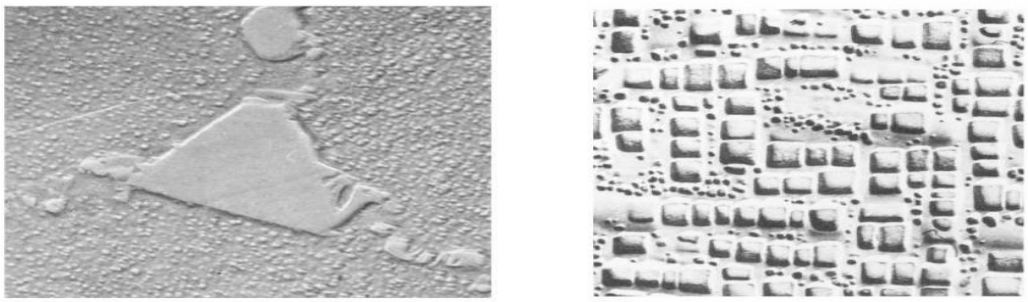

(a) (b)

Figure 6. a) Nimonic 80 showing spherical γ ' precipitates b) U-700 with cuboidal γ ' precipitate at 6000X[41].

Carbides represent another common and important phase seen in polycrystalline nickel based superalloys. They are particularly important in the grain boundaries for providing strength and ductility, if present in the right combination of composition and shape they can provide good creep-rupture strength at high temperature[39].In some alloys for which an intermetallic precipitation hardening phase is not present, carbides serve the purpose through their precipitation[42]. Primary carbides MC are formed in the molten state (above 1038 °C) at intergranular and intragranular location as blocky particles that then break down in subsequent reactions in the solid state to form $M_{23}C_6$ at lower temperatures (790 to 816 °C) and M_6C at intermediate temperatures (816 to 982°C)[41].

The carbides serve three important functions: 1) Grain boundary carbides when formed provide strength to the grain boundaries and allows stress relaxation, 2) When γ' is not formed, fine carbides precipitates strengthen the matrix, 3) They hold down the elements that can induce phase stability[36]. The metallurgy described above is common in most nickel-based superalloys. Several of AORA's turbine components are made up of these materials. In the next section there is specific information about Hastelloy X, which is of interest to AORA.

2.1.1 Hastelloy X

It is expected that cyclic loading, creep and their interactions can limit the service life of Hastelloy X at elevated temperatures[43]. The influence of hold time at high temperature under cyclic loads is a significant factor affecting the service life of this material[44]. Under this condition, particularly under low cycle fatigue, one can see cyclic hardening, followed by cyclic softening[45]. Generally, longer hold times

would result in reduction of fatigue life when temperature rises above 980 °C[44]. Along with this, oxidation effects become pronounced when the hold time is increased. The stress relaxation that occurs during hold times contributes to the development of creep strain and increases the accumulated strain at the tip of any cracks present, which promotes fatigue crack growth[46]. Thus the combination of creep damage and oxidation can lead to a considerable reduction of fatigue life [44].

In this alloy $M_{23}C_6$ carbides and sigma phase also play a role in the degradation of mechanical properties. Total strain-controlled low-cycle-fatigue tests with and without hold times have been performed at temperatures ranging from 816°C to 982°C in laboratory air[44]. Micrographs taken with and without hold time suggest that a crack first initiates and then propagates transgranularly for the periods without hold, while both transgranular and intergranular propagation occur for periods with hold times[45]. The material undergoes changes from cyclic hardening to cyclic softening with changes in temperature due to dislocation recovery effects during strain cycling, so at higher temperatures and longer hold times there is less resistance to the motion of dislocations and this gives rise to cyclic softening. Moreover, the effect of oxidation damage becomes significant when the hold time is considered, as longer times will be spent at high temperature and high loads[45]. Typical M_6C and $M_{23}C_6$morphology evolved after 26 hours of heat treatment at 750°C is shown in Figure 7.

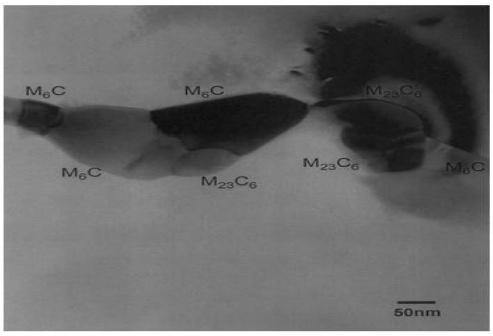

Figure 7. TEM image showing morphology of chromium carbides in Hastelloy X[47].

This alloy consists of uniformly sized M_6C precipitates randomly distributed in a solid solution [48]. Figure 8 shows microstructure of Hastelloy X tensile tested at high temperature, at high temperature, in the range of 600 °C, fracture initiates in the vicinity of the primary carbides in Figure 8a, grain boundary shear fracture at triple point, intergranular fine precipitates and twin boundaries along with grain elongation is seen in Figure 8b and 8c. At higher temperatures, precipitates ripen and lose their effectiveness as dislocation pinners. Precipitation leads to extensive solute depletion and weakening of the solid solution matrix, and this weak matrix deforms intragranularly as well as by grain boundary shear[49].

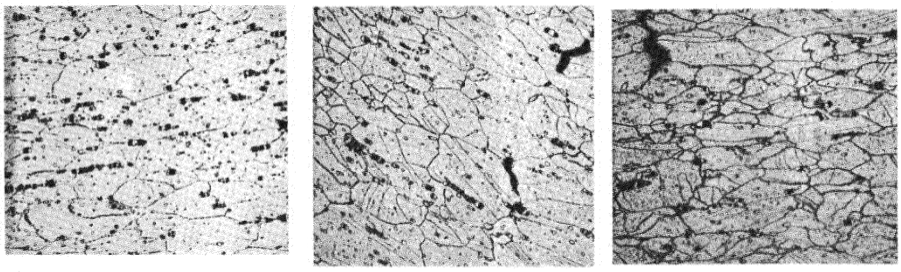

(a) (b) (c)

Figure 8.Microstructure of Hastelloy X tensile tested showing precipitation and grain elongation at a) 600 °C-200x, b) 648 °C-200x, c) 760 °C-200x[49].

Hence, failure in Hastelloy X starts at with fracture occurring by the normal transgranular crack propagation method. This crack initiates at carbides and advances across the grains. Due to excess carbide precipitation at elevated temperature and due

to plastic deformation there will be depletion of solid solution strengthening elements from the lattice[49].

2.2 Austenitic stainless steel

Austenitic stainless steel is seen widely used in the food, chemical and energy industries. It has a face centered cubic (fcc) structure and is excellent in performance at high temperature due its excellent oxidation resistance, general corrosion resistance, creep resistance with high ductility and toughness. Stainless steels contain 16-26% Cr, 8-25% Ni, 0-6% Mo and other elements like Mn, Ti, Nb[50].

Similar to nickel superalloys, steel addition of other elements into the austenitic matrix results in precipitation of carbides, nitrides and intermetallics that could be helpful and in some instances could be detrimental, if present in excessive amounts, for certain properties. In particular, $Cr_{23}C_6$ carbides are most common in the austenitic stainless steel seen at grain boundaries, twin boundaries and intragranular sites. Microstructure coarsening and precipitation of σ (sigma) and Laves phases are considered to be detrimental as they cause matrix weakening[50]. During long exposure time at high temperature sigma phases precipitates at grain boundaries and triple point as shown in Figure 9.

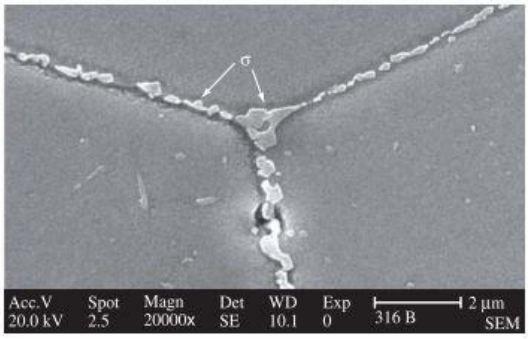

Figure 9. Formation of sigma phase at grain boundary and triple point[51].

Sigma phase causes loss in ductility and due to loss in chromium and molybdenum from solid solution the alloy becomes more susceptible to corrosion and high temperature resistance[51].Another material of interest to AORA in terms investigation of failure of its turbine components is SS 347. The next section describes the specific details of this alloy

2.2.1 Stainless Steel 347

The behavior of grade 347 stainless steels does not seem to be as widely studied and documented as for other austenitic stainless steels, particularly at high temperatures, as not much of the available literature provides specific information about it. This grade was developed to provide the 18-8 type alloy with improved intergranular corrosion resistance, since it is stabilized against chromium carbide formation by the addition of niobium and tantalum. These elements have a stronger affinity for carbon than chromium, and their carbides precipitate within the grains instead of forming at the grain boundaries[52-54].

This steel is stabilized by addition of molybdenum, titanium or niobium. Additions of niobium or titanium prevent precipitation of grain boundary carbides, as described above, and contribute to precipitation hardening by MX type carbide or carbonitrides. Chromium and molybdenum increase the corrosion resistance of steel, but make the austenite phase unstable due to formation of intermetallic compounds known as σ-phase[50].

In niobium stabilized steel, niobium carbonitrides, Nb(C,N) form due to high affinity between niobium and interstitials. Figure 10 shows coarser (primary) Nb(C,N) precipitates in the later part of the solidification process, there is also a dispersion of

fine (secondary) Nb(C,N) formed during solution annealing homogenously distributed in the matrix as shown in Figure 11. The solubility and the stoichiometry of Nb(C,N) determine the behavior of the steel with regard to temperature. The presence of this phase not only affects the mechanical properties but also reduces the corrosion resistance [50].

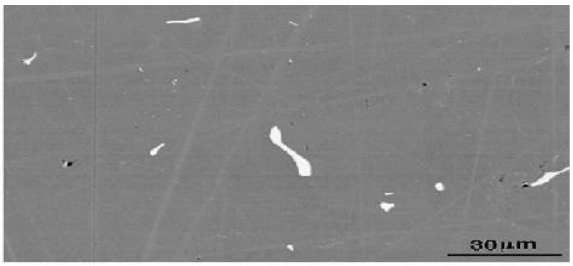

Figure 10. The morphology of primary Nb(C,N) shows that they are formed interdendritically during solidification[55].

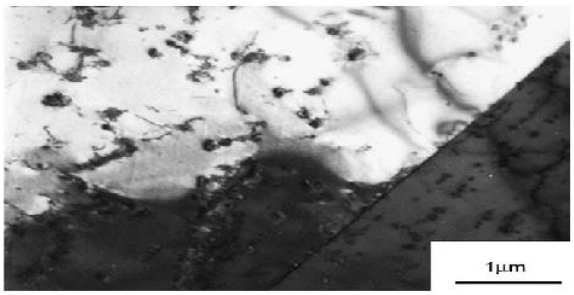

Figure 11.Micrograph showing secondary Nb(C,N) embedded in the austenite matrix [55].

One of the objectives of this work is to see and compare the effect of foreign object damaged sample to sample without foreign object damage on the fatigue life of the two alloys described above. In the next sections some insight about effect FOD on ductile metals, fatigue mechanism and effects of FOD on fatigue are discussed.

2.3 Foreign object damage of ductile materials

The idea of foreign object damage and how it is important on the overall context of this work was introduced in section 1.6. In this section more insight is

provided in terms of the damage via wear/erosion it creates on component's surfaces. Foreign object damage (FOD) is any perturbation or change caused by a particle/debris/substance that is foreign to the system that could potentially cause the initiation of damage in parts of the system. Depending on the system, the foreign object causing damage could be anything that is integral part of the system's components, for example: broken pieces of metal, loose parts, nuts, bolts, or external contaminants, e.g., sand, hard amorphous materials, rocks, small animals (or birds in the case of aircraft), etc. The erosion/wear caused by FOD may be influenced by several factors [56], many of them listed below:

- Angle of impingement.
- Particle rotation at impingement.
- Particle velocity at impingement.
- Particle size.
- Surface properties.
- Shape of the surface.
- Stress level in the surface.
- Particle shape and strength.
- Nature of the carrier gas and its temperature.

2.3.1- Effects of Important Factors

Angle of impingement is defined as the angle between target materials and the trajectory of the erodent particle. Dependence of erosion rate on impingement angle is dictated by the nature of the materials involved. As shown in Figure 12 for ductile

materials, e.g., metals and alloys, the maximum rate of removal is at 15° and 30° while for brittle materials like glass the maximum removal rate is at 90°.

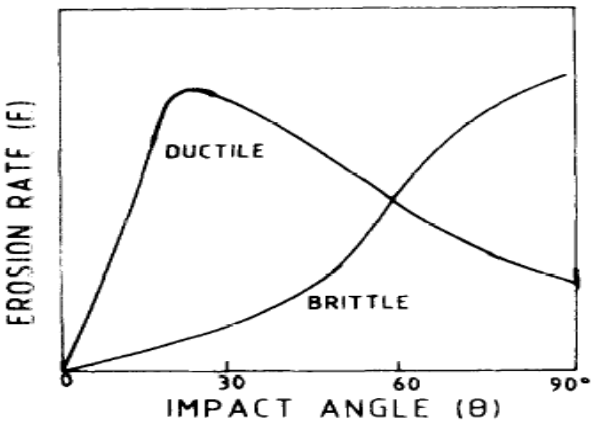

Figure 12. Effect of impact angle on erosion rate of ductile and brittle material[57].

Impact velocity affects the rate of removal of material from the surface. The rate of material removal (E) is defined as the ratio of weight loss of the eroding material to the weight of the eroding particle. The velocity dependence of erosion rate is given by a power-law relationship, $E=E_0V^p$, where p the velocity exponent, E_0 is a constant and V is impact velocity. In case of metallic materials, available experimental data shows that under oblique impact the velocity exponent is 2.4. The effect of impact velocity and angle of impact on the erosion rate of aluminum is show in Figure 13(1), which shows the increase in erosion rate with increasing impact velocity, but as shown in Figure 13(2), when the erosion is rate is normalized by dividing by the erosion rate at normal impact, the erosion rate becomes independent of the impact velocity[58].

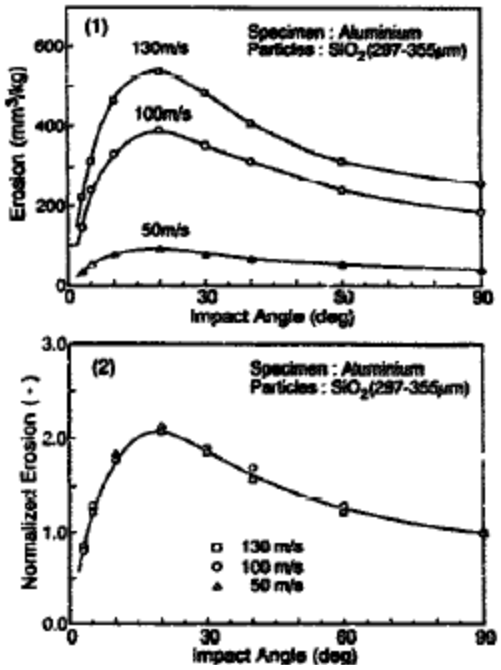

Figure 13. The effect of impact velocity on 1)erosion rate and 2) normalized erosion rate of aluminum[58].

Regarding particle size, the interesting aspect about it is that the amount of material removed by a mass of abrasive material is independent of particle size for particles larger than 50μm to 100μm and below this size the erosion becomes less and less efficient as shown in Figure 14.

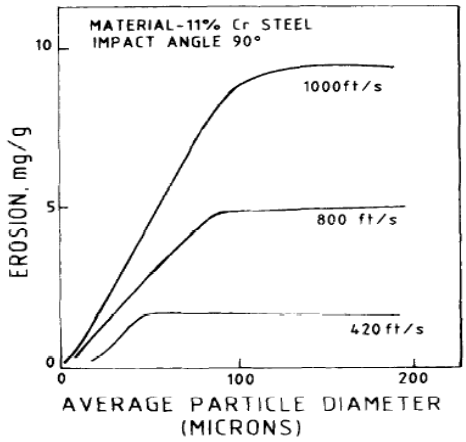

Figure 14. Variation of erosion rate of steel with particle size at normal impact at different impact velocities **[**57**]**.

Particle shape also affects the erosion rate of metals. Angular particles tend to cause higher erosion rates as compared to spherical shaped particles. Figure 15 shows a comparison of erosion rates for spherical and angular particles. In particular, it can be seen that erosion due to spherical steel balls is maximum at a normal impact angle for Copper alloy while for the same material angular SiC particles result in a ductile response with regards to the erosion behavior. This indicates that as the angularity of the erodent particles increases the erosion rate-impact behavior shifts towards a ductile response[57].

There has been several explanation on size dependent erosion behavior some of which includes ploughing, strain rate sensitivity of materials, rake angle, high temperature, etc., [59], but the mechanisms that apply to one wear process might not hold true for a different one. In general this can be attributed to some material surface properties like surface work hardening[60]. The quantification of this phenomenon still remains a future work to do. The reason for the erosion rate becoming constant after certain particle size of erodent could be due to the number of particles striking the surface, their kinetic energy and interference between incoming and rebounding particles[61]. The sharpness of the particles edge does not change with an increase in particle size; therefore, the ability to penetrate and plastically deform the material does not change. Additional evidence that erosion changes with particle shape is given in Table 1.

Table 1. Effect of particle shape [61].

Particle size (μm)	Feed rate (g min^{-1})	Mass loss (mg)			
		20 m s^{-1}		60 m s^{-1}	
		Spherical	Angular	Spherical	Angular
250–355	6.0	0.2	1.6	3.0	28.0
250–355	0.6	0.2	2.0	4.5	32.7
495–600	6.0	0.1	–	1.2	–
495–600	2.5	–	2.0	–	42.4

The data in Table 1 and [61] clearly show that angular particles cause more erosion than spherical particles. Hence, particle shape plays a major role in changing the erosivity of materials, given that the difference is nearly a factor of 10 between spherical and angular particle erosion rate. Hardness of the erodent particle also affects erosion rate, e.g., if the hardness of the erodent is close to that of the target, the erosion rate will decrease[61].

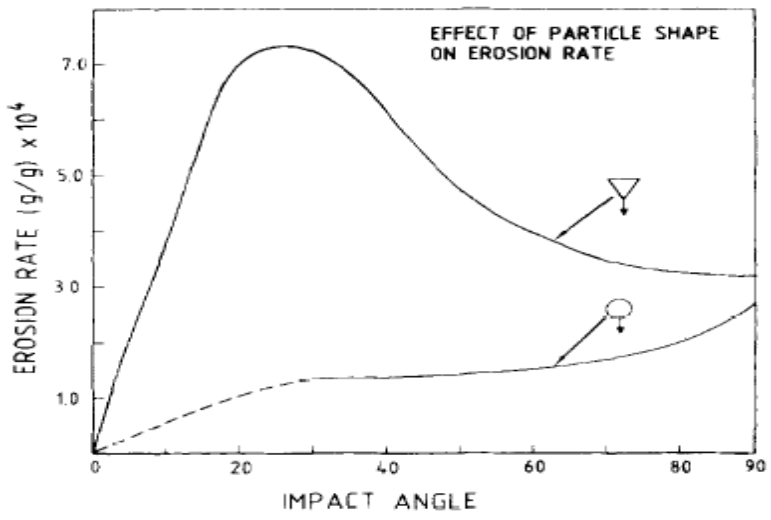

Figure 15. Influence of impact angle on erosion rate in the case of spherical and angular particles[56].

Figures 16 and 17 show the temperature effects on the erosion characteristics of titanium 6Al-4V and 410 stainless steel, respectively. The plots show erosion parameter ε , defined as milligrams of eroded materials per gram of impacting material vs. temperature.

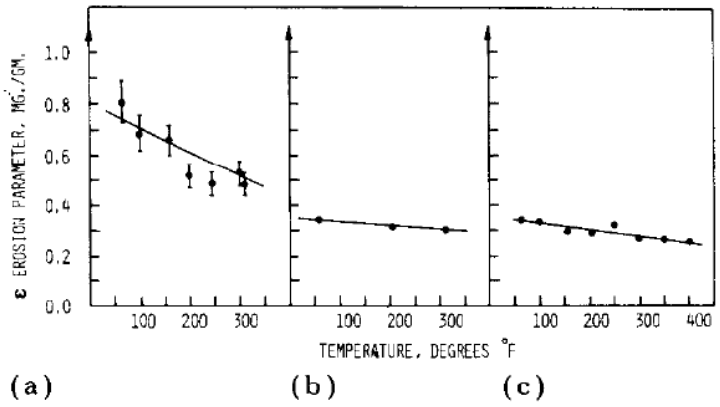

Figure 16. Effect of temperature on the erosion of titanium 6Al-4V. Angle of impact (°):a)20,b) 60,c)90. Particle size (µm):a)164, b)164, c)164. Particle velocity (ft.s-^{1}**)**: a)400, b)382, c)399 **[**62].

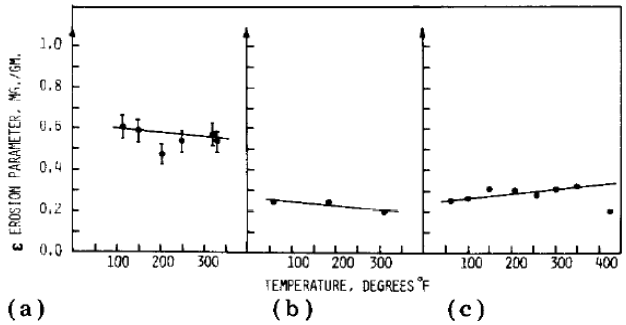

Figure 17. The effect of temperature on the erosion of 410 stainless steel. Angle of impact (°): a) 20, b) 60, c) 90. Particle size (µm):a)138, b) 138, c)138. Particle velocity (fts^{-1}): a) 410, b) 390, c) 410 [62].

At 20°, 60° and 90° angle of impact titanium shows a decrease in erosion Figure 16), the same trend is observed in steel (Figure 17) for 20° and 60°, but at a 90° angle the erosion [20] decreases. The literature does not talk about the reason for the decrease in the erosion rate, but one can guess it could be due to work hardening of the surface due shot-peening action of the abrasive particles and the erosion could increase again after continued effects of impacting particles.

Figure 18 shows the crater formed by the displacement of materials from an aluminum sample made by a single particle impact of SiC, 250µm, at 30 m/s speed

and an angle of 30°. This is an example of the mechanism called ploughing in which particles coming at an angle produce shear action and with rolling further impacts take place beyond the site of impact, leaving a curved depression, as well as a lip at the side of the depression and at the front of the particle [21].

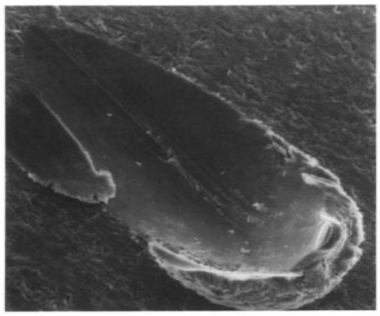

Figure 18. Single impact crater on 1100-0 aluminum[63].

2.4 Fatigue

Fundamental mechanisms for fatigue damage are described in this section, as they are important to gain a basic understanding of the phenomenon before discussing the more complex interactions between FOD and fatigue.

Fatigue failure of structural components often occurs due to alternating stresses that are much smaller than the required stress to cause failure. Initiation of cracks always occurs at a surface discontinuity for the high cycle fatigue regime. Even if there is no potential crack initiation site small micro-crack can initiate due formation of persistent slip bands (PSB), since the plastic strain in these region is very high compared to the region away[64]. Due to movement of many slip planes steps are produced called intrusions and extrusions (Figure 19) due to imperfect reversal of the local plastic strain, and they eventually lead to crack formation[64]. The crack propagation rate is very slow ~1nm/cycle and therefore no distinct fracture features are observed[64].

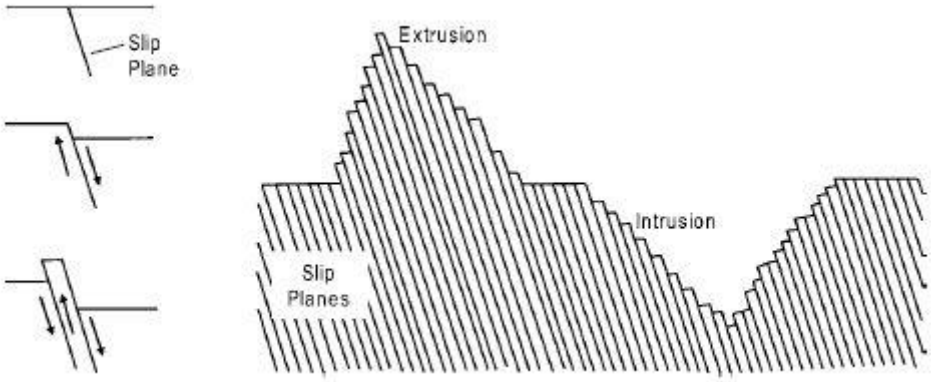

Figure 19. Slip plane movement in fatigue[55].

After reaching sufficient crack length such that stress field at the crack tip is dominant, the crack starts propagating perpendicular to the principal stress where crack proceeds in a process of plastic blunting and produces fatigue striation as shown in Figure 20. At the beginning of the load cycle the crack tip appears to be sharp (Figure 20-1), as tensile load is applied small double notch concentrates the slip along planes 45° to the plane of the crack (Figure 20-2), as the crack stretches to its maximum width, it elongates by plastic shearing resulting in a blunt crack tip. When the load is reversed, the slip direction also gets reversed at the front of crack tip (Figure 20-4) and the new crack surface is created due to tension into the plane of the crack (Figure 20-5) where it folds due to buckling to form a new sharp crack tip, this new crack tip is the ready to propagate in the next loading cycle[56].

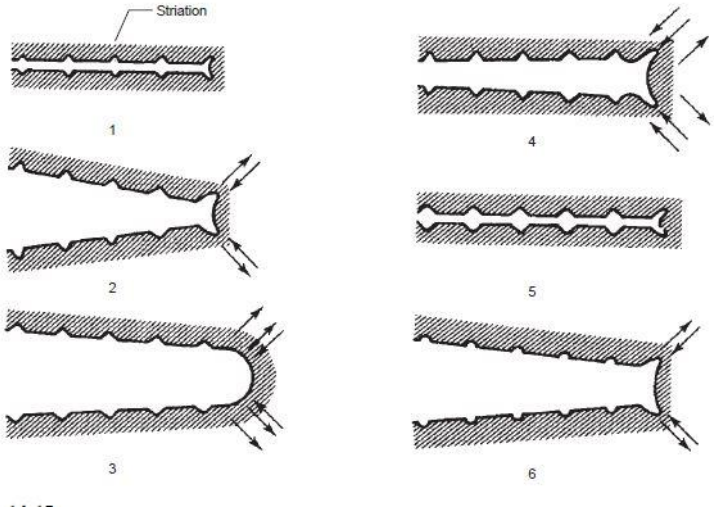

Figure 20. Plastic blunting crack growth process[55].

During this process the crack is considered to be a macro-crack and would have been in the size range of few millimeters. Here the important linear elastic fracture mechanics parameter ΔK is the rate-governing factor[64].

$$\Delta K = Y \Delta \sigma (\pi a)^{0.5} \quad (2)$$

where $\Delta K = K_{max} - K_{min}$, $\Delta \sigma = \sigma_{max} - \sigma_{min}$, a is crack length and Y is dependent on specific specimen geometry.

The fatigue crack growth behavior can be represented by plotting crack growth rate da/dN vs. ΔK as shown in Figure 21. Considering region I, crack does not grow at all values of ΔK, da/dN increases as ΔK increases from ΔK_{th}, which is the minimum value for crack to propagate, in stage II crack growth is linear and stable and is described by a power law in the Paris regime[64].

$$da/dn = C(\Delta K)^m \quad (3)$$

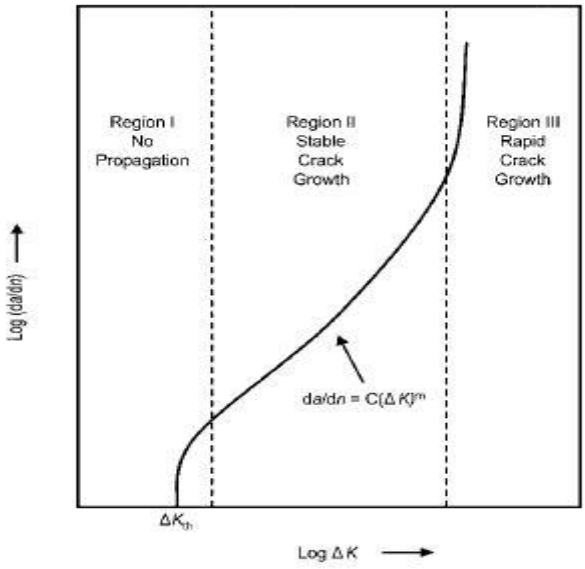

Figure 21. Schematic of fatigue crack growth rate[64].

Where, a=crack length, n number of cycles, C and m are material constants dependent on temperature, environment and stress condition. This relation helps in estimating useful fatigue life. The crack growth rate da/dN sometimes is reduced due to crack closure phenomenon, during this period crack temporarily stops propagating.

Fatigue is very sensitive to surface conditions. Interaction of foreign object damage on the material surface and its effects on fatigue are described in following section.

2.5 Effect of foreign object damage on fatigue

Microturbine blades and other components experience a variety of load conditions like low-cycle-fatigue (LCF) due to on/off cycle, and high-cycle-fatigue (HCF) due to vibrations and airflow dynamics. The microstructural damage caused by FOD can lead to fatigue failure under such loading conditions. Following are the factors that plays a role in governing FOD induced fatigue cracking or failure[65]:

1) Stress concentration around the impact site: Stress distribution gets altered in the vicinity of the impact site under applied loads due to indent or change in topography created by FOD.

2) Residual stresses induced due to impact: FOD creates a residual stress field due to plastic deformation around the impact site, which can either increase or decrease the total stress acting on the fatigue crack initiated at the site. It can influence the initiation and propagation of cracks when combined with cyclic loading and stress concentrations.

Analytical study of FOD induced residual stress field has carried out by creating a finite element model [65]. The parallel experimental investigation has also been done on FOD induced high cycle fatigue properties of Ti-6Al-4V (Titanium alloy)[66]. As shown in Figure 22a sphere (diameter-D) is pushed with a load P, after unloading contact diameter and depth of indent is measured as w and δ respectively. This depiction is realistic for the titanium alloy Ti-6Al-4V, yield stress σ_y, Young's modulus E and Poisson's ratio ν is considered for dimensional analysis of residual stress field after unloading.

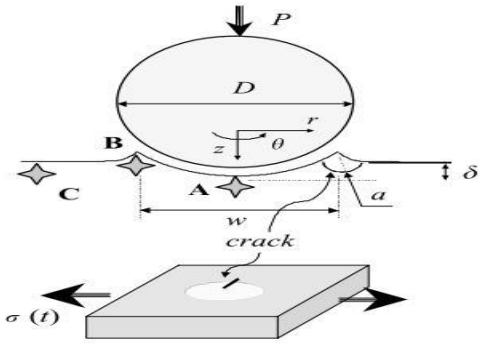

Figure 22. Three most likely crack fatigue crack sites denoted by A, B and C[65].

The stress field from quasi-static indentation takes the functional form of[67]:

$$\frac{\sigma_{ij}(r,z)}{\sigma_y} = f_{ij}\left(\frac{P}{\pi/4 D^2\sigma_y}, \frac{\sigma_y}{E}, \mu, \frac{r}{\sqrt{P/\sigma_y}}, \frac{z}{\sqrt{P/\sigma_y}}\right) \quad (4)$$

where r and z are the radial and axial directional coordinates, respectively, μ is the Coulomb friction co-efficient and dimensionless load factor $L = \frac{P}{\pi/4 D^2\sigma_y}$ for finite element calculations. Three different load levels a)L=0.0013, b)L=0.064 and c)L= 1.91were computed to show very shallow, moderately shallow and deep indentation results, respectively. In the results for the very shallow regime, residual hoop stresses were observed to be compressive below the indent and tensile outside the rim (boundary of the indent), for the moderately shallow regime, surface hoop stresses are tensile at the bottom of the indent and becomes compressive at further below, and outside the rim at a distance about twice of the indent radius the stresses becomes tensile. For deep indents there are compressive stress within the indent and prominent tensile stresses outside the rim[67]. Dynamic stress fields accounting for kinetic energy of particle have also been studied. The residual stress field for dynamic impact is given by[65]:

$$\frac{\sigma_{ij}^R}{\sigma_Y} = F_{ij}^R\left[\frac{x}{D}, \Omega\right] \quad (5)$$

Where $\Omega = \frac{\pi}{12}(\rho_p / \sigma_Y)v_0^2$ is a dimensionless impact energy parameter, ρ_p = particle density and v_0 = particle velocity.

Experiments to study FOD on Ti-6Al-4V have been done and the residual stress distribution shown in Figure 23 was deduced by using X-ray microdiffraction and numerical studies[66]. Results show that after impact the constraint due to the surrounding elastic material leads to a compressive residual hoop stress σ_θ and a tensile residual radial stress $\sigma_{r.}$ Moreover, three different zones of tensile residual hoop stress are created as also shown in Figure 23, and this increases the local mean stress during fatigue cycling. Two regions are small but intense and the residual stresses were estimated to vary between $0.4\,\sigma_Y$ and $0.8\,\sigma_Y$. In FOD experiments fatigue has been observed to initiate at all three locations and a reduction in the critical crack size threshold is observed. The study also suggests that both geometric stress concentration and residual stress are important factors when the load ratio R is below 0.4 while at higher R values only the geometric stress concentration plays a role on critical crack size threshold.

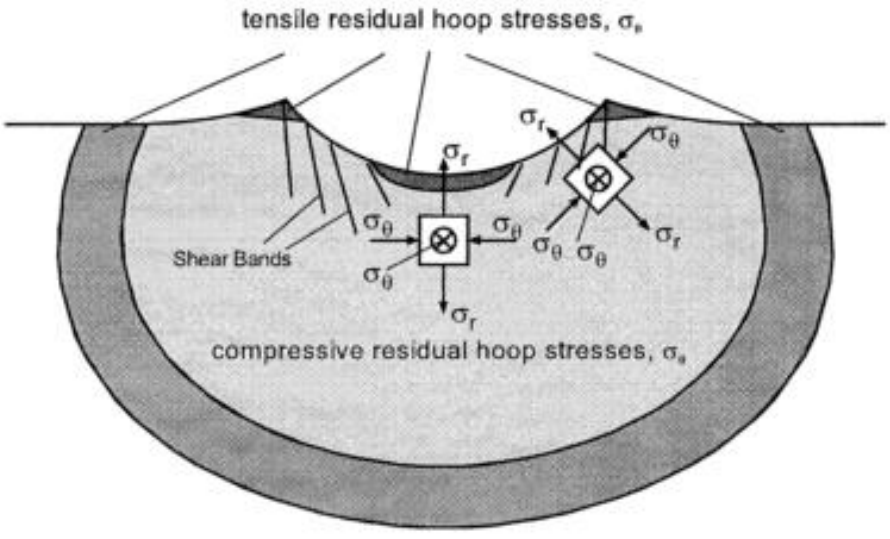

Figure 23. Residual stress state after impact [65].

The effect of FOD on the fatigue life of Ti-6Al-4V is shown in Figure 24. A steel ball of 3.2 mm diameter was used to simulate FOD at normal impact angle. It can be seen that there is a reduction in fatigue life when compared to undamaged specimens shown in the S-N curve. The fatigue cracks were observed to initiate from different locations[68], at high applied stress and high velocity the crack tended to initiate at the crater rim due to microcrack formation, for lower impact velocity the crack initiated at the base of the indent due to high stress concentration compared to the rim, where at lower velocity there is absence of microcracks. However, at lower applied stress and lower impact velocity, crack tend to initiate away from the indent crater at the location where high tensile residual stresses are present on such crack initiation site is shown in Figure 25. Moreover there are chances of multiple microcracks forming at the rim, i.e., around the edges of the impact area at high velocity[69].

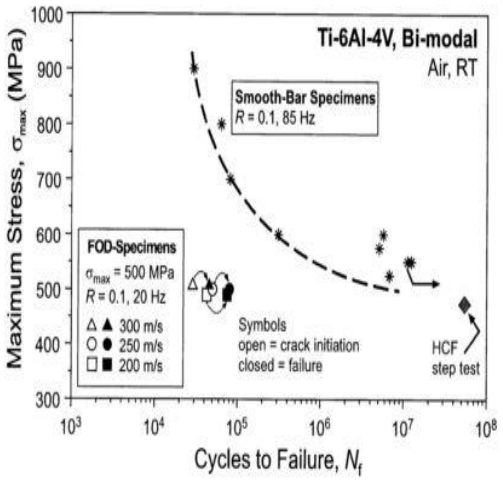

Figure 24. S-N curve showing effect of FOD in Ti-6Al-4V[65].

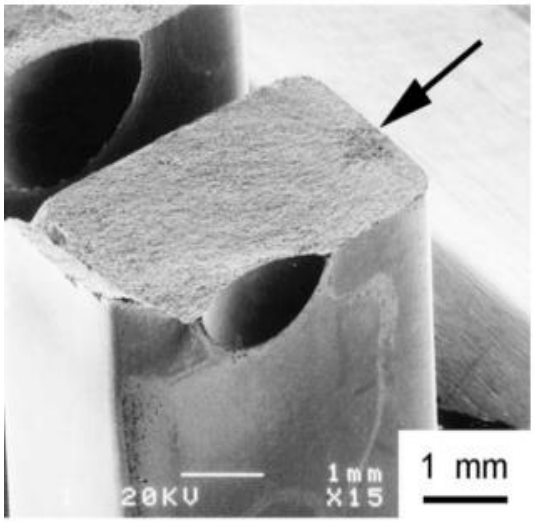

Figure 25. Fractograph showing crack initiation at the surface. σ =325MPa, R=0.1, N_f=1.6x10^7[68].

3) Microcrack and micro-structural distortion: FOD alters the local microstructure creating shear bands or texturing, which are potential sites for crack nucleation.

As mentioned above, FOD affects the threshold for crack growth and one such comparison to crack growth of undamaged material is shown for load ratio R=0.1 and R=0.5 in Figures26a and 26b respectively for Ti-6Al-4V with two microstructures, bimodal and lamellar, having UTS of 965 MPa (Bimodal)-1055 MPa (Lamellar).

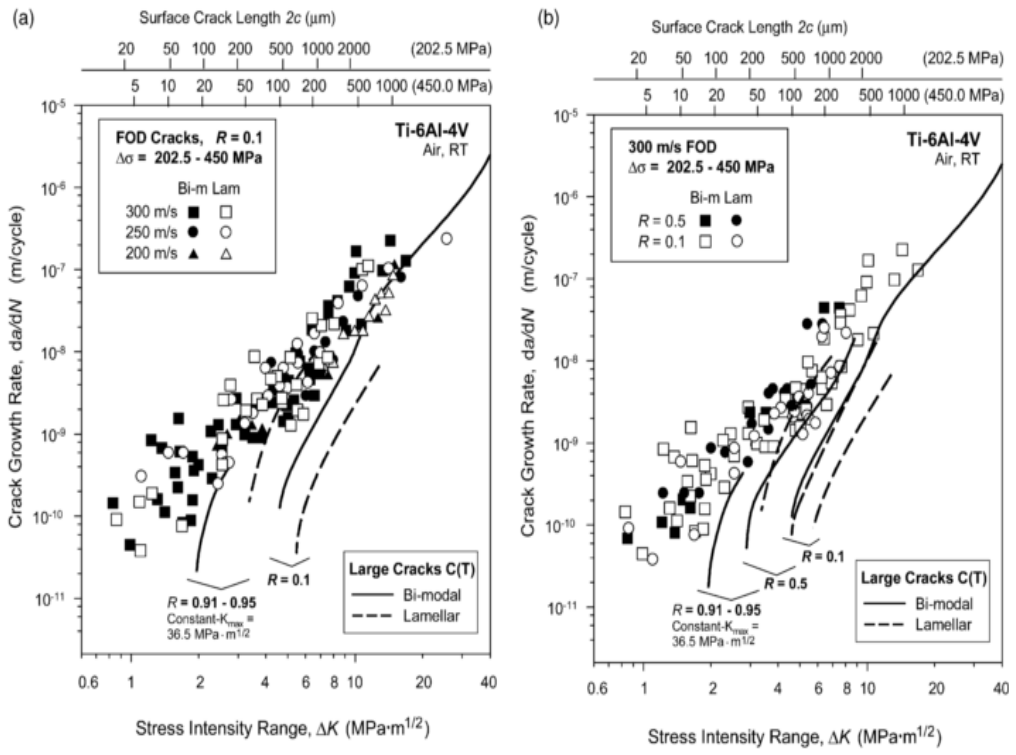

Figure 26. Crack-growth rates as a function of applied stress-intensity range at load ratios of (a) R=0.1 and (b) R=0.1 and 0.5 of FOD small cracks and large cracks in bimodal and lamellar Ti–6Al–4V. Large-crack growth data for R=0.1 derived from constant load-ratio tests and for R=0.91 (lamellar) and 0.95 (bimodal) constant-Kmax/increasing-Kmin testing was used[70].

The FOD crack growth data is shown as function surface crack of length 2c and applied stress intensity range for two different types of microstructure. The growth rate for FOD-initiated small cracks is one order of magnitude higher than for long

cracks at near threshold levels[70]. For the bimodal microstructure, as the small crack grows the result shows it merges with the long crack above ΔK=10 MPa-$m^{1/2}$. However, the trend is opposite for the lamellar microstructure showing high crack growth resistance in the presence of long cracks. The faster crack growth rate is believed to be associated with impact-induced plasticity, which causes reduced resistance to crack growth. The above study considered FOD on flat specimens, more discussion on FOD occurring at leading edges of turbine blade is provided below.

There have been different approaches used by researchers to simulate FOD and study it at laboratory scale. A quasi-static chisel indenter can be used to make a notch on the edge of a blade or specimen[71-72]. The indents resulting from these methods are simpler than those produced by dynamic impacts and so the residual stresses resulting from them are not similar to real dynamic FOD[30]. Another technique that has been used [73] is hitting the leading edge of a component with a swinging pendulum. In addition, to get close and to have better understanding of real FOD, experimental work based on the use of small particles like steel balls fired onto targets using a gas gun has also been carried out[31].

In one such experiment, hardened steel spheres of 1 and 3.2 mm in diameter, were normally shot on Ti-6Al-4Vat speeds of 200-300 m/s. The specimens were then cycled at a load ratio of 0.1 with maximum nominal stress of 325 or 500 MPa. The most likely fatigue crack initiation sites are shown Figure 27[74]. At low stresses points "1" and "2" are favorable sites due to tensile residual stresses reaching maximum[65]. At high stresses and low impact speed, 200 m/s, point "3" is the crack initiation site due to high stress concentration at this point. At high stresses and high impact speed 300 m/s, microcracks are produced at point "4". Due to combined effect

of residual stress and stress concentration superimposed on these cracks it turns out to be a site for fatigue cracking [74].

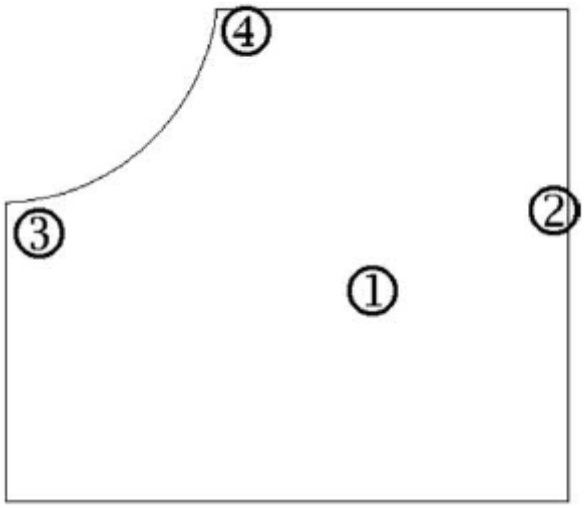

Figure 27. Schematic showing half cross section fatigue crack sites, impact location is shown by curved portion [73].

The previous experiment discussed considered flat specimens and in order to simulate more realistic FOD, a model system representative of leading edge of turbine blade as shown in Figure 28(a) was considered to demonstrate the fatigue crack initiation due to FOD[74]. In this model, a blade with thickness of about 1 mm was impacted with particles at a speed of 300m/s using a particle size in the range of 1-4 mm. Figures 28(b) and 28(c) show the three-dimensional schematic of impact and the cross section A-A, respectively.

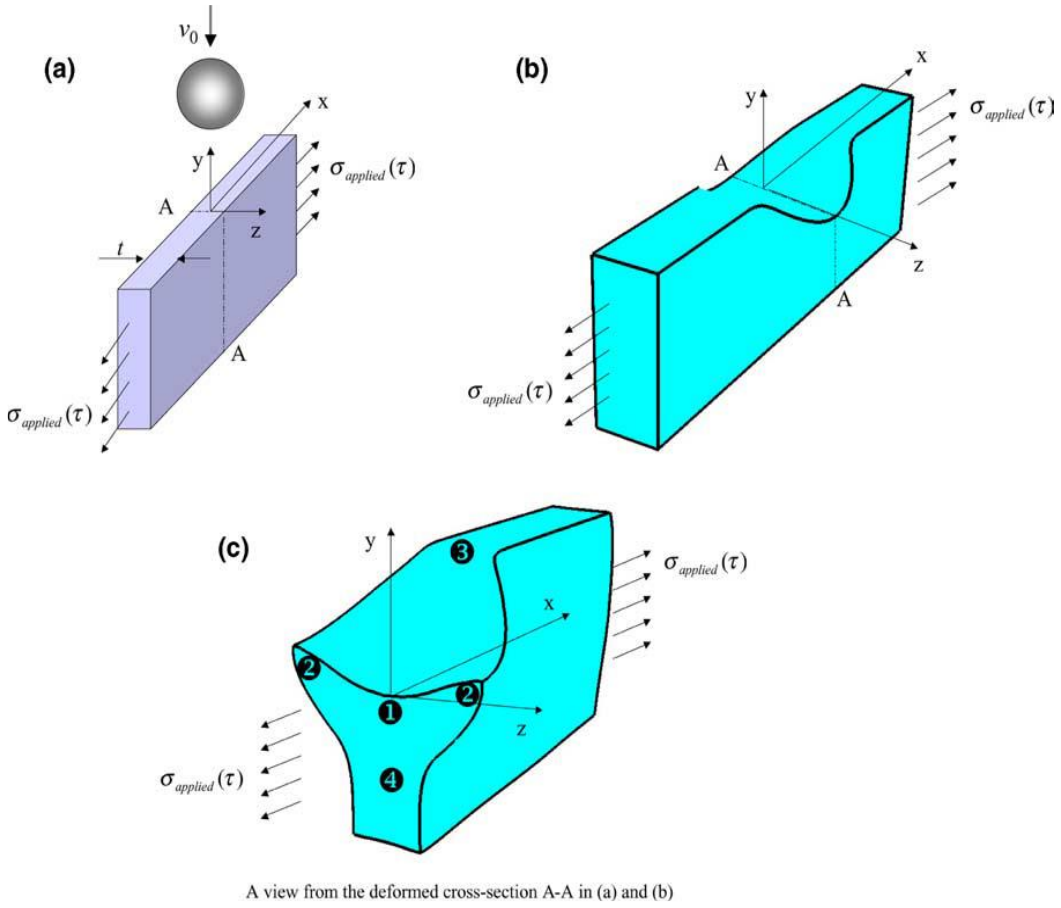

Figure 28. Schematic showing a) rigid particle impacting normally to the edge of a thin plate, b) deformed configuration, c) cross section A-A[74].

Experiments in [74] showed that the fatigue life of the specimen decreases with increasing indent depth upon cyclic loading along the x-direction. It was observed that most of the fatigue cracks initiate from point "1", i.e., the bottom of the indent or from point "2", the bulge tip. In addition, a few cracks also form at point "3" outside the crater rim or at point "4", beneath the surface of the indent as shown in Figure 28(c)[74].

The study discussed above considers the effects on fatigue due to large single particle, i.e., in the mm range in size, and the indentation/impact created by it. In this research work FOD experiments are conducted using a stream of multiple particles

striking onto the surface to create an impact that may have an effect similar to that produced by the shot peening process, so this topic is briefly reviewed next.

2.6 Effects of shot peening

Some of the factors mentioned in section 2.3 also play a role in controlling effects of shot peening. These factors are shot speed; shot dimension, shape and hardness of shot; angle of incident; exposure time under shot peening and surface area covered by shot peening. The effects of shot peening on a material surface also depend on materials hardness, microstructure and hardening characteristics of the material. The interaction of shot peening factors and material factors can result in residual stresses in the material, strain hardening at the surface and sub surface, as well as alteration in surface and substructure of materials[75].

The shot peening process is generally used to increase the fatigue life of component as the striking of the shot produces a compressive residual stress due to work hardening on the surface till a depth of generally about 0.1-0.25 mm, which delays the initiation of fatigue cracks. The depth of the deformed layer decreases with decrease in materials hardness and almen intensity, i.e., shot peening intensity (Figure 29a), depending on the hardness of the material being shot, the increase in diameter of the shot increases the depth of work hardening and stabilizes after certain level (Figure 29b). The maximum stress residual stress level and residual stress gradient will depend on the depth of the material being deformed and in turn will control the residual stress distribution[76].

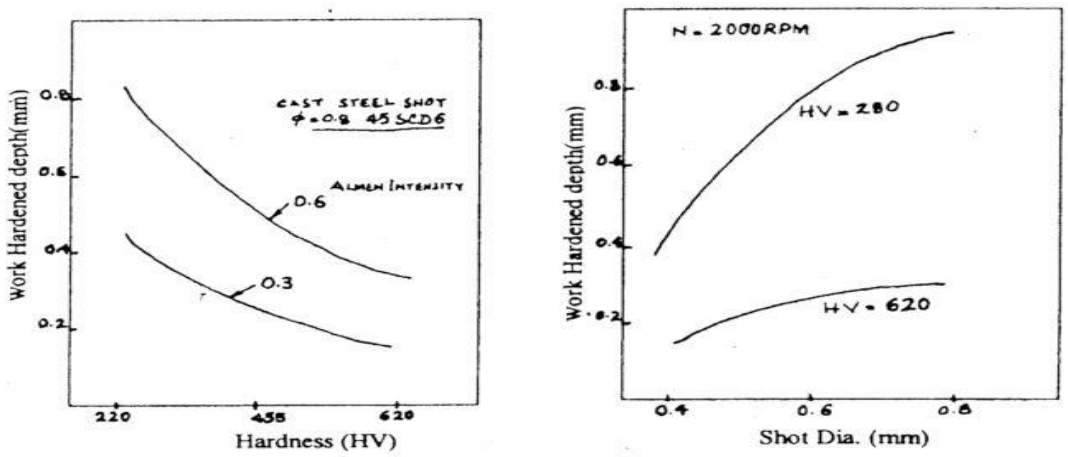

(a) (b)

Figure 29. Effect of a) Material hardness b) Shot diameter on work hardening depth [75].

The typical stress distribution pattern along the depth of the material is shown in Figure 30. The symbol (SS) indicates the surface stress below which (CS max) compressive residual stress exist and at depth d the residual stress becomes maximum tensile stress (TS) and becomes uniform[77].

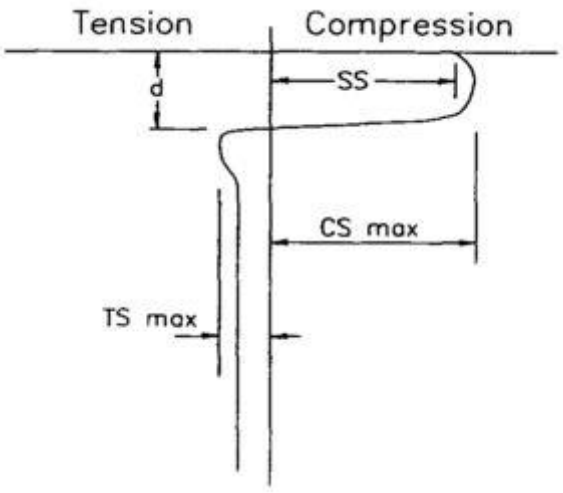

Figure 30.Typical profile of residual stresses due to shot peening[77].

Variation in shot peening factors may have little effect on the magnitude of maximum compressive stress but could influence the depth of the stress profile, and both of these parameters can affect fatigue life. The beneficial effect of shot peening in terms of increasing the fatigue life of a component or material is largely related to compressive residual stress and an optimized/controlled shot peening process, so it is important to consider as to what extent the compressive residual stresses are stable. These compressive stresses tend to relax due to reverse plastic straining depending on loading cycles subjected. Moreover, exposure to high temperature also helps in relaxing the compressive stresses but this stress relaxation does not affect the depth of the residual stress field[78].

Failure due to foreign object is a rather complex phenomenon that brings contact mechanics, crack mechanics and fatigue together. In the real FOD induced fatigue failure in microturbine of AORA, there could be many factors as described above playing simultaneous roles for ultimate failure of the material and it is difficult to isolate effects of each factor. Moreover, there is not much specific information and detailed study of FOD induced fatigue failure as experienced by AORA's CSP facility due to ceramic materials in form of chunks, debris, etc. The aforementioned effects of FOD were mostly studied as it pertains to FOD observed in aircraft engines but it is believed that similar effects of FOD and shot peening are likely to occur in AORA's system and to simulate AORA's FOD condition, a lab scale FOD testing setup using ceramic powder as foreign object was developed and is described in experimental section along with other experiments.

3.OBJECTIVES

There is a need to quantify the mechanical behavior of metallic alloys used in concentrating solar power applications at temperatures approaching and often surpassing those listed as upper limits by the material manufacturers. The quantification of the mechanical behavior represents an important aspect of the overall problem that has direct and immediate practical application.

As described in chapter one there is little significant data available on the effect of foreign object damage on the fatigue behavior of the metallic alloys of interest to AORA, especially on the effect of FOD produced by small particles. The proposed work is to simulate in the lab the FOD produced by small particles similar to those found inside AORA systems and perform fatigue tests on metallic samples with and without the simulated FOD under temperatures and atmospheres that replicate the conditions found the AORA turbines to understand the structural reliability and basic failure mechanisms in the metallic parts used by AORA. The work of this research is focused on Hastelloy X and Stainless Steel 347, which are AORA's materials of interest. The main hypothesis is that damage observed in AORA's system is due to multisite fatigue damage produced by FOD. The specific objectives for this work that will allow testing this hypothesis are:

- Perform microstructural characterization using Electron Backscattered Diffraction technique and hardness tests before and after the heat treatments to see the change is surface mechanical properties due to high temperature.
- Characterize the debris samples received from AORA with Energy Dispersive Spectroscopy and Powder X-Ray Diffraction to identify the chemical

composition and phases present, which will then be used to decide what kind of particles to use for carrying out FOD experiments.

- Design and build a gas gun to perform the experiment to simulate FOD. The gun needs to have a stainless steel reservoir to collect gas at high pressure, solenoid valve to release the gas, a breach to insure sudden release of the pressure and an appropriate barrel.
- Develop techniques and determine conditions to perform FOD experiments and evaluate the surface damage produced by the FOD on well-characterized surfaces.
- Design and fabricate fatigue specimens of selected metallic alloys for high temperature fatigue experiments with and without simulated FOD in air that fail within a high temperature region produced by available heaters.
- Develop heat treatments for the specimens to create a metallurgical state that is similar to what is expected inside the turbine given its operating conditions, so experiment results are representative of this metallurgical state, rather than of the as received condition.
- Perform tensile tests at room and high temperature (600 °C) to characterize mechanical properties such as tensile and yield strength that can be used to estimate stresses for performing fatigue tests.
- Perform failure analysis, i.e., fractography on the failed ablated and non-ablated fatigue specimen to study damage mechanisms.

4. EXPERIMENTAL PROCEDURE

4.1 Microstructure characterization

Scanning electron microscopy (SEM) and electron backscattering diffraction (EBSD) were used to map the microstructure of Hastelloy X and SS 347. In EBSD, an electron beam is focused on a tilted sample; electrons from the incident beam lose some energy due to elastic scattering events that change the trajectory of incident electron. The trajectories of the electrons generates a paired group of large angle cones representing each diffracting plane that satisfies Bragg's law:

$$n\lambda = 2d\sin\theta \quad (6)$$

The resulting diffraction patterns from Kikuchi bands whose angle and width represent crystalline structure. These patterns are captured and interpreted by specialized software that is able to find the crystal orientation of individual points as the sample is scanned. Then, all points with the same orientation (within a specified tolerance) are assigned to individual grains. The final grain structure is shown in the form of an inverse pole figure map with different colors representing crystal orientations parallel to particular physical direction.

Samples for EBSD characterization were 1cm x 1cm x 0.635 cm rectangular parallelepipeds and polished using SiC paper with grit sizes of 240,600, 800 and 1200 and the final polishing was done on an Allied HighTech Chempol cloth pad with a mixture of 0.05 µm diamond paste and colloidal silica. To collect electron diffraction data EDAX-TSL OIM software was used with following parameters: voltage-20 keV, beam size-1µm, step size- 5 µm, grid shape-hexagonal. Figure 31 shows the schematic of the EBSD data collection.

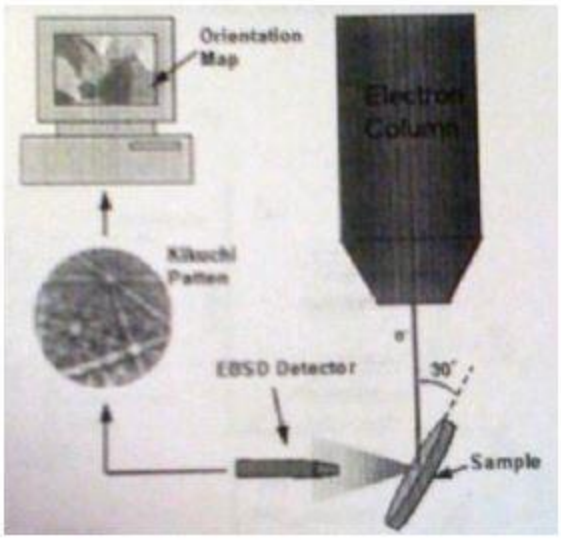

Figure 31. Schematic for EBSD[79].

4.2 Energy Dispersive Spectroscopy (EDS) characterization of debris

Samples of debris were received from AORA as collected from different parts of their system. A key objective of this work was to find out the nature of the debris, e.g., chemical composition and phases present in order to choose the type of particles needed to simulate foreign object damage in the lab. A total of 8 samples were provided in different forms, such as small pieces, granules and soft fabric. These samples were first characterized using energy dispersive spectroscopy (EDS) to identify the elements present in them.

Energy dispersive spectroscopy is an analytical technique used for elemental or chemical analysis. It detects the characteristics X-ray emitted when a focused beam of electrons is bombarded on the solid sample for obtaining chemical analysis. The emitted x-rays are detected by an energy dispersive spectrometer that is capable of separating x-rays with different energy levels. Most EDS system typically consist of a semiconductor detector with a field effect transistor (FET) preamplifier, a main

amplifier that helps in further amplification and a fast pulse inspection function as shown in Figure 32. All of these functions are fully controlled by a computer-assisted system like a multichannel analyzer (MCA) or a computer assisted X-ray analyzer (CXA).

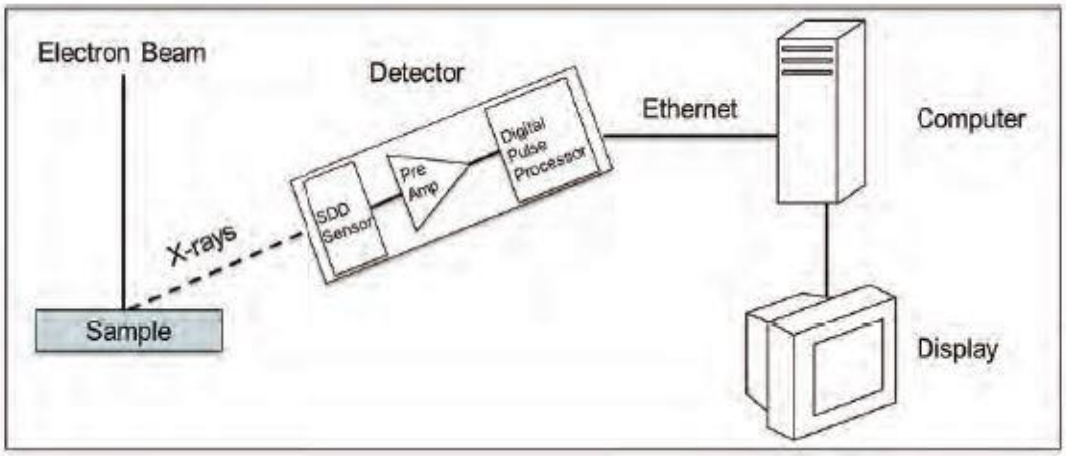

Figure 32. Components of EDS system[80].

The incident electron beam interacts with atoms of that sample that release secondary electrons, backscattered electrons and many other reactions take place in different ways. The characteristic X-rays are generated due to electron transitions between inner orbits that are usually full. In this case, when an electron from the beam hits an atom in the sample, it ejects an electron from its original position in shell (K,L or M) creating a vacancy to be filled out by an electron from an orbit further out. For example, if the vacancy is created in the K shell and it is filled by an electron from the L shell, a K α x-ray is emitted and if the vacancy is filled by an electron from the M shell a K β x-ray is emitted as shown in Figure 33. Similarly if an L shell electron is removed and filled by an electron from an adjacent M shell an L α x-ray is generated.

Also the generated x-rays are denoted by numbers in increasing order(1,2,3...) of the corresponding subshell, L and M have 3 and 5 subshells, respectively[81].

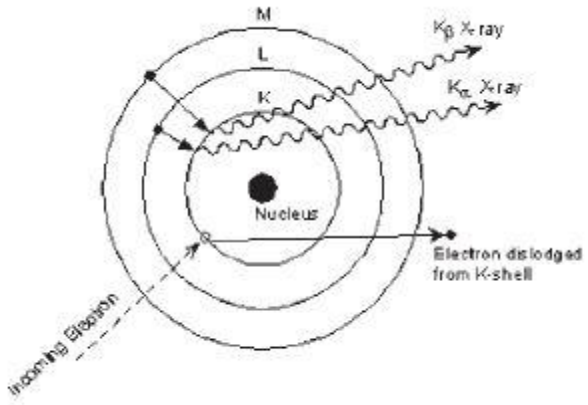

Figure 33. Working principle of EDS[80].

As for EDS instrumentation, the escaping X-rays from the sample hit the detector creating a charge pulse in the detector, this short lived pulse is converted into voltage pulse with an amplitude resembling the detected X-ray energy. The voltage pulse gets converted to a digital signal and one more count is added to the corresponding energy channel. These accumulated counts generate a typical X-ray spectrum shown in Figure 34 having major peaks superimposed in the background.

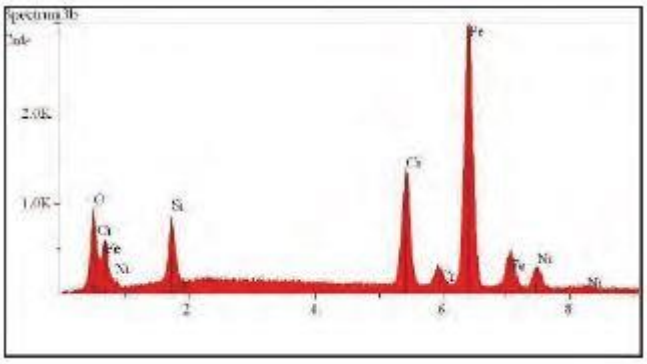

Figure 34. Typical EDS x-ray spectrum[80].

In this work, EDS was performed using a Tescan Vega II Scanning Electron Microscope operating at 20 kV voltage and ~500pA beam current. The scope is equipped with an EDS detector, which detects signals from the sample and shows in form of peaks (counts per second) vs. energy (keV). To get reliable peaks signals were acquired for 120 seconds. The peaks were then analyzed using Genesis EDS software, which matches the position of the peaks with built-in database of energies for different elements present. The appearance of the debris and its secondary electron image are shown in results.

4.3 Powder X-Ray Diffraction(XRD)

Once the EDS step of the characterization process was completed, samples were crushed to a fine powder using a ceramic mortar and analyzed using powder X-ray diffraction. It is a rapid analytical technique mainly used for identification of phases present in crystalline materials pioneered by Max Von Laue in 1912[82].

Diffraction patterns occur when electromagnetic radiation interacts with the periodic structure of crystalline materials. In a diffraction experiment, an incident wave is directed on to a material and a detector is moved to record the intensities of the diffracted waves. Mostly there will be destructive interference of diffracted beams in all directions, as combining waves will be out of phase and there will be no resultant energy leaving the sample. However, as the atoms are arranged in a regular pattern there will be constructive interference in some direction when the condition satisfies Bragg's law ($n\lambda = 2d\sin\theta$). These waves are in phase and define x-ray beams leaving the sample in different directions. The conversion of the diffraction peaks to d-spacing reveals the information about the phase present in the material as each

phase has unique set of d-spacings. When X-rays strike the plane of a crystal they get partially scattered by atoms and the rest passes onto the next layer of atoms to also scatter[83]. Figure 35 shows two parallel incoming x-ray beams on two sets of atomic planes at an angle θ. The interplanar spacing d is equal to the difference in path length of two reflected x-ray beams from top and bottom atomic planes. Constructive interference occurs when $n\lambda$ =AB+BC. Since AB=BC it follows $n\lambda$ =2AB, from Figure 35, AB=dsin θ and hence $n\lambda$ =2dsin θ.

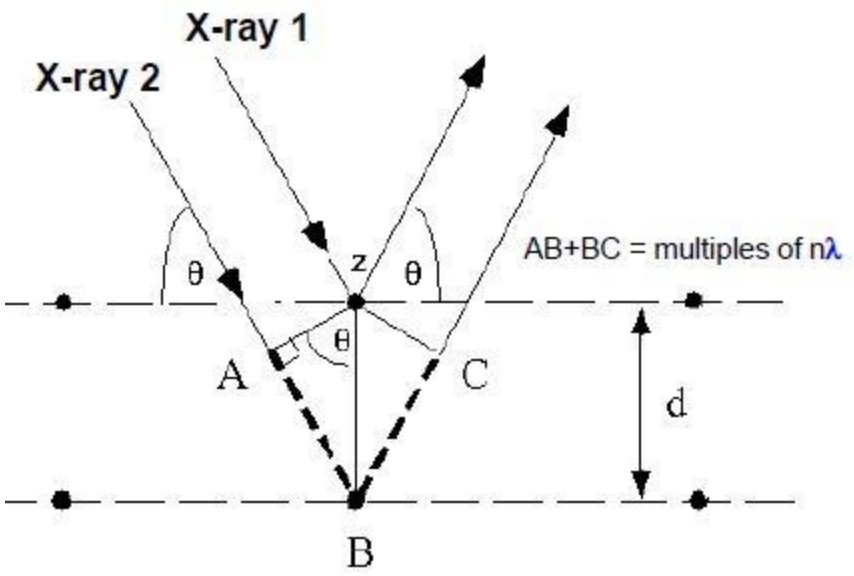

Figure 35. Geometry for interference of wave in Bragg's Law[84].

. A high resolution X-ray diffractometer (PANalytical) was used for the obtaining diffraction patterns and Cu-K α rays with wavelength of 1.544 Å, voltage 45 mA and current 40kV were used for analyzing debris. A powder X-ray diffractometer comprises an X-ray source, a sample stage and a detector. Figure 36 shows the schematic illustration of a diffractometer,

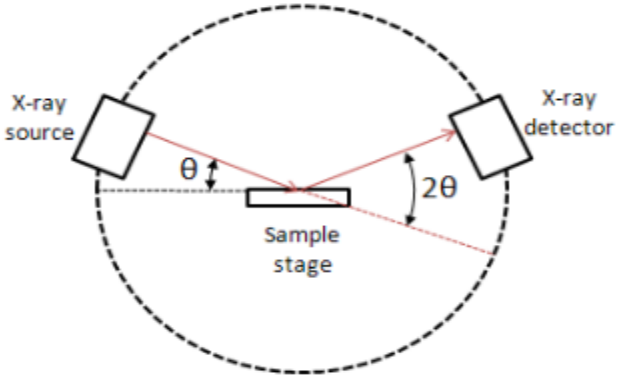

Figure 36. Schematic for X-ray diffractometer[85].

The X-ray is incident on to the sample at an angle θ, and the detector on the opposite side reads the diffracted X-rays at 2θ away from the source. The incident angle was changed gradually from 10° to 90° while the detector angle always stays at 2θ. The peaks obtained during XRD were analyzed by X'pert software using the identified element by EDS. The analysis software matches the peaks to those in a database of known compounds and this process allows the phases present in the sample to be identified.

Characterization of the debris samples allowed choosing alumina particles to simulate FOD in the lab. The experiments to simulate FOD also required a delivery system capable of accelerating the particles to high velocity towards the sample. A description of the system developed to do this is provided next.

4.4 Foreign object damage using gas gun

To perform the lab scale foreign object damage experiment there was a need to built a gas gun that could be used to do FOD experiments at varying angle of

incidence based on the testing procedures described in [86-87], which describe continuous delivery of abrasive particles in a pressurized air stream as shown in Figure 37. Some of the keys aspects from the standard were used and there was also some deviations as the standard itself allows to do, e.g., the system mixing chamber and supply tube were eliminated and instead a barrel was directly placed after the gas supply, the portion beginning of the nozzle was used as abrasive reservoir, the barrel length to diameter was changed from 25:1 to approximately 100:1, a means of controlling angle and velocity were also added by using a flexible sample stage and changing supply gas pressure, respectively. Regarding test time, it was decided to get a maximum amount of particles with gas in the accumulator in a single burst as opposed to the 600s of continuous streaming as recommended in the standard so the erosion rate was not determined due to shorter test time and no apparent loss in the sample mass. The recommended 50 µm Al_2O_3 particles were used as an abrasive particles and a 10 mm distance between specimen surface and barrel exit was used.

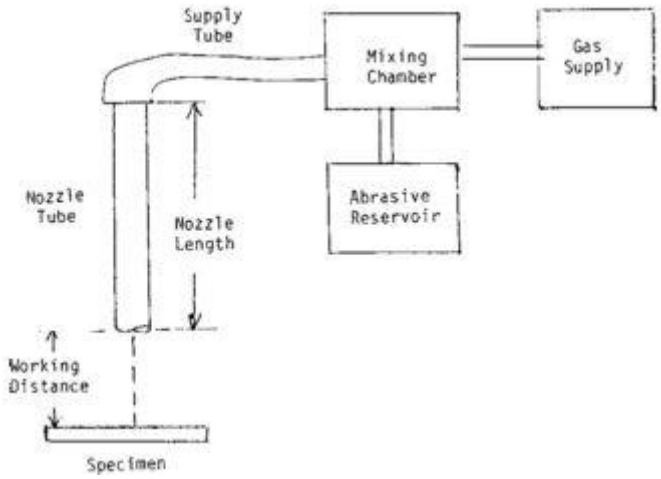

Figure 37 Schematic Drawing of Solid Particle Erosion Test System[86].

The final setup of the gas gun was achieved over a period of time by doing several modifications as required. The building process for gas gun started off with just

having connected a 6 feet long, 1/2 inch diameter cast iron pipe to a 120 psi compressed air outlet, later on some fittings were added to use a breach membrane and abrasive particles. Figure 38 shows the initial setup of the gas gun.

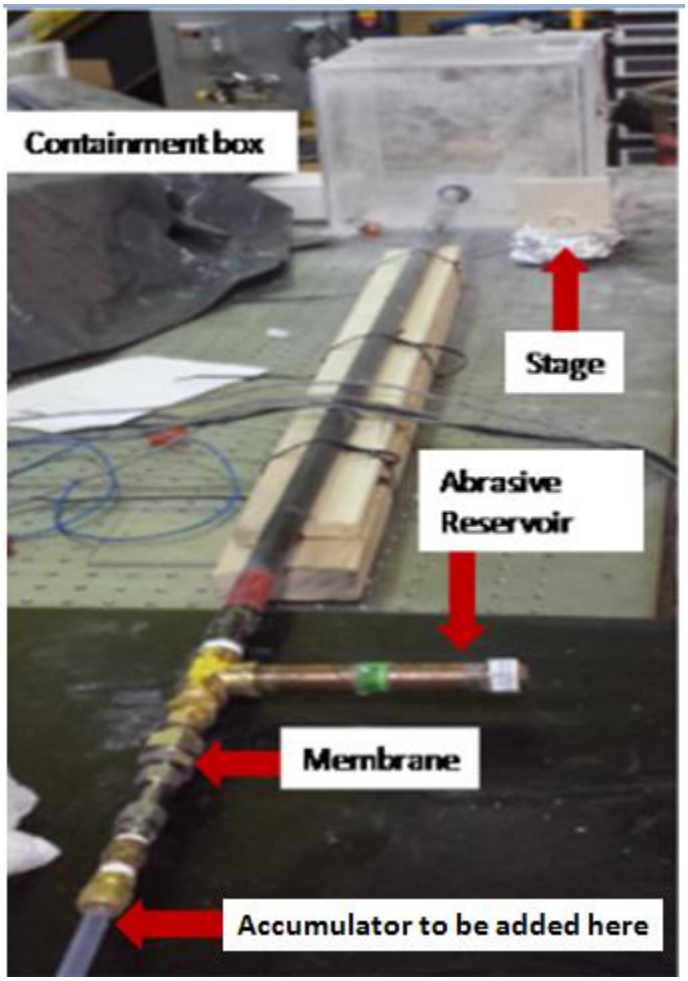

Figure 38. Initial setup for the gas gun.

It can be considered as a single stage gas gun consisting of two main elements: a reservoir to fill the gas and a launch tube that guides the projectile[88]. Higher velocity of the projectile (powder) can be achieved by increasing the initial reservoir gas pressure. Furthermore, it shows the point where an accumulator with a maximum capacity of 1800 psi would be placed to collect gas at a known pressure. The stage shown here is a rotating platform to control the angle of incidence of the particles.

Controlling the angle is really important since the amount of material removal from the surface depends on the angle of incidence, and the maximum amount of wear for ductile materials occurs close to 23°[57]. A solenoid valve rated for 1200 psi that provides fast acting opening and leads to transient flows during the release of gases from the accumulator was added to this setup. This transient behavior is key to achieve high velocities [88]. The system is, therefore, designed to operate in bursts, which is the suspected mode of erosion/damage due to particles in AORA's turbines.

After adding the accumulator and the solenoid to the preliminary setup, FOD experiment trials were carried on Inconel 625 dogbones whose impact behavior is shown in the results section. Further modifications were made to the gas gun setup and it was upgraded to all stainless steel parts to make it capable of performing FOD experiments at high temperature, although those experiments are beyond the scope of the present work. Figures 39 shows the final setup of gas gun. The setup shown here has a membrane "breach" set after solenoid valve that can be used to deliver sudden expansion of gases to achieve higher particle velocities, while also allowing the delivery of a steady stream of particles at lower velocities to induce wear over longer periods of time [88]. Sample holding for this setup was changed from the previous rotating stage shown in Figure 38, and unistruts were used to make two T joints and on the vertical leg L brackets were clamped so that the sample can rest onto it. This holder allows moving the position of the vertical legs to achieve the desired angle of shooting, since the amount of materials removal from the materials surface depends on the incident angle of shooting particles.

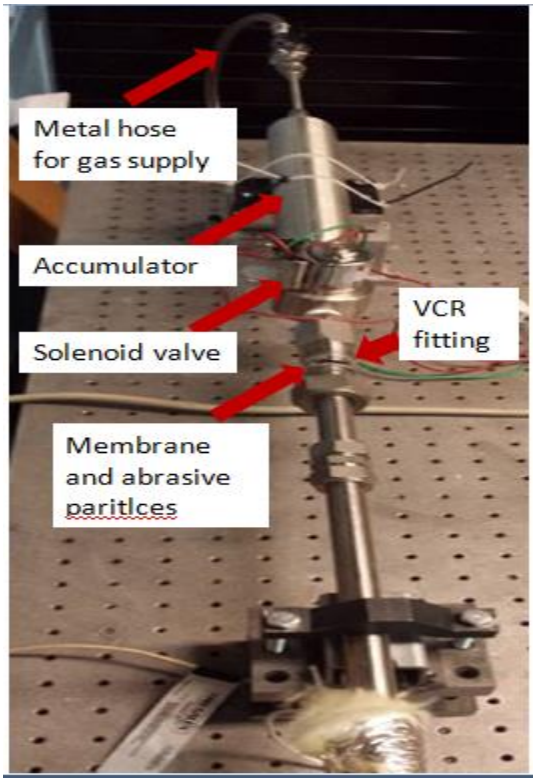

(a)

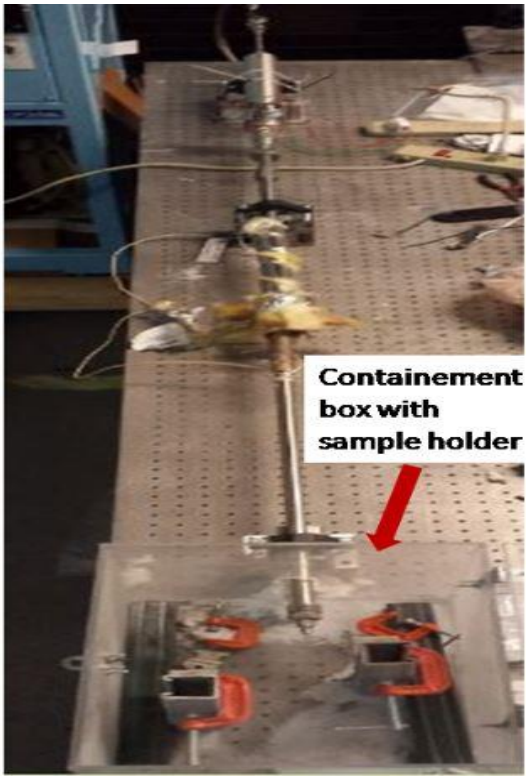

(b)

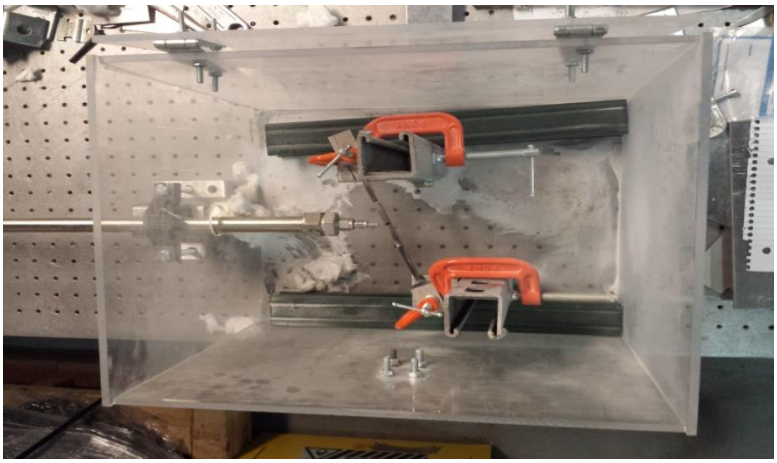

(c)

Figure 39. High temperature gas gun setup and details of the sample holder.
The L brackets can be adjusted up and down with C-clamps on the vertical leg such that the side of the sample sits in front of the gas gun nozzle, as shown Figure 39c.

To perform FOD experiments the VCR fitting, labeled as such in Figure 39a, is opened to slide the barrel in order to feed in 5 gms of alumina particles and then it is

closed by carefully inserting a Mylar film as a breach membrane in between (labeled in Figure 39a). After this the sample is set at the desired height and angle by adjusting the vertical legs and height of the C clamps such that side of the sample to be shoot sits in front of the nozzle. Then, while keeping the regulator valve on the nitrogen cylinder closed, the main valve on the nitrogen cylinder is opened, followed by opening of the regulator valve till the low pressure gauge reading is 0.96 MPa (140 psi). This will fill the accumulator with nitrogen gas at that pressure. The solenoid valve is then plugged in the socket, triggering the power on will cause the solenoid valve to open quickly, which releases the gas contained in the accumulator. This gas, in turn, will break the Mylar membrane leading to the sudden expansion of the gases, which take the Alumina particles with them as they expand along the barrel and propel them at high velocity towards the sample.

The velocity of the projectile keeps increasing as it moves along the barrel, but the base pressure decreases, and this continues till the particles reaches to exit nozzle of the barrel. The velocity of the gases is estimated from the typical design equation used for gas guns[88].

$$\frac{p_0 SL}{M} = \frac{2a_0^{\,2}}{\gamma+1}\left[1+\frac{\frac{(\gamma+1)v}{2a_0}-1}{\left[1-\frac{(\gamma-1)v}{2a_0}\right]^{\gamma+1/\gamma-1}}\right] \quad (7)$$

Where p_0 and a_0 = value of pressure and sound velocity of the working gas at the initial time, v = velocity of projectile, γ = ratio of specific heats, S and L are the cross-sectional area and length of the launch tube (barrel) and M is the mass of the projectile (abrasive particles).

The FOD experiments on samples for fatigue testing were done at 140 psi (0.96 MPa) using 5 gm of alumina particles. By solving Eq. 7 for known pressure, geometry of the barrel, gas properties and projectile mass the velocity for the tests was estimated to be near ~200 m/s.

4.5 Fatigue sample fabrication and polishing

All the samples for FOD and thermomechanical fatigue testing were fabricated from 6.35 mm (1/4 inch) thick plates of Hastelloy X and SS 347.

Two sample geometries and two gripping arrangements were explored for thermo-mechanical fatigue testing. Figure 40 shows the dimensions for the first sample geometry and gripping arrangement used, i.e., the bottom grip, top grip and dogbone. All dimensions shown in the figure are in mm.

The dogbone samples with the geometry shown in Figure 40c were then polished on all four sides of the gauge length, which was necessary to create a baseline surface with known roughness so that the effect of damage left by particles could be quantified by comparison to a known initial condition. Polishing very long dogbones uniformly is difficult and cannot be done using conventional polishing equipment; therefore, a tabletop Sherline Model 5100 CNC end mill was used to polish the sample, as shown in Figure 41. A spring-loaded tool was attached to the spindle and at the bottom of the tool a circular flat disc can be inserted.

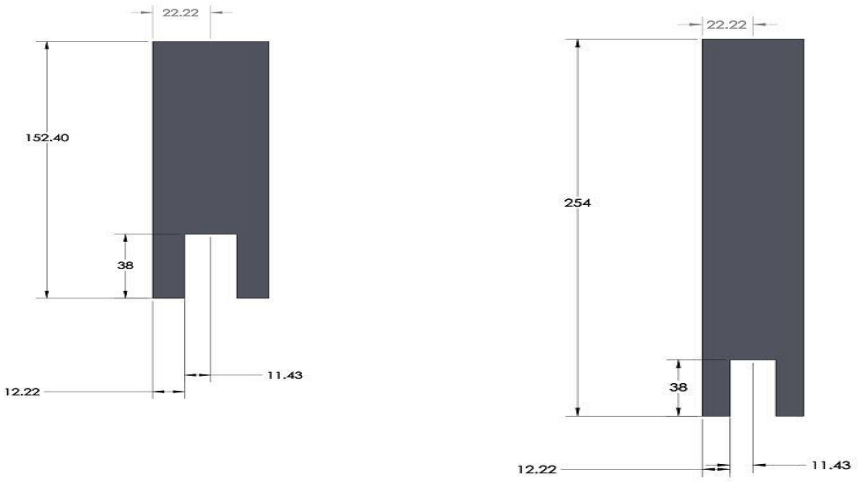

(a)

(b)

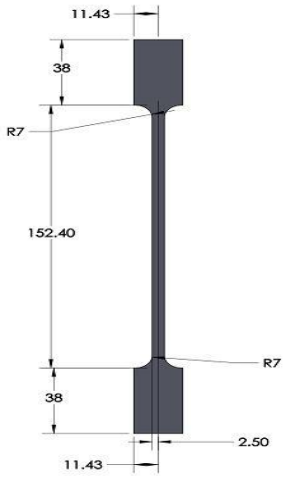

(c)

Figure 40. a) Bottom grip, b) Top grip c) Dogbone fatigue sample.

Figure 41. CNC machine for polishing samples.

Different grit size papers and polishing cloths were used by attaching them on to a flat disc. A CNC code was written such that it followed and covered the gauge length and polished uniformly and one fully polishing cycle could be repeated the desired number of times. The initial roughness from the raw material was removed using very coarse SiC paper grit size 60, 80 or 120, and then the surface was further smoothed by polishing successively using 240, 600, 800 and 1200 grit SiC paper. No polishing agents like colloidal silica or diamond paste were used except for the Inconel 625 sample. The square samples for EBSD and hardness test were polished using manual hand polisher from grit size 240 to 1200 and subsequently by a mixture of 0.05 µm colloidal silica suspension and 0.05µm diamond paste.

The polishing served as the first step in preparing samples for further experiments such as Vickers hardness, EBSD and fatigue tests.

4.6 Vickers Hardness and High temperature indentation

Vickers hardness is a very convenient and useful technique to evaluate mechanical properties of a material. Higher loads increase the penetration and size of the indents, which can give information about the average behavior of a large number of grains, while lower loads can give information about local grain clusters due to a smaller indent size. Therefore, information on the mechanical behavior at different length scales can be obtained using this method by making numerous indents with different loads on the same sample. Indentation testing was performed using a Leco M-400-H2 micro-indentation hardness tester and it performs Vickers hardness measurements with a four-sided pyramid diamond indenter that is pushed into the material to be tested under the desired load for 10 seconds. This will leave a mark on the surface the size of which can be measured by a microscope and micrometer attachment to the tester. The size of the indent can then be calculated knowing the load and the size of the indent using the following formula[89].

$$HV=1.8544*P/d^2 \quad (8)$$

Where, P=force in kgf, d=mean diagonal length of the indent in mm.

Hardness tests under different conditions were performed: a) hardness at room temperature 2) hardness on heat treated samples 3) hardness after FOD experiments and heat treatment to see the effect of different conditions and environment on the properties of the materials.

These different conditions were chosen to understand the effects of heat treatments and surface ablation when compared to the as received raw material since they mimic

AORA's turbine operating conditions, i.e., high temperature on solar mode as well as foreign objects striking the turbine parts during operation.

High temperature indentation experiments were also performed using a servo hydraulic load frame in an inert atmosphere to see the change in plastic behavior of materials at different temperatures. The setup is shown in Figure 42.

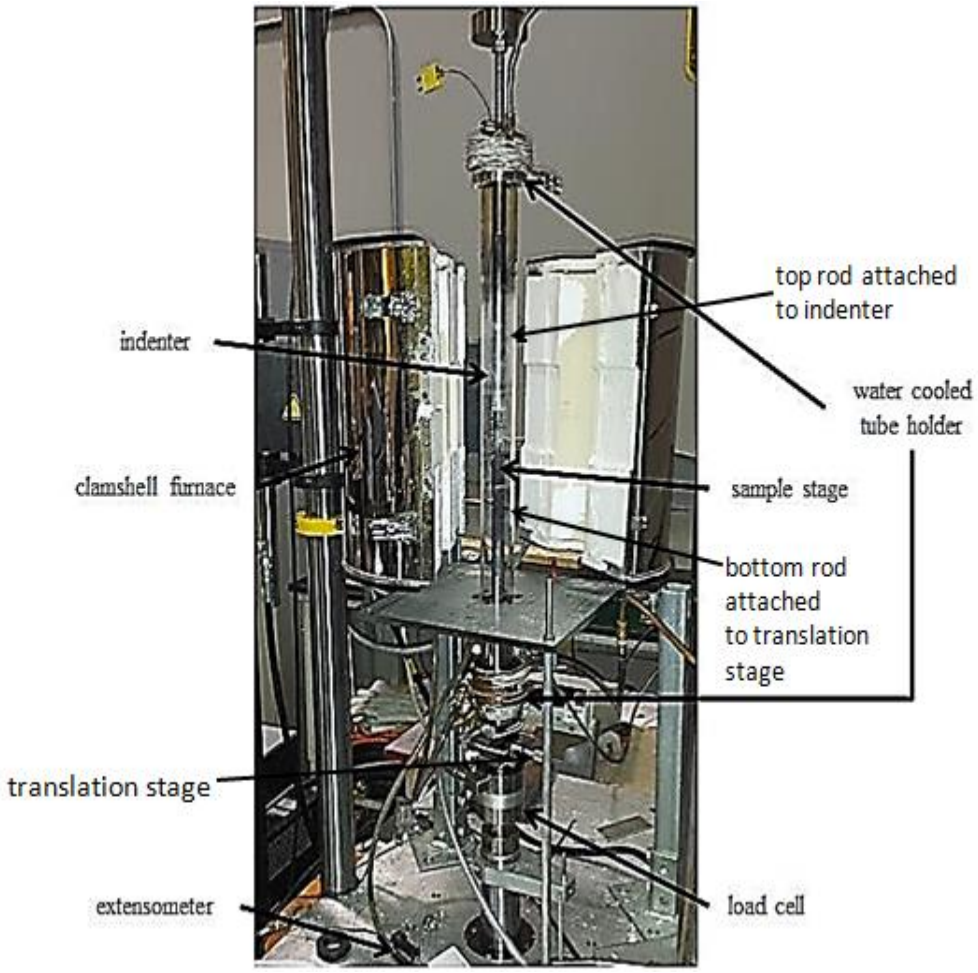

Figure 42. High temperature indentation assembly.

The sample was set on the bottom vertical rod made of TZM alloy and an indenter was attached upside down to the top vertical rod, the bottom rod was attached to a translation stage that allowed moving the sample to perform several indents. These rods were enclosed in a quartz tube to create an inert atmosphere using

Ar-5% H_2 to avoid the oxidation of the sample. The end caps on the quartz tube were water-cooled to avoid heat transfer to the load cell.

. As shown in Figure 42 the quartz tube was then held inside a clamshell furnace to control the temperature. Indentation tests were performed under load control at three different temperatures, 900°C, 700 °C and 550°C starting from highest to lowest to avoid changing the metallurgical state of the material for each set of indents. The data was recorded as load vs. displacement. A load of1 kgf was as well as a WC indenter of 1/16" size diameter.

4.7 Fatigue test gripping design

To perform the high temperature fatigue tests there was a need to come up with a gripping design since the initial setup of the load frame was not equipped with a high temperature grip that could be placed inside the furnace to grip the sample. The grips were designed to keep the actual specimen on the uniform temperature zone of a newly acquired Mellen furnace, while they extended all the way outside of the furnace itself, so they can be attached to servo-hydraulic grips outside of the hot zone. Water-cooled servo-hydraulic wedges were installed to solve the problem of the high temperature on the gripping area during testing. Since the furnace was long and making long tests specimens was not cost effective, it was decided to weld the dog bones samples to extension grips to be cost effective and yet serving the intended purpose of gripping outside the furnace. Extensions to the gripping section of regular dogbone samples were designed and fabricated from 310 stainless steel, and attached to the samples using TIG welding, as shown in Figure 43.

Figure 43.Extension grips welded to a dogbone sample for high temperature tests.

The final fatigue test design and setup was improved over time with modifications and upgrades over the course of the test program. The design was tested at room temperature and 550 °C during a fatigue test, to make sure that the welds and the extensions themselves, which were much wider than the sample, could take the loads. Previous iterations of the design failed at room temperature at the welds, which led to changes to improve them. The tests were performed under load control using a sine wave with a load ratio R (min. load/max. load) of 0.1 at a frequency of 10 Hz. The sample shown in Figure 43 was made of Inconel 625, had a gauge length cross-section of 6.35x6.35 mm^2 and was tested at approximately 20,000 N, which resulted in a stress of about 720 MPa. The sample experienced approximately 70,000 cycles under pull-pull conditions and failed at the gauge length and showed a fracture surface with typical fatigue characteristics, e.g., beach marks.

The same experiment was performed at 550° C using a clamshell furnace as shown in Figure 44, with a stress level of 660 MPa, and under high temperature the sample

experienced 22,000 cycles. These experiments indicated that the TIG welding was strong enough to sustain the load at high temperature and would allow the sample to break at the gauge length. It was decided to go ahead with the initial design to carry out the fatigue test. However, there were issues with this design as the samples had a longer than expected fatigue life for high levels of stress, which was attributed to residual stresses due to the welding process (some samples bent during welding). This led to additional modifications of the testing procedure.

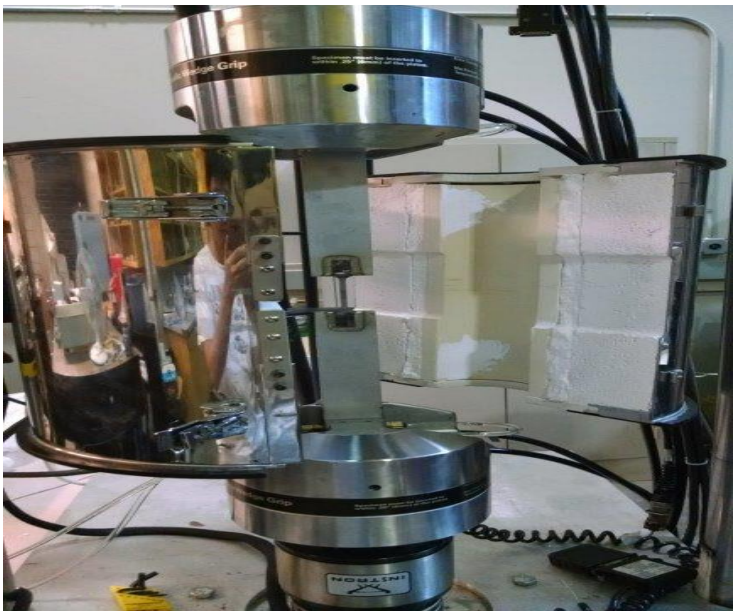

Figure 44.High temperature fatigue test setup showing grip extensions welded to the samples.

The heating source was replaced with a Thermcraft heating element, as shown in Figure 45 to test the sample with same design but without welding grips. Even with these heating source change sample had a longer than expected fatigue life and failed outside the heating zone, which could be due to a sharp radius at the gripping section.

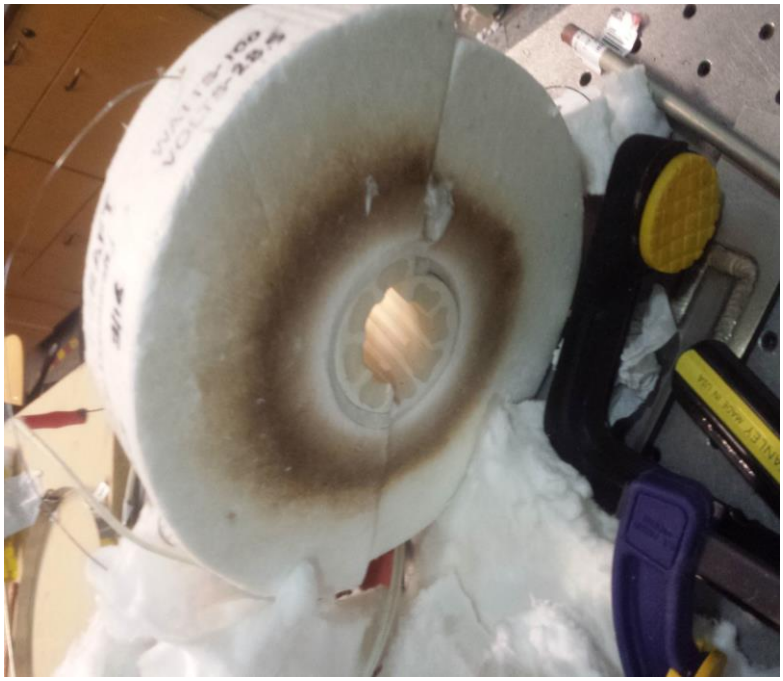

Figure 45. Thermcraft heating element.

This led to the decision to change the design of the sample to have a gentle radius for most of the gauge length, but with a straight section right at the middle, as shown in Figure 46.

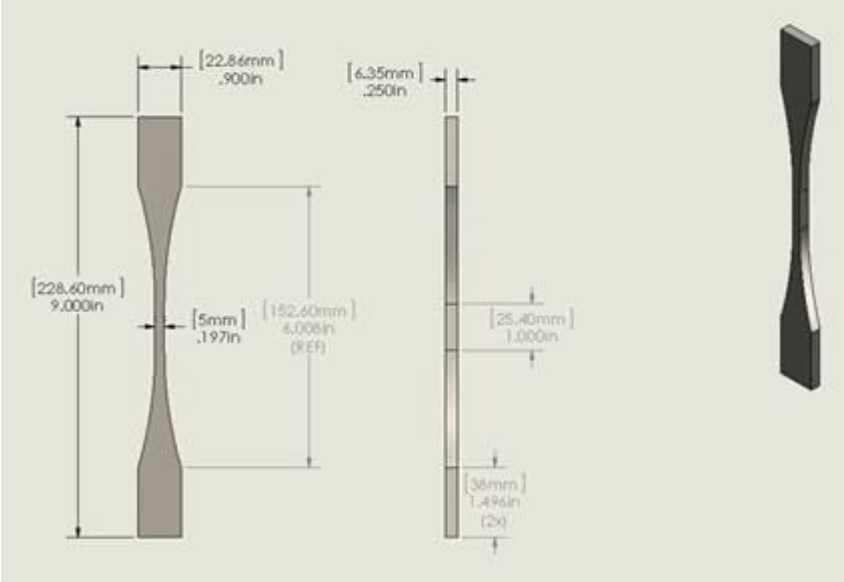

Figure 46. Dimensions for re-designed fatigue sample.

4.8 Fatigue test stress estimation

There is only limited data available for the chosen materials for fatigue endurance behavior, i.e., S-N curves specifically at high temperatures. Hence, the stresses to be used in the fatigue tests were estimated from the high temperature tensile properties and Basquin's equation[90]

$$\sigma_f = AN_f^b \quad (9)$$

where σ_f = stress for failure, N_f= number of cycles to failure, A & b are constants.

A general rule of thumb, for steels, is that 90% of ultimate tensile strength (UTS) gives 10^3cycles and 50% of UTS give 10^6cycles [91]. This rough approximation was used to solve Basquin's equation to get the stress required for 10^5 cycles, which was considered long enough to represent high cycle fatigue behavior, but short enough that tests could be carried out in a reasonable amount of time.

Room temperature tensile tests were performed on as-received material and after heat treatment. Tests at high temperature (600 °C) were performed after heat treatment for 8 hours on Hastelloy X at 1000 °C and SS 347 at 950 °C, since these temperature are likely to occur in AORA's system in solar mode. Given that one can assume that during the day time AORA's system runs on solar mode only, 8 hours was selected for heat treatment. Tensile tests were carried out in displacement control mode with displacement rate of 1mm/min. The properties obtained are described in results section and an example of solving Basquin's equation is shown for Hastelloy X using the high temperature UTS (575 MPa) is given below.

Using the general rule of thumb mentioned above and substituting it in Basquin's equation gives:

$$518 = A(10^3)^b \quad (*)$$

$$288=A(10^6)^b \quad (**)$$

Solving (*)and (**) for *A* and *b* gives A=938 and b=-0.086. Using these values in Basquin's equation, the stress value for 10^5 cycles can be obtained as:

$$\sigma_f = 938(10^5)^{-0.086} = 347 \text{ MPa}$$

Similar calculations were performed using room temperature tensile properties coupled with percentage drop in UTS from room temperature to high temperature. Comparing the calculated values with the stresses used for the past experiments, the final stress value for Hastelloy X and SS 347 were chosen to be 440 MPa and 340 MPa, respectively. High temperature fatigue test were performed using these values, the setup and procedure of which are described next.

4.9 Fatigue test setup and procedure

The Thermcraft heating element has each half rated for 28.5 volts, 100 watts with maximum temperature up to 1200 °C. The smaller 2 inch length of this new element, as compared to the clamshell furnace initially used, allowed the sample to be gripped directly at the ends, but it reduced the sample length under high temperature. Since this heating element is much smaller than the larger furnace, which has much less heat dissipation, the temperature distribution was not expected to be very uniform and the highest temperature is likely to be at a spot or a few millimeters at the center of the heating element.

One of the consequences of using the Thermcraft heating element is that the actuator was sitting close to the heating element as compared to the sample with the welded grips sections. This, in turn, increased the chance of more heat flow to the water-cooled wedges, where heat is removed by water flowing through connected plastic tubing. There was a concern that plastic tubing might burst if the wedges

reached 100 °C, so the plastic tubing was replaced with copper tubing to overcome this issue. Figure 47 shows the test setup with the new heating element. A mount was built such that heating element would sit at the middle of the gauge length. It was decided to use the same stresses that were used to test the samples with the welded grips. Heat dissipation was reduced by using cloth insulation around the sample such that it stayed in the centerline of the heating element, and more insulation was used on the top and bottom of the element. A thermocouple was then inserted in such a way that it stayed closer to the sample surface near the middle of the gauge length, where the temperature was expected to be the highest.

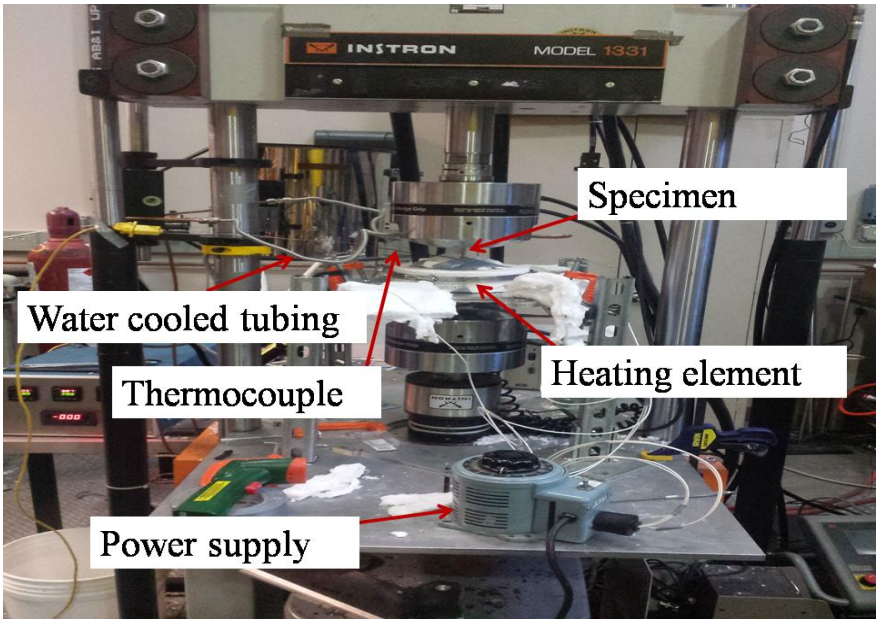

Figure 47. Fatigue test setup using Thermcraft heating element.

The samples for fatigue test were heat treated at the higher end of the temperatures for 8 hours experienced by metallic components inside the AORA turbine, Hastelloy X at 1000°C, SS 347 at 950°C as described earlier. The tests were then performed under load control using a sine wave with a load ratio R (min. load/max. load) of 0.1 at a

frequency of 10 Hz using stress value of 440 MPa and 340 MPa for Hastelloy X and SS 347 respectively.

The results for the experiments described in this chapter are discussed next.

5. RESULTS AND DISCUSSION

Results from experimental work are shown and discussed in this chapter, starting with metallurgical characterization of the metallic alloys of interest, Hastelloy X and SS 347. This is followed by characterization of debris provided by AORA, so that appropriate surrogates could be selected for foreign object damage (FOD) testing. Preliminary results from ablation tests on a Ni-based alloy are reported as well. Measurements from high temperature spherical indentation, hardness and tensile tests at room and high temperature results are also shown. Lastly, results from fatigue tests in terms of fatigue lives, fractography analysis, damage mechanism, characterization of microcrack patterns present on ablation sites and its relation to crack initiation are discussed for Hastelloy X and SS 347.

5.1. Microstructure characterization using EBSD

Techniques to characterize microstructure and composition of 347 SS and Hastelloy X were developed. Figures 48 and 49 show results for SS 347 and Hastelloy X, respectively.

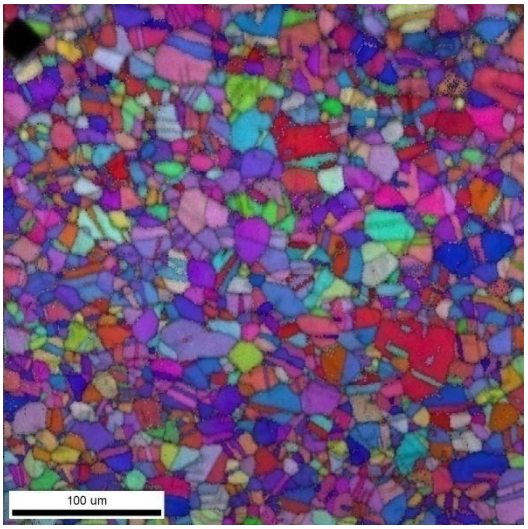

(a)

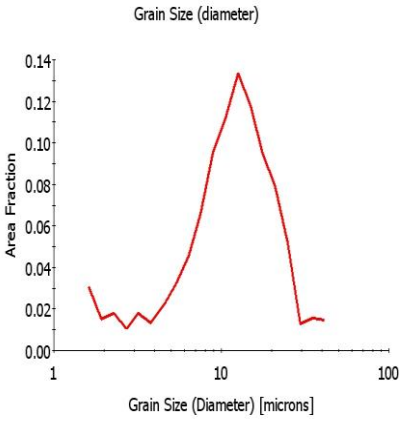

(b)

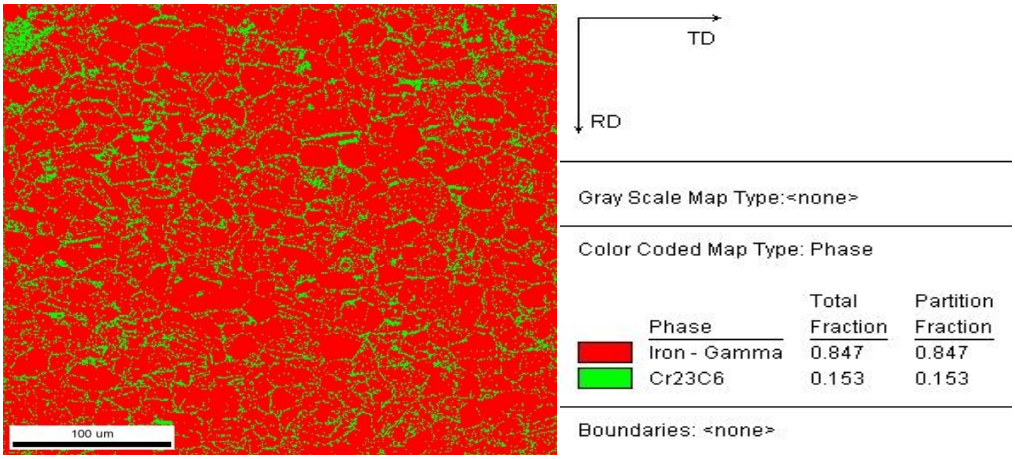

(c)

Figure 48. Microstructure data for 347SS obtained from EBSD. (a) Inverse Pole Figure. (b) Grain size distribution. (c) Phase map (red is austenitic phase, green is chromium carbide).

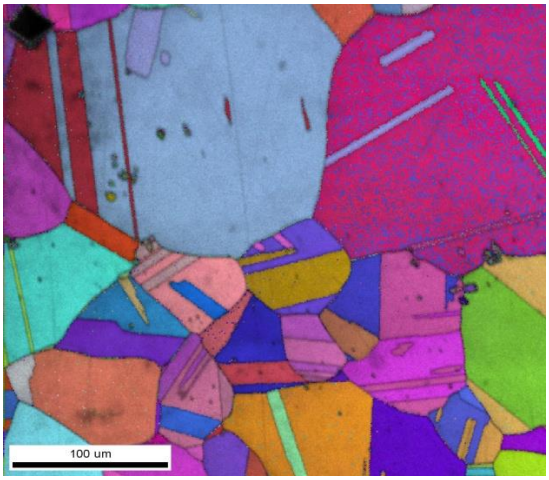

(a)

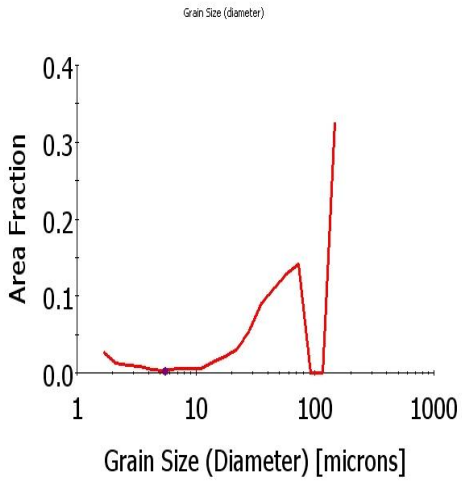

(b)

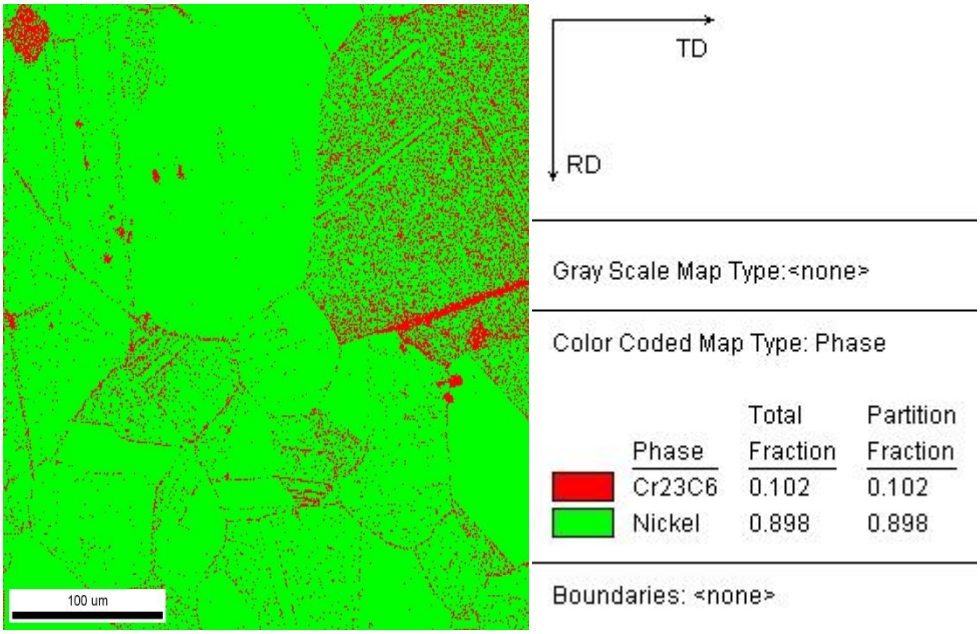

(c)

Figure 49.Microstructure data for Hastelloy X obtained from EBSD. (a) Inverse Pole Figure. (b) Grain size distribution. (c) Phase map (red is chromium carbide, green is nickel).

Results for the stainless steel and Ni-based superalloy of interest show that carbides can decorate grain boundaries, as expected, since this is a typical creep

strengthening mechanism in these alloys[50]. Occasionally, however, grain boundaries were covered with a continuous film of carbides, and this is detrimental to high temperature strength[51]. Unfortunately, the measurements done did not have enough resolution to get the actual size of the carbide precipitates and noise due to uncertainty of crystallographic indexing at the boundaries compounds this problem. The results showed that materials had a wide grain size distributions, as can be seen in Figures 48b and 49b, and that can lead to localized fatigue damage (large grains) or creep (small grains)[92]. These wide distributions are somewhat consistent with increased scatter of hardness measured at room temperature at low loads compared with the scatter at high loads, as will be shown in the discussion of hardness results.

5.2. XRD and EDS Characterization of Debris

The following samples were provided by AORA from different locations in their system:

1)Distributor: A part of the receiver attached to the microturbine**.**

2)Combustor-in: Inlet of combustion chamber through which air enters the combustor section.

3) Combustor section: It is an area of a turbine where highly pressurized air is fed for combustion.

4) Swirl: It is a part of combustor section through which air flows into the combustion zone. Its function is to create turbulence in the flow to mix air and fuel rapidly (see Figure 50).

5)Pilot wall: The pilot is a central hollow part of the swirl, which supplies fuel for initial startup of combustion (see Figure 50).

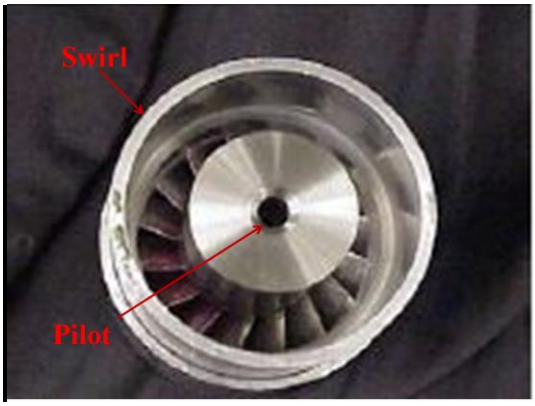

Figure 50. Example of swirl and pilot in a gas turbine setup [93].

6)Nozzle: The nozzle is the ring of vanes that guides the flow of the working fluid from the combustor into the turbine (see Figure 51)

Figure 51. Example of a nozzle in a gas turbine setup[94]**.**

7) Volute inlet and 8)Volute outlet: The volute is a casing for the turbine. The combustion gases enter through the volute inlet and exit through the outlet.

The samples provided by AORA were analyzed using XRD and EDS, as well as SEM. Images of their appearance at low magnification are shown in Figure 52.

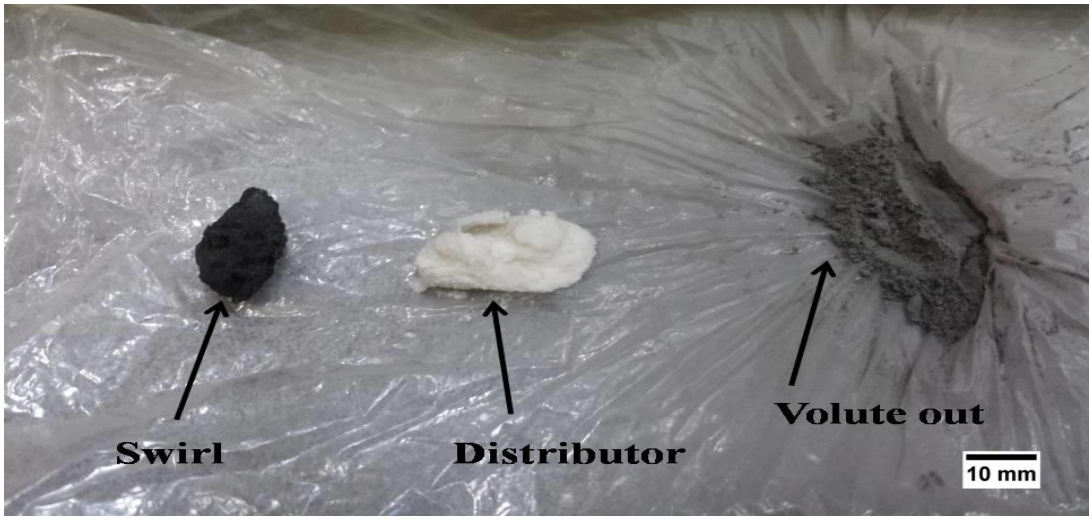

Figure 52. Examples of debris specimens provided by AORA: Swirl, Distributor, and Volute out.

Samples came in different forms, such as small fragments, granules and soft fabric. The EDS spectra and XRD peaks obtained from the samples "Distributor", "Combustor in", "Combustor section" and "nozzle" are shown in Figures 53, 54, 55 and 56 respectively.

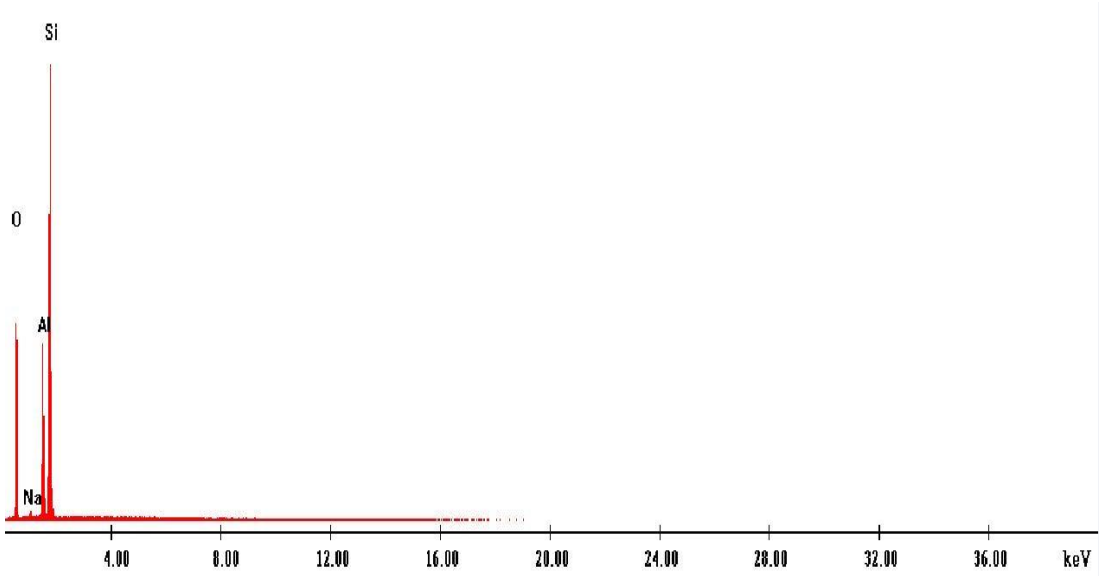

(a)

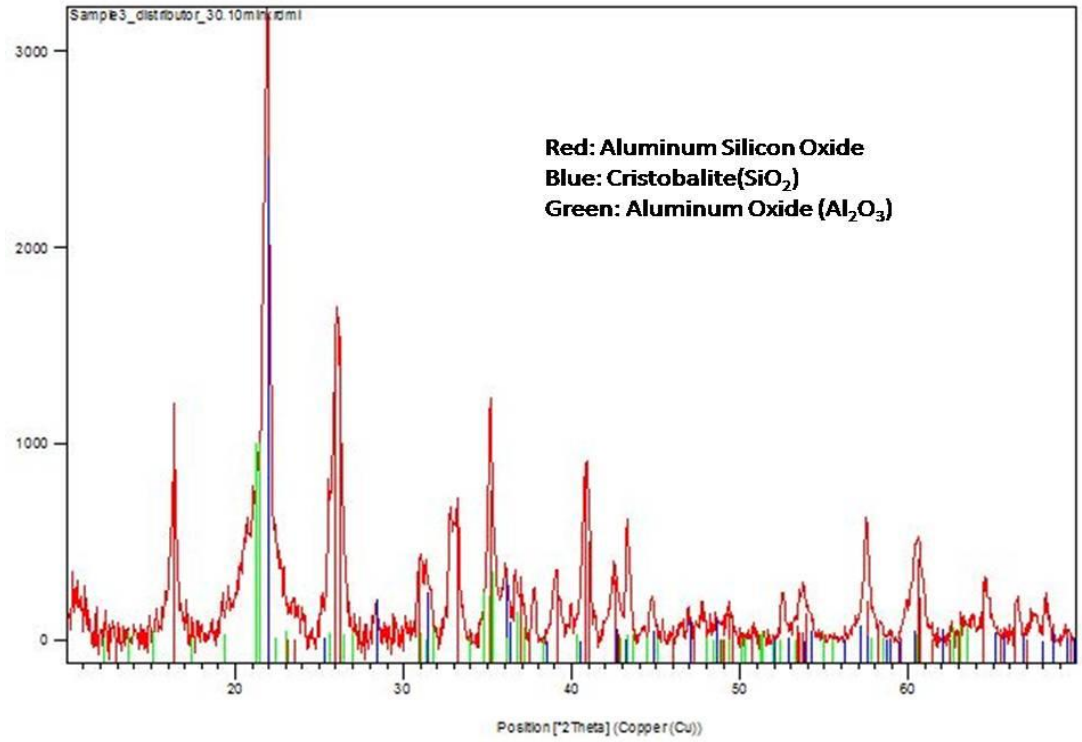

(b)

Figure 53. Results from the Distributor sample. (a) Spectrum from EDS. (b) Diffraction pattern from x-rays.

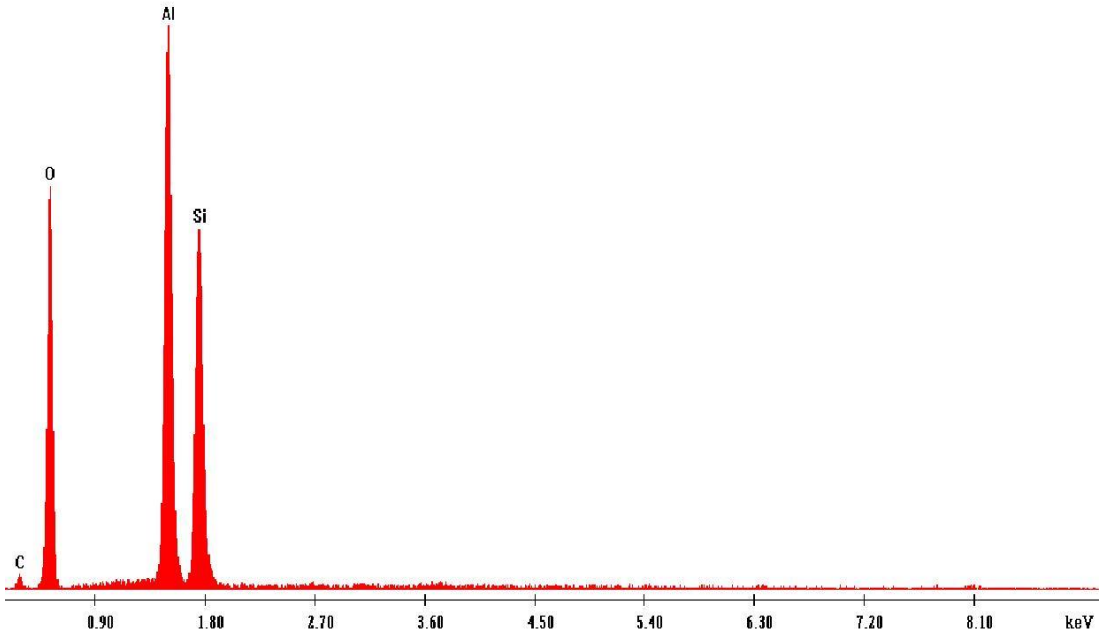

(a)

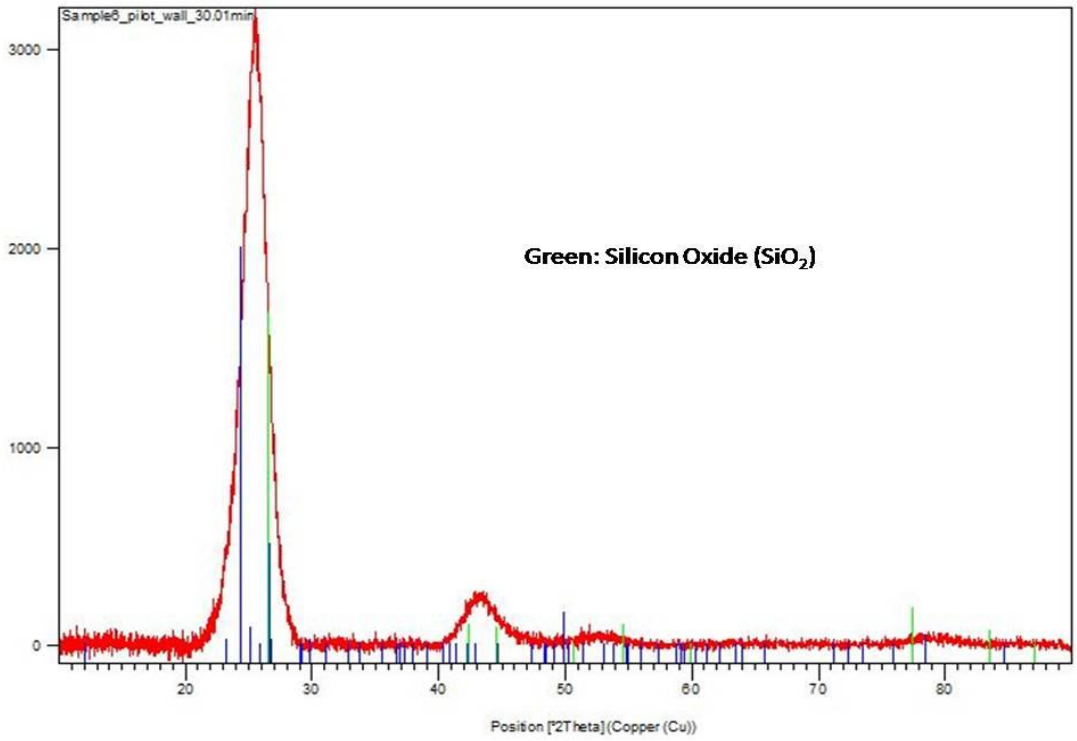

(b)

Figure 54.Results from the Combustor sample. (a) Spectrum from EDS. (b) Diffraction pattern from x-rays.

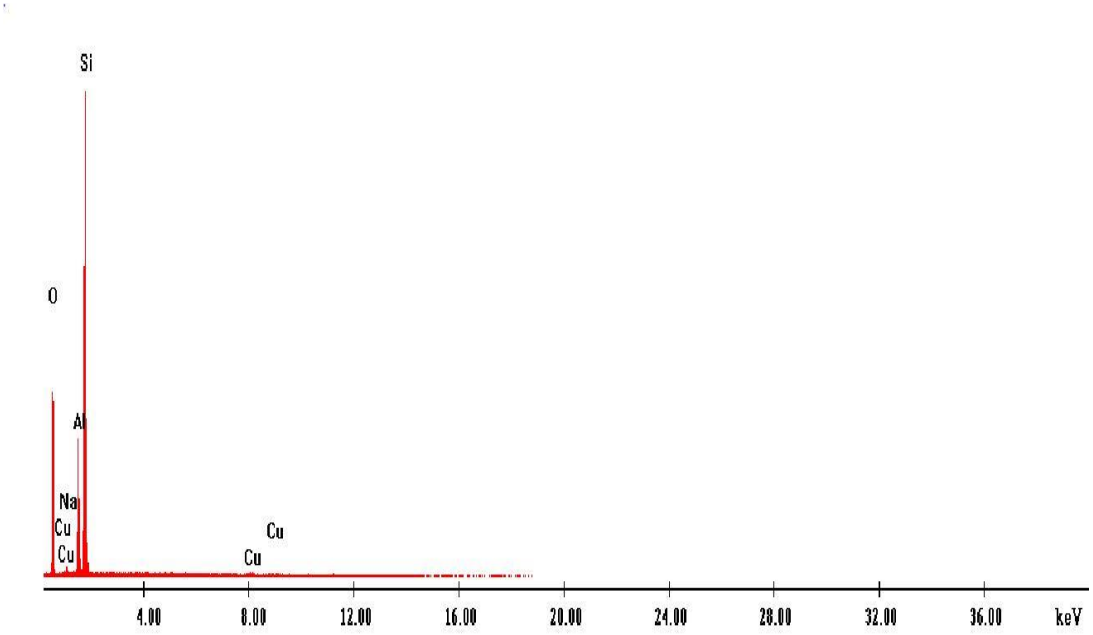

(a)

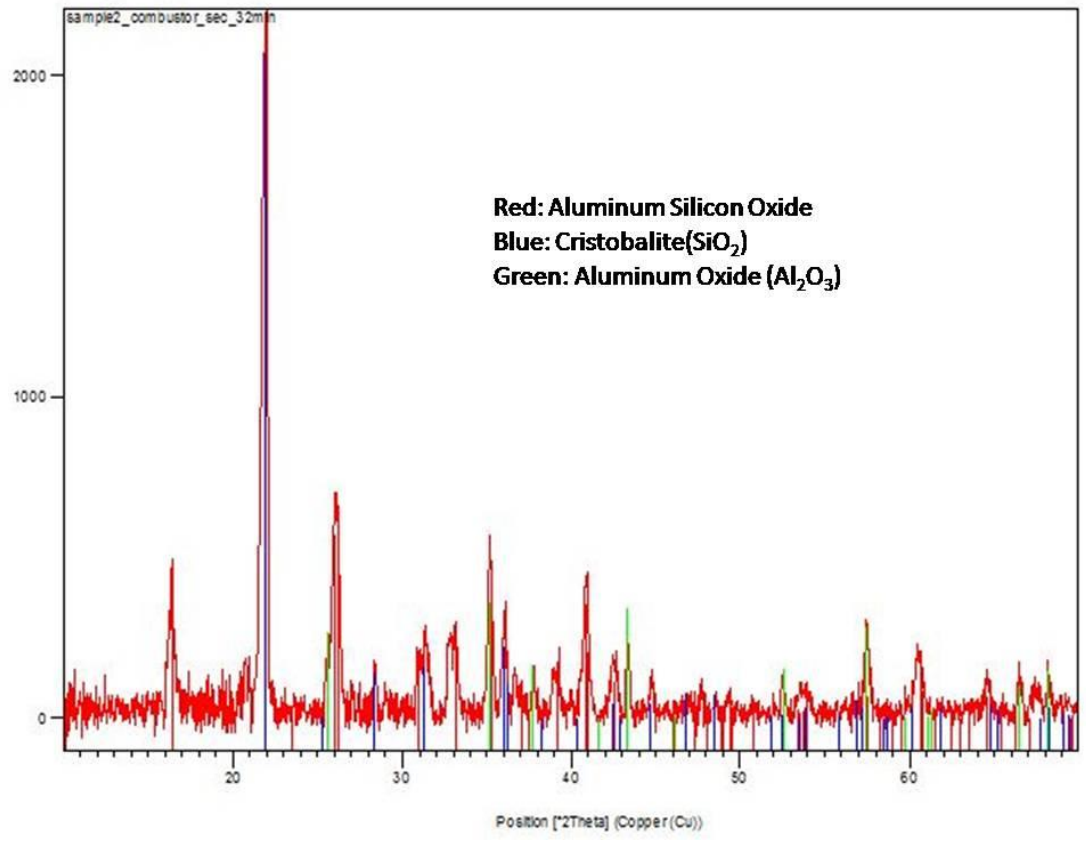

(b)

Figure 55. Results from the Combustor section sample. (a) Spectrum from EDS. (b) Diffraction pattern from x-rays.

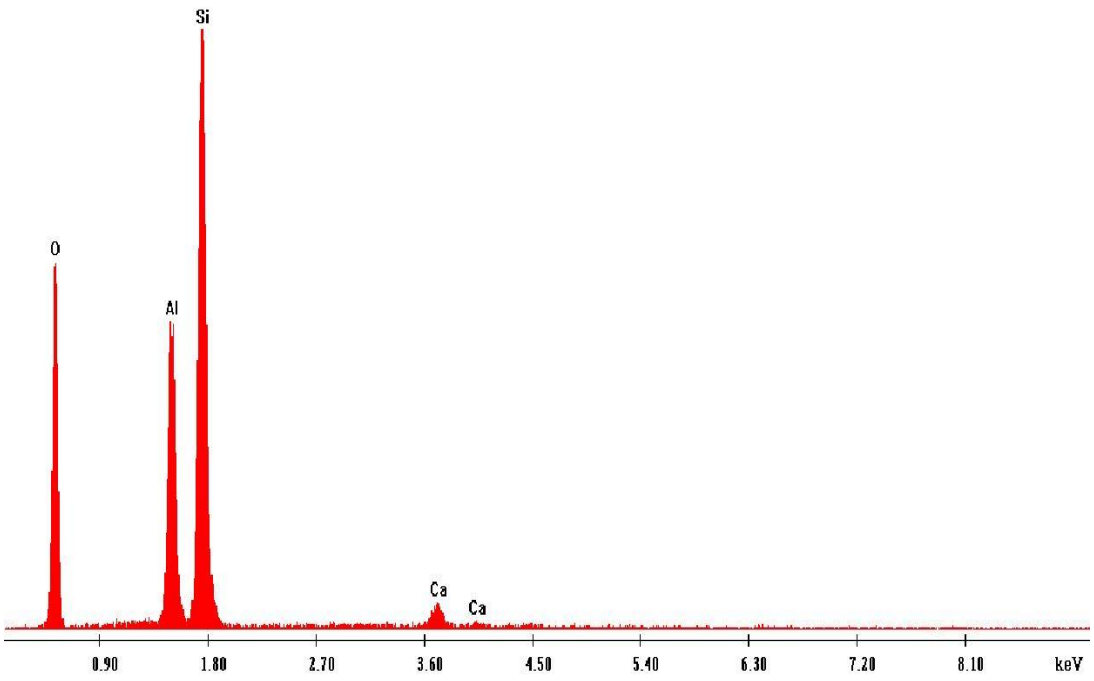

(a)

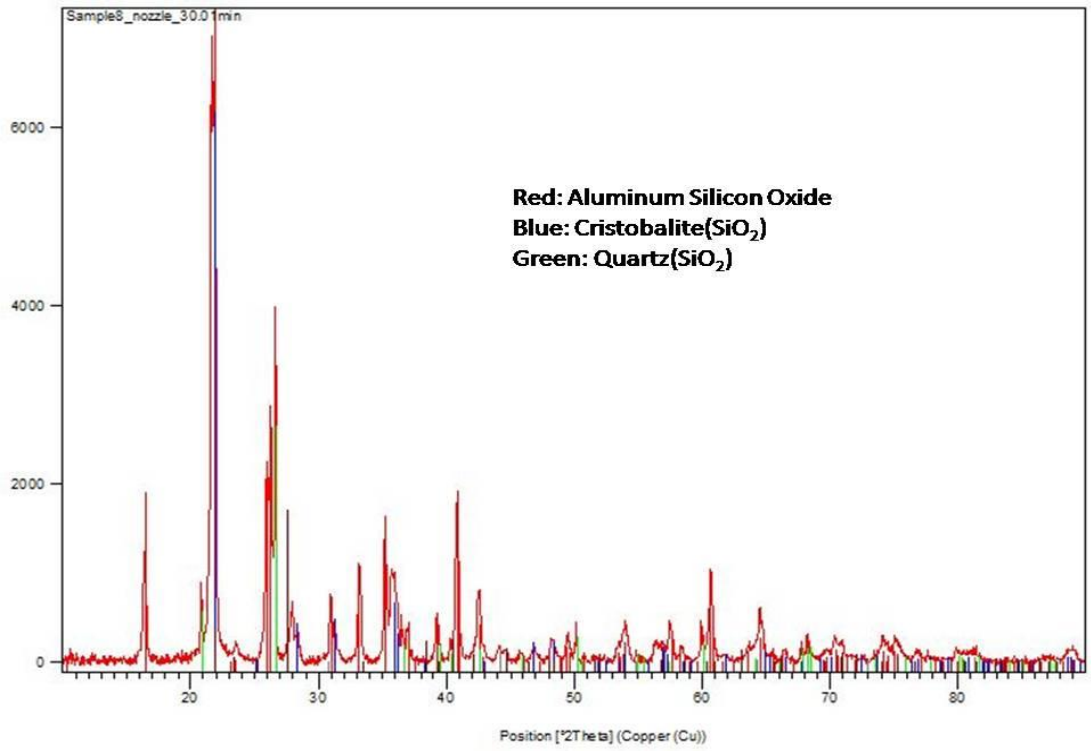

(b)

Figure 56. Results from the Nozzle sample. (a) Spectrum from EDS. (b) Diffraction pattern from x-rays.

Samples from all the locations shown above showed dominant peaks of Al, Si and O in their EDS spectra, and these peaks were consistent with XRD findings of silica, alumina, and alumino-silicates as seen in the XRD patterns.

Results from the swirl and the pilot wall samples are shown in Figures 57 and 58, respectively. They reveal a dominant peak of carbon and a smaller peak of oxygen in the EDS. This can be expected as the swirl portion of the turbine is used for initial combustion of fuel and is the central part of the swirl, so the black fragments that made the majority of this sample could be a collection of fuel residue accumulated over time. The XRD results showed a broad peak, at a value of 2θ consistent with graphite, with the broadening perhaps from small particles. The lack of more peaks in the XRD spectra made identification with XRD difficult, but the EDS results are fairly conclusive that these debris samples were essentially carbon, most likely residue from fossil fuel combustion. Samples from "volute out" and "volute in" sections were the only ones to show metal peaks in their EDS spectra that were consistent with the expected metallic alloys of the system, although the debris composition was still dominated by Al, Si and O.

An interesting aspect of the EDS spectra from the "volute out" and "volute in" samples is that Cr, Fe and Ti peaks were much taller than Ni peaks. This suggests that Ni-based superalloys in the path of the abrasive particles are not being eroded as much as the iron and titanium based alloys present along the same path. An additional possibility is that the erosion is affecting mostly the protective chromium oxide layer in the stainless steels and Ni-based superalloys. This would explain why the Cr peak is taller than the Fe peak in the EDS spectra for these samples. The EDS spectrum for the "volute in" and "volute out" sample are shown in Figure 59 and 61. The XRD

peaks for samples from the "volute out" and "volute in" sections also showed peaks of silica and alumino-silicates as shown in Figures60 and 62.

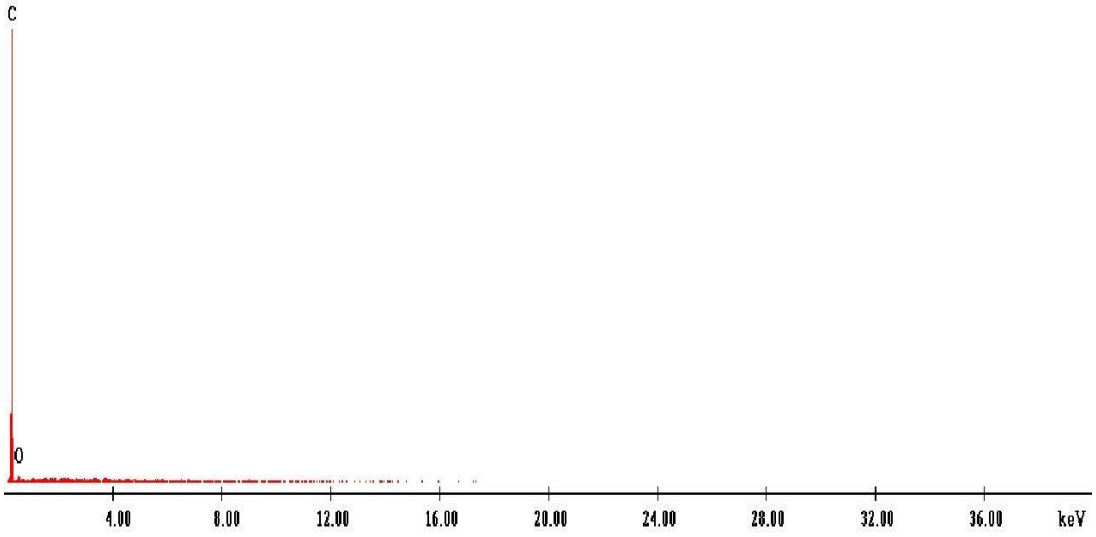

(a)

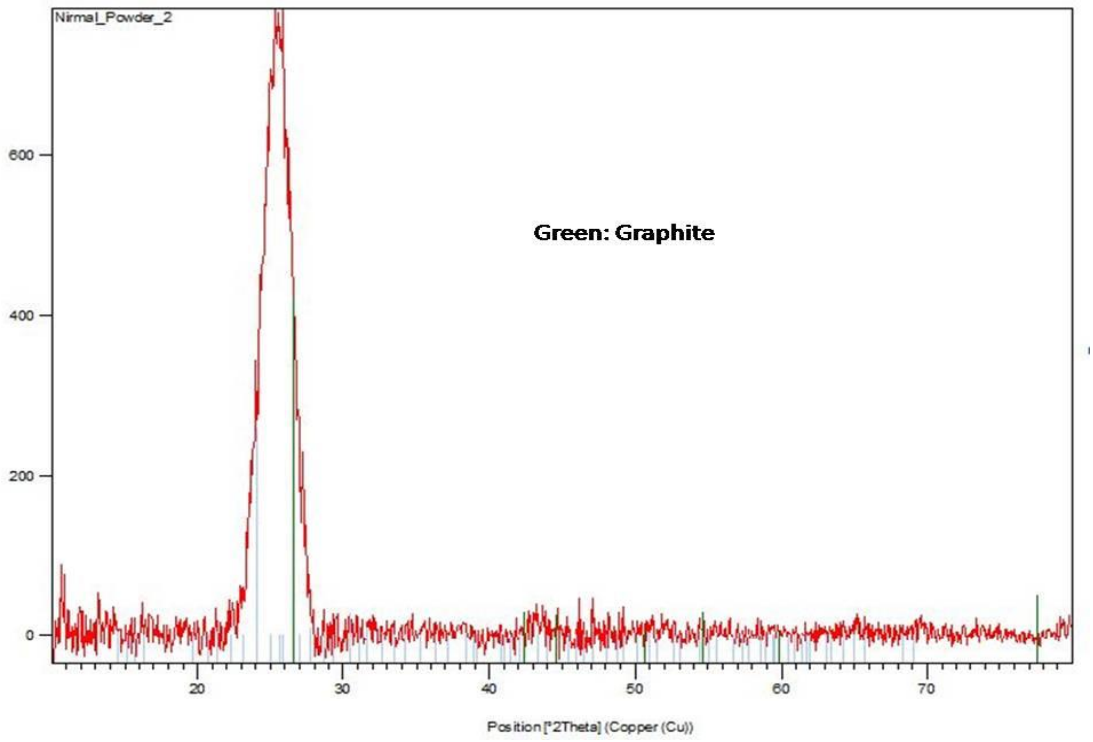

(b)

Figure 57. Results from the swirl sample. (a) Spectrum from EDS. (b) Diffraction pattern from x-rays.

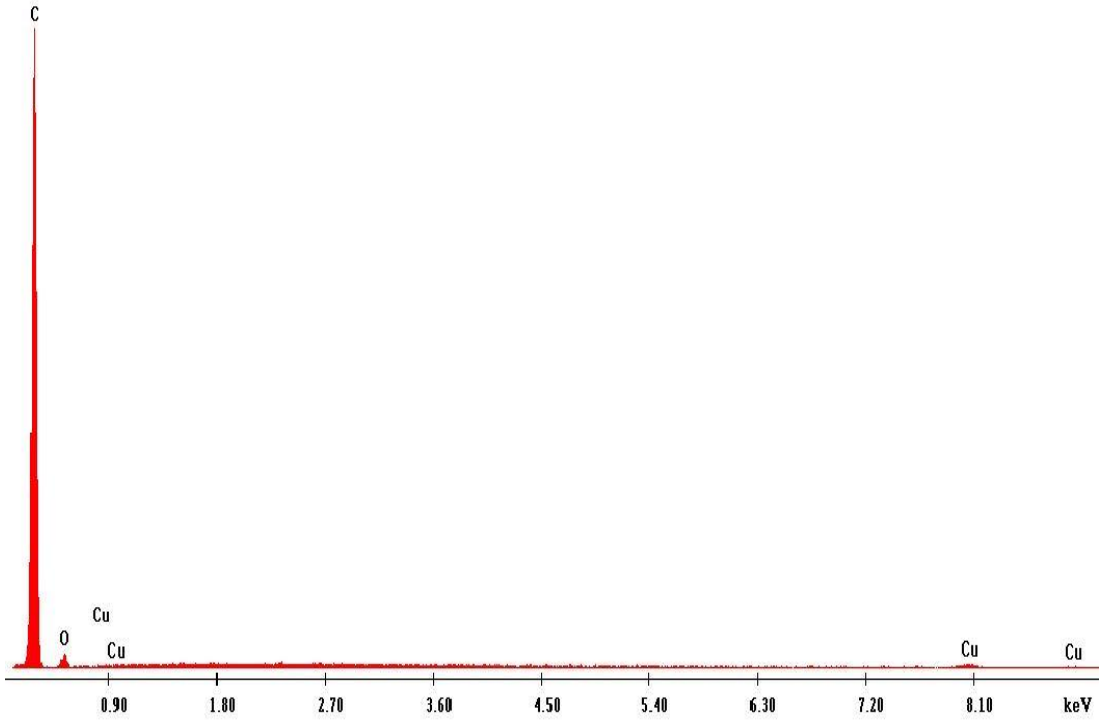

(a)

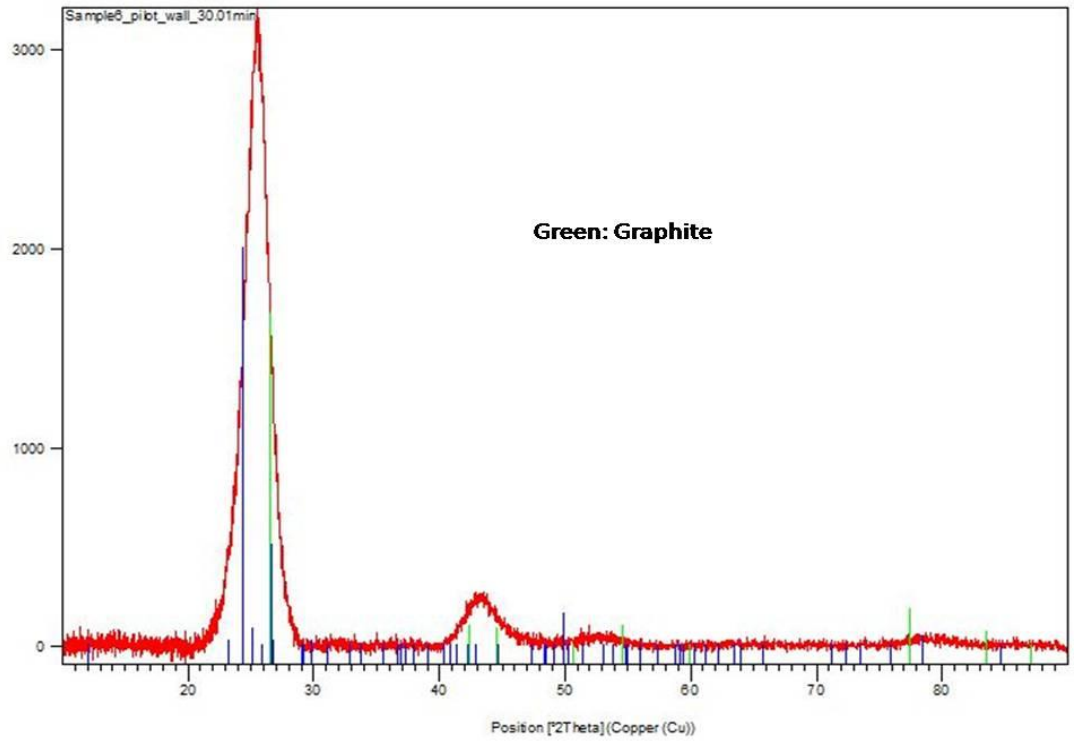

(b)

Figure 58.Results from the Pilot wall sample. (a) Spectrum from EDS. (b) Diffraction pattern from x-rays.

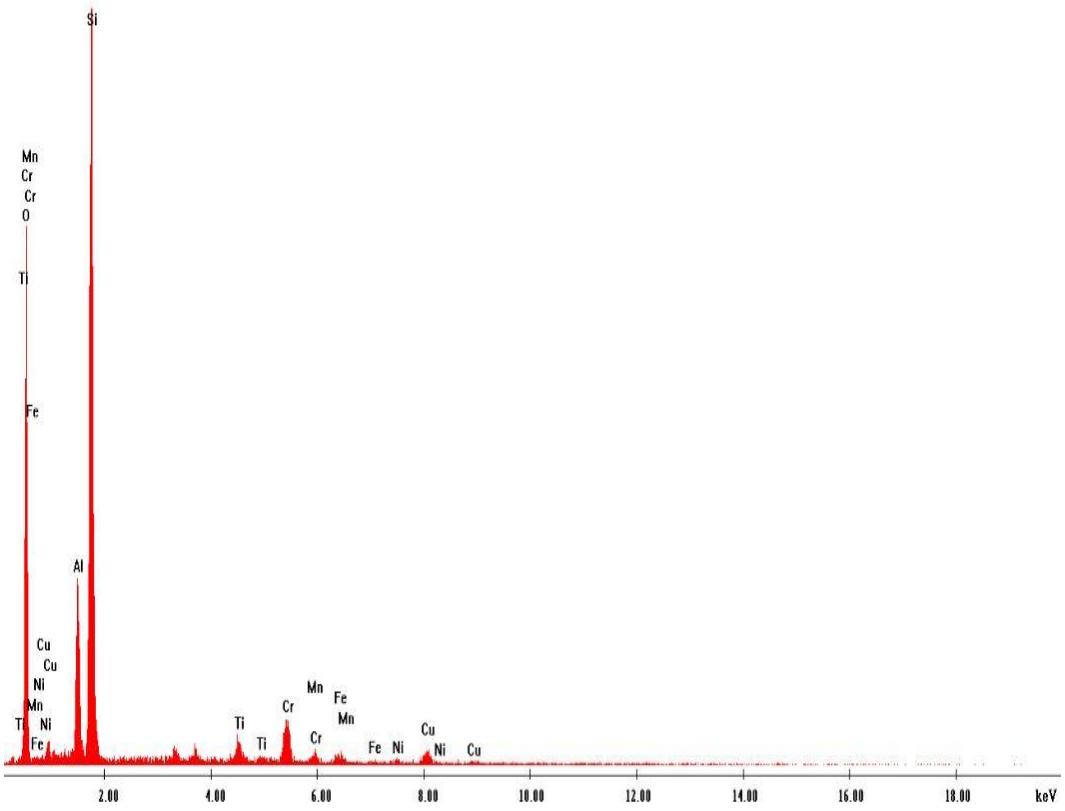

Figure 59. Spectrum from EDS data obtained using the "volute in" sample.

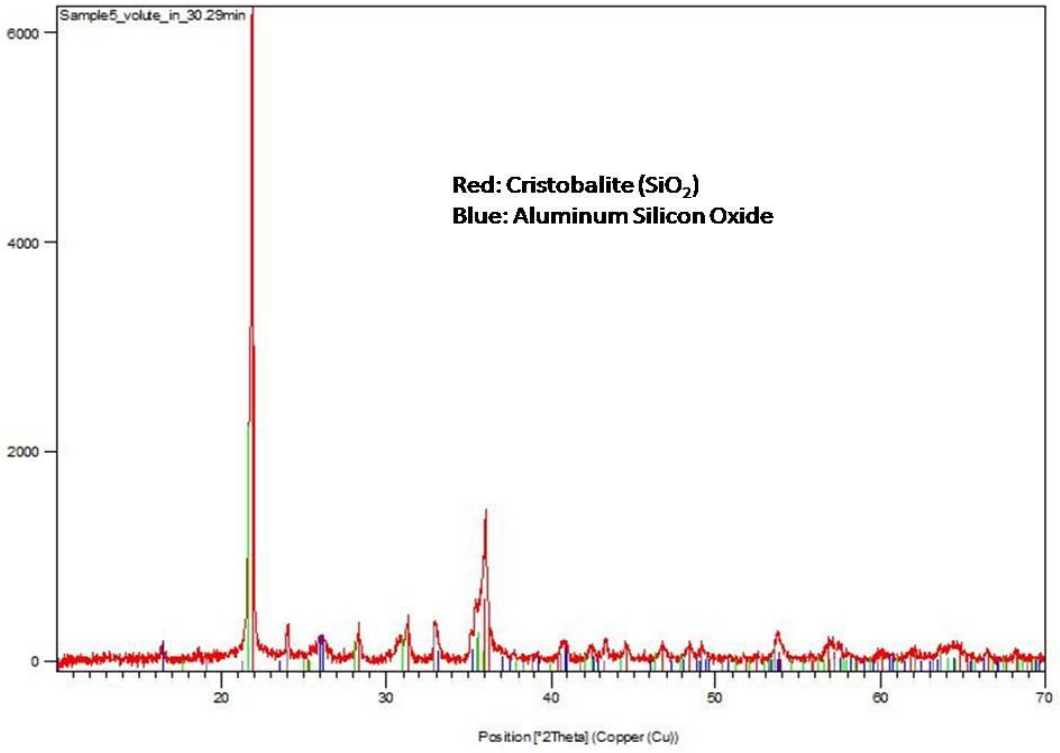

Figure 60. Results from the Volute in. sample-diffraction pattern from x-rays.

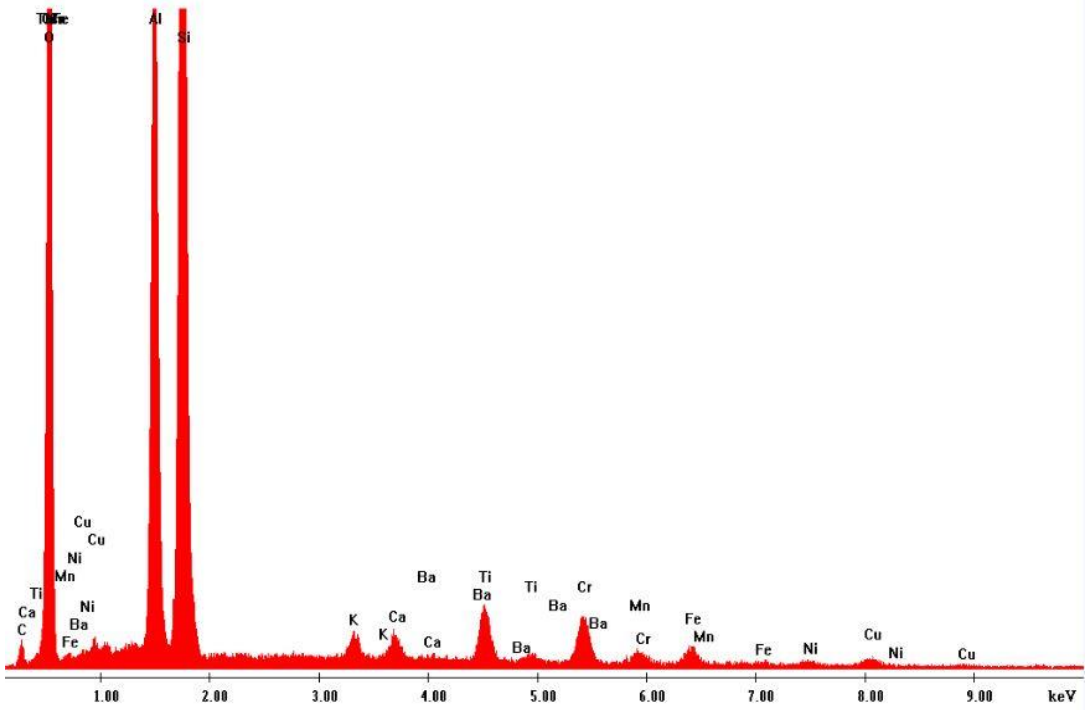

Figure 61. Spectrum from EDS data obtained using the "volute out" sample.

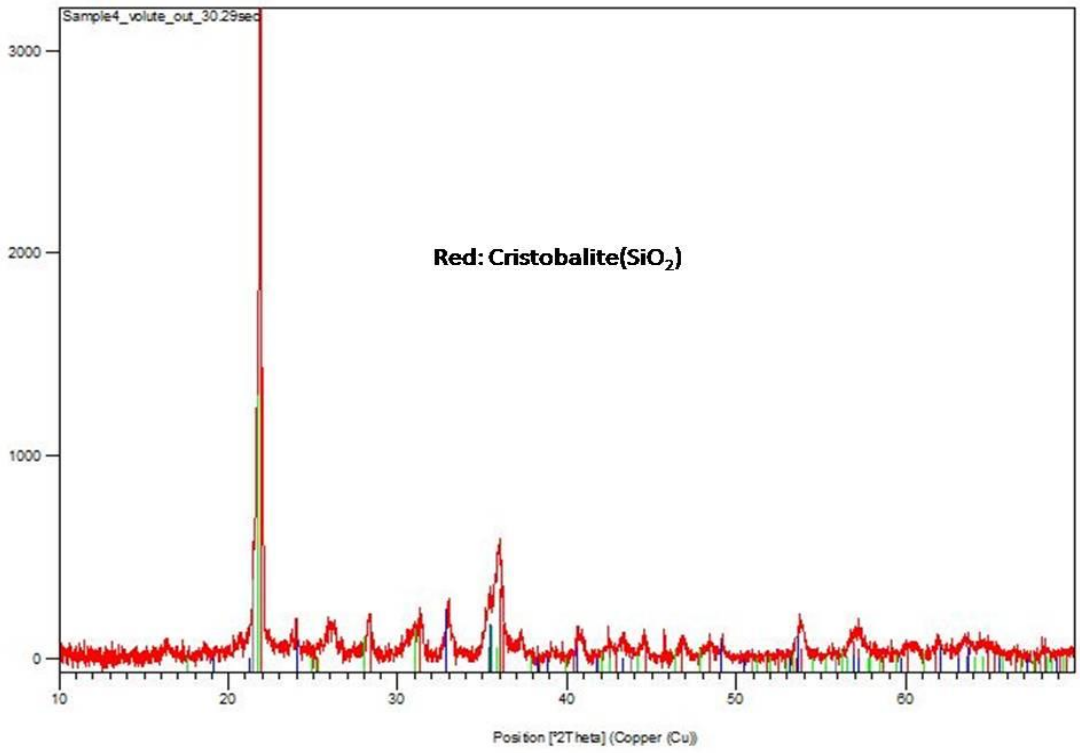

Figure 62.Diffraction pattern from x-rays from the "volute out" sample.

The most common phases found through the combined XRD and EDS results were Cristobalite (SiO_2), Aluminum-Silicon-Oxide, and Corundum (aluminum oxide). These 3 ceramic phases retain compressive strength at high temperature[95]and the fact that metal alloys will soften at high temperature[38]strongly suggests that the striking of hard ceramic particles would enhance the degradation of mechanical properties of metallic materials used in AORA's system.

The origin of the particles found in these debris samples is suspected to be from a section of the AORA system called the “receiver”, where concentrated solar radiation enters the system to heat the working fluid, air in this case, by going through a silicon oxide window and heating an array of ceramic (alumina) pins. The windows, pins and insulation are made of ceramic materials similar to those identified through the XRD measurements.

Inspection of the system in the field showed significant damage in metallic components, but the ablation alone might not be the responsible factor as the low amount of Ni found in the debris via EDS suggests that the Ni-based superalloys are not being ablated enough to explain the damage observed, so that they might be failing due to other mechanisms, e.g., fatigue enhanced by foreign object damage. Figure 63 shows some examples of debris characterized using SEM.

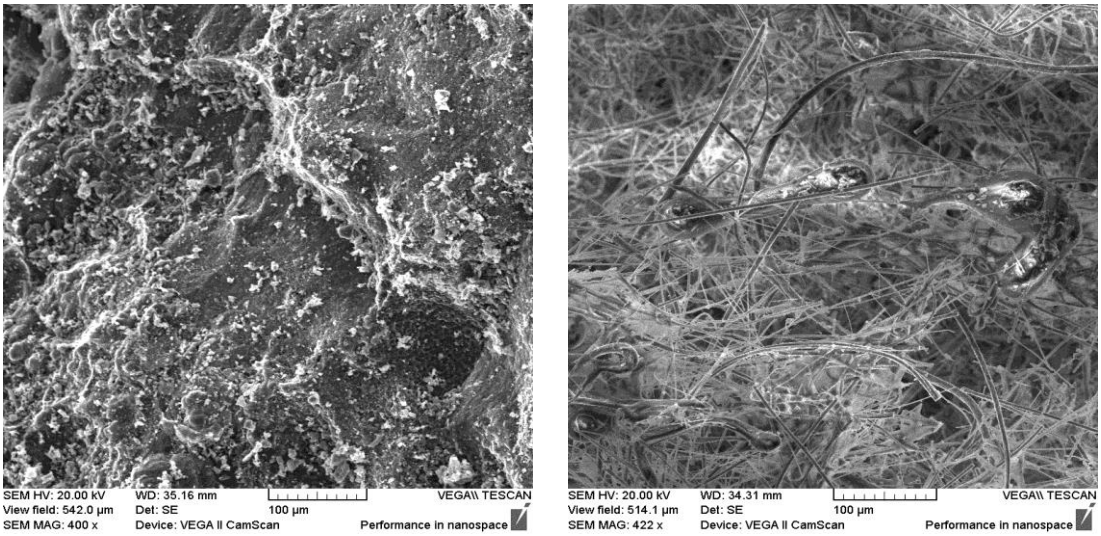

Figure 63. SEM image a) Swirl sample b) Distributor sample.

The XRD and EDS results discussed indicated that for performing lab scale FOD testing, ceramic particles made of alumina would be an appropriate substitute to resemble debris collected by AORA. Moreover ASTM standards that are widely used to test for ablation of materials produced by a stream of particles [87]also suggest to use 50 µm alumina particles to perform lab-scale erosion tests, so it was decided to use alumina particles with these characteristics to simulate FOD since it is also close to the size range, i.e.,~ 20 to 30 µm, of debris particles.

Once debris samples were characterized, the hardness of the metallic materials chosen for this study was studied, as described next.

5.3.Hardness tests

Samples of Hastelloy X and SS 347 were heat treated at 1050 °C in air for 8 hours since in AORA's system these materials will experience high temperature while in solar mode operation during the day for about 8 hours. Vickers hardness was then compared with the hardness of as-received materials measured at room temperature to the corresponding value, using 500 grs and 50 grs loads. These two load levels were

selected to explore variability in properties within the material: at 500 grs the indentation size would be large enough to probe multiple grains and show average behavior of small and large grains, while at 50 grs load the indentation size would be smaller and it can probe behavior of a single grain or a cluster of small grains. Figures 64a and 65a show the room temperature in as received condition, while Figure 64b and 65b show the hardness at room temperature after performing heat treatment at 1050 ° C for Hastelloy X and SS 347, respectively.

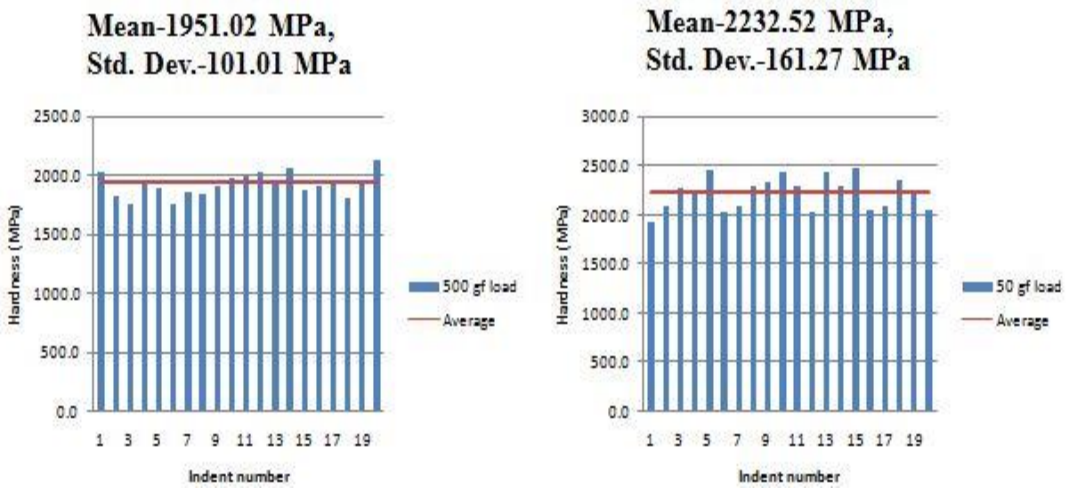

(a)

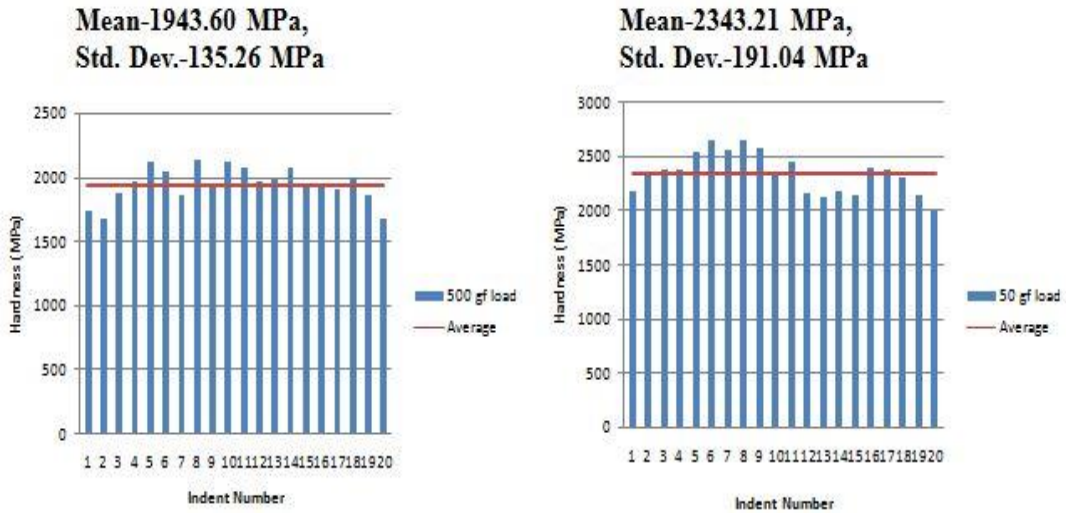

(b)

Figure 64. Hardness results for Hastelloy X a) room temperature measurements in the as-received condition b) room temperature measurements after heat treatment at 1050 °C.

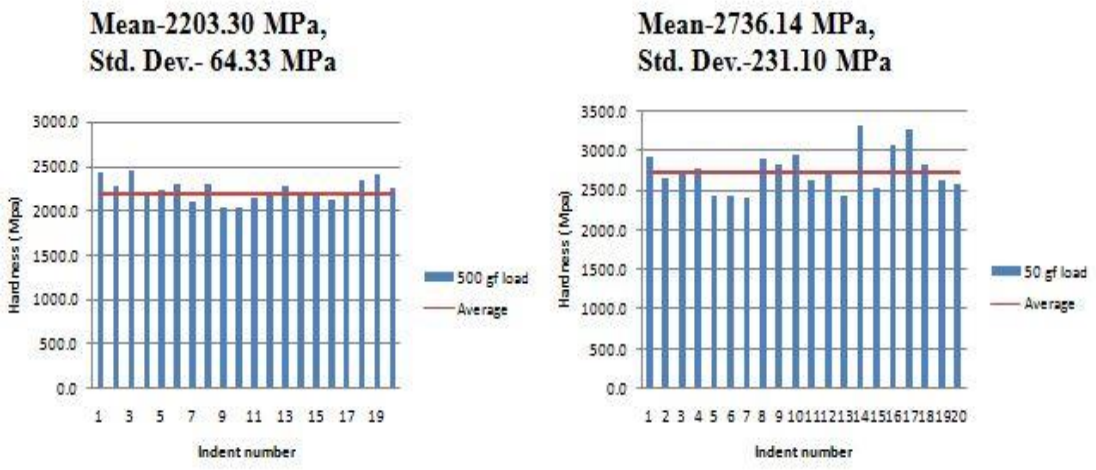

(a)

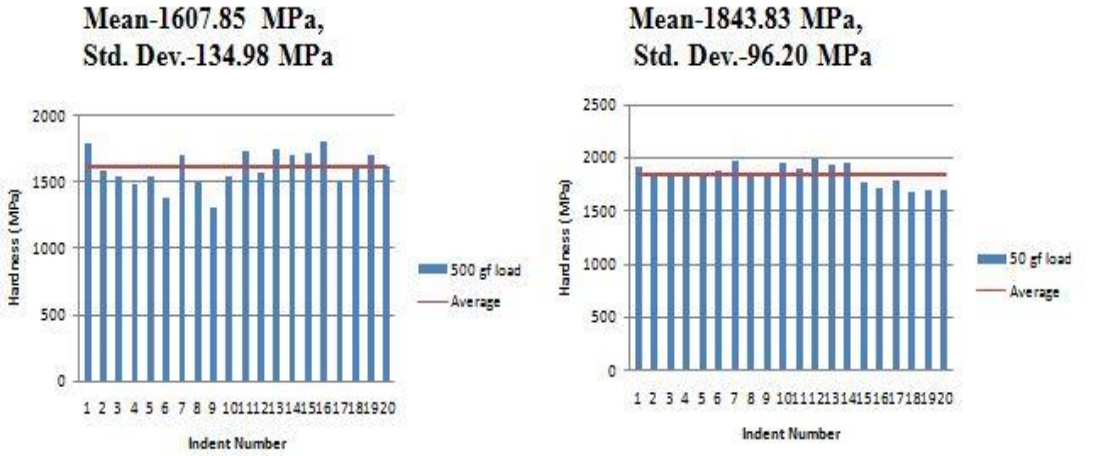

(b)

Figure 65.Hardness results for SS 347 a) room temperature measurements in the as-received condition b) room temperature measurements after heat treatment at 1050 °C.

The hardness of Hastelloy X did not reduce significantly after heat treatment at 500 grs, but increased by ~5% at 50 grs. This suggest that Hastelloy X retains its hardness after a short exposure to high temperature and increase in hardness at 50grs could be due to evolution of carbides probed by small load level. From Figure 64 it can be seen that the standard deviation is higher at 50 grs than at 500 grs, which suggests that there is more variability in properties at the microstructural scale than at the bulk.

Moreover, the heat treatment caused an increase in the variability. It can be seen from figure 65 that the hardness for SS 347 decreased significantly, by 27% at 500 grams and 30% at 50 grams, both of which are larger than the measured scatter of 3% at 500 grams and 8.5% at 50 grams. The standard deviation for SS 347 at room temperature also suggests that there is much higher variability in properties at the microstructural scale (50 grs) compared to 500 grs. Furthermore, the variability increased at high temperature for 500 grs; however, it decreased for 50 grs.

The reduction in the hardness for SS347 could be related to a reduction in number of dislocations due annealing effect, due to carbide coarsening at grain boundaries, and also because of the heat treatment grains would tend to grow, as result a yield strength and consequently hardness also reduces. This can be explained by Hall-Petch relation, which states that yield strength of material is inversely proportional to the grain size. The Hall-Petch relation is given by[96]:

$$\sigma_y = \sigma_o + kd^{-1/2} \quad (10)$$

where σ_y is yield strength, σ_o and k are material constants and d is the average grain diameter.

Instrumented spherical indentation testing was performed under inert atmosphere for Hastelloy X and SS 347 at 1 kg maximum load and at temperatures of 550 °C, 700 °C and 900 °C. Results, in the form of load-penetration curves, are shown in Figures 66 and 67.

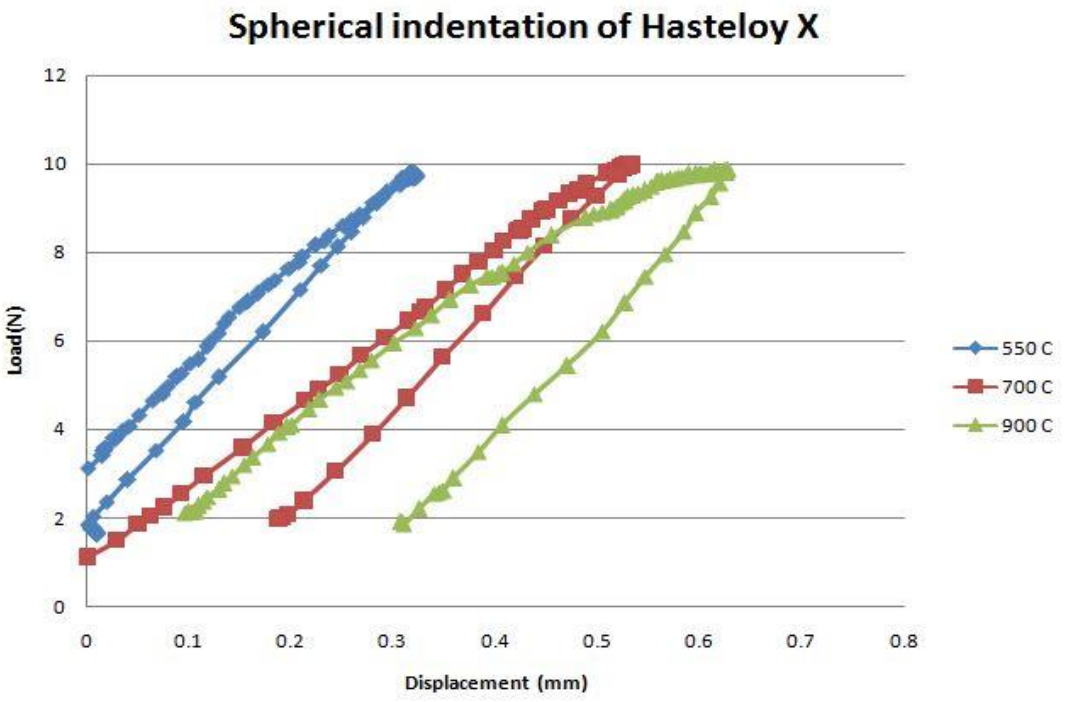

Figure 66.Hastelloy X load (N) vs. displacement (mm) curves at three different temperatures.

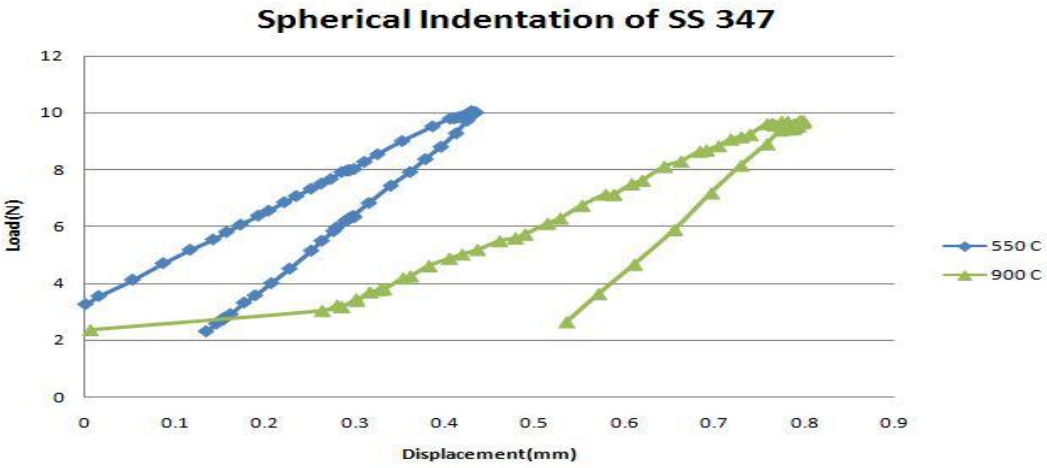

Figure 67. SS 347 load (N) vs. displacement (mm) curves at three different temperatures.

Figures 66 and 67 indicate significant increases in plastic behavior (width of the curve) occurred from 550 °C to 900 °C in all alloys, although the response of SS 347 did not change with temperature as much as expected.

These results also indicate that the mechanical properties of these materials experience meaningful reductions as temperature increases. Similar behavior can happen in AORA's turbine components when particles strike at high velocity and the high temperatures can lead to more plastic deformation than at low temperatures. These changes can be compounded by environmental effects due to oxidizing atmospheres. Erosion caused by alumina particles using a gas gun is discussed.

5.4 Erosion behavior of a ductile material

An abrasion experiment was carried out on an Inconel 625 dogbone specimen to observe the effect the particle stream had on a ductile metal’s surface. Similar effects are expected on the surface of Hastelloy X and SS 347. A pressure of 120 psi (0.82 MPa) was used in the gas gun cylinder and abrasive particles made of Aluminum Oxide with a size of 240 grit (50 µm), as specified by the ASTM standard[87], were used to impact the Inconel 625 dogbone’s gauge length. One sample was oriented normal to the particle stream (90° incidence angle) and another at 23° from the stream, it is reported in the literature that maximum erosion in ductile materials occurs at angle between 20° and 25°[57].The sample dimensions were: total sample length-105 mm; gauge length-51mm, width of the reduced section-4.36 mm andthickness-6.35 mm. The appearance of the specimens for each of these two angles is shown in Figure 68.

(a)

(b)

Figure 68. Surface appearance shown in red ellipse after impact experiment a) 90° and b) 23°.

Optical profilometry was used to assess the effect of the impact of the particle stream on the gauge length of the samples. Figure 69 shows the surface of the specimen used for the 90° incidence angle before (Figure 69a) and after (Figure 69b) the experiment at the macroscopic level, since the line profile obtained spanned a distance of 2.5 mm. The surface before the experiment is macroscopically smooth with little variation in topography. The results after the experiment shown in Figure 69b indicate the formation of a crater, where the difference between the top and lowest point on the surface was 80 micrometers. This is a significant rate of abrasion,

given that the stream of particles was only sustained for a few seconds, at most, during the experiment. This is meant to simulate the burst of foreign particles that are suspected of producing the damage observed in AORA system components as characterized in the field.

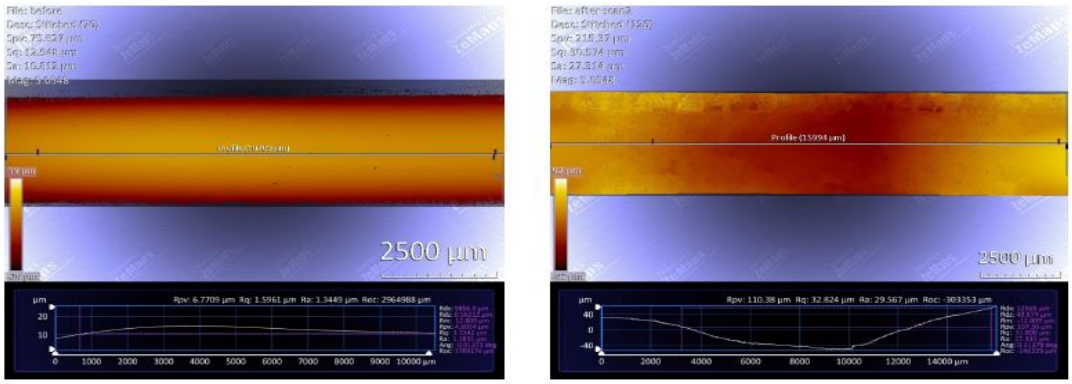

(a) (b)

Figure 69. Macroscopic profilometry analysis for the sample impacted at 90°. a) Before and b) after the test.

Samples were also examined at the microscopic level using profilometry, as the line profile measured spanned a distance of 0.05 mm. It was found that the difference between low and high points in the surface profiles was only 3 micrometers, as shown in Figure 70.

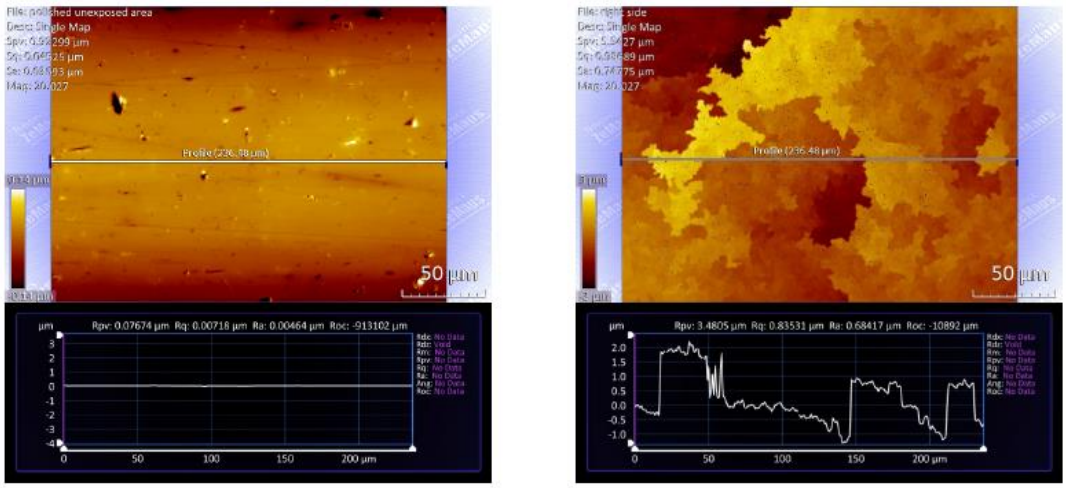

(a) (b)

Figure 70. Microscopic profilometry analysis for the sample impacted at 90°. a) Before and b) after the test.

This result indicates that, despite the short duration of the particle abrasion experiment, the material removal was fairly uniform over the area affected, most likely due to multiple impacts over the same area that overlapped with neighboring impacts, leading to macroscopic material removal, with low levels of surface roughness at the microscopic level. The same experiment was performed at a 23° impact angle and the results from the corresponding profilometry analysis are shown in Figures 71 and 72.

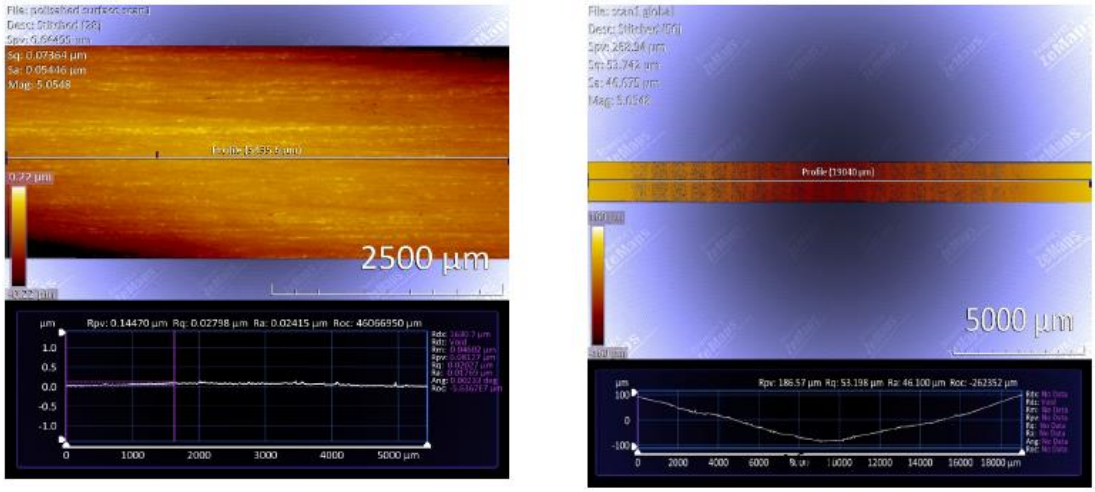

(a) (b)

Figure 71. Macroscopic profilometery analysis for the sample impacted at 23°. a) Before and b) after the test.

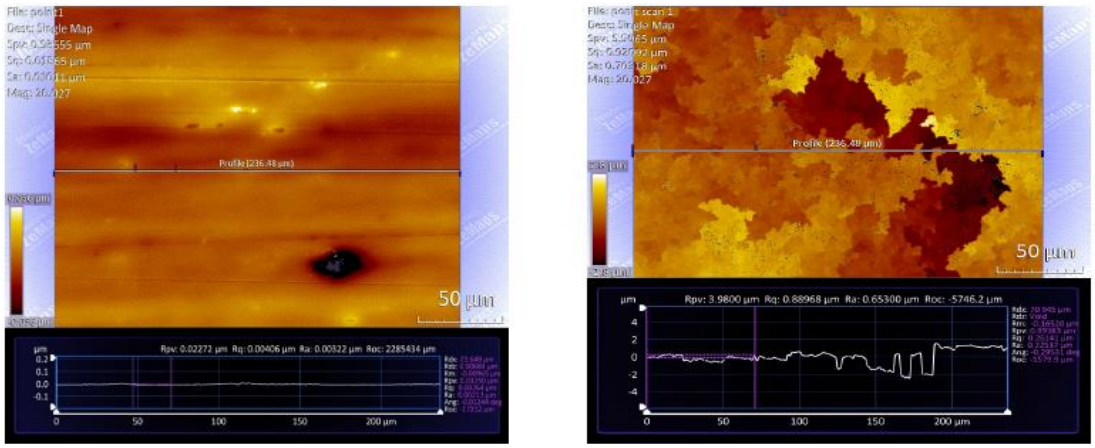

(a) (b)

Figure 72. Microscopic profilometery analysis for the sample impacted at 23°. a) Before and b) after the test.

As mentioned above, there is more erosion at angles near 23° in ductile materials[57], which agrees with experimental results shown here. Figure 71 shows the before and after surface profile at the macroscopic level for the experiment at 23°, and there is a clear difference in the erosion level when compared to the results at 90°. Note that the difference between top and bottom points of the surface was 200 µm, as compared to 80 µm at 90°. The impact angle did not make much of a difference at the microscopic level (Figure 72) but the erosion rate is certainly much higher at 23°, which is, again, fully consistent with the literature[57]. The erosion experiment on Hastelloy X and SS 347 samples were performed using 140 psi (0.965 MPa), 5 grs alumina, and at a 23° angle. The samples were then heat treated after ablation or heat treated before and after ablation. It is believed that similar or higher erosion behavior as Inconel 625 would occur on Hastelloy X and SS 347, as they are both ductile materials. So, the optical profilometry was not performed on ablated Hastelloy X and SS 347 instead the depth of the ablated area was measured using a dial indicator attached to end mill as described in the experimental section. The dial was passed through the ablated area after setting the sample horizontal and the deepest point measured was 30 µm for all the samples. Given that heat treatments were carried out either after the ablation, or before and after ablation, the added an oxide layer might have led to a reduction of the depth. The strength of the material also makes a difference on the erosion rate, it is reported that for pure metals an increase in hardness there is an increase in the resistance to erosion, but for alloys like steel there is no significant effect of the hardness on resistance to erosion[97].

An abrasion experiment at ~120 psi (0.82 MPa) with 50 µm alumina particles followed by heat treatment at 1050 °C for 8 hours was carried out on Hastelloy X and SS 347 to see the effect of it on their hardness, as these materials will experience high

temperatures and striking of foreign objects simultaneously in AORA's system. Vickers hardness at room temperature was measured with 500 grs load and results are shown in Figure 73.

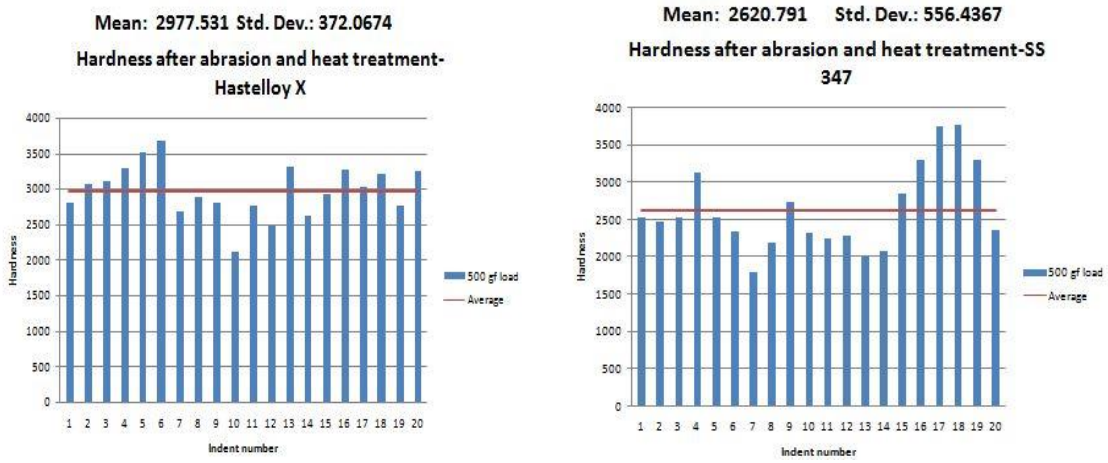

(a) (b)

Figure 73. Hardness measure at room temperature after abrasion and heat treatment a) Hastelloy X b) SS 347.

The hardness is higher than the room temperature hardness of as-received materials and also the hardness after heat treatment at 1050°C, which is likely a result of work hardening on the surface due to repeated impact of particles. The results also suggests that the FOD ablation experiment is causing deformation on the surface similar to that due to shot peening effects as described in section 2.6 of the introduction chapter. The increase in hardness is a sign that the ablation might introduce changes in local residual stress fields, which, in turn, can have a significant affect on the fatigue life. Moreover, considering AORA's condition of simultaneous interaction of repeated FOD and high temperature, the longer exposure time to high temperatures would lessen the effect of work hardening caused by FOD, but the amount and rate of material removed due to FOD could increase. Mechanical properties of the materials of interest had to be measured under the different conditions used here to shed some more light on the expected behavior. This is discussed next.

5.5 Tensile test

Room temperature tensile tests on the as-received, after heat treatment and high temperature (600 °C) tensile tests after heat treatment were performed. The heat treatment was performed at 1000 °C and 950 °C for Hastelloy X and SS 347, respectively, for 8 hours, these are the temperatures that these materials are likely to experience in AORA's turbine. Results are shown in Figures74 and 75 for Hastelloy X and SS 347, respectively. The resulting tensile properties are shown in Table 2.

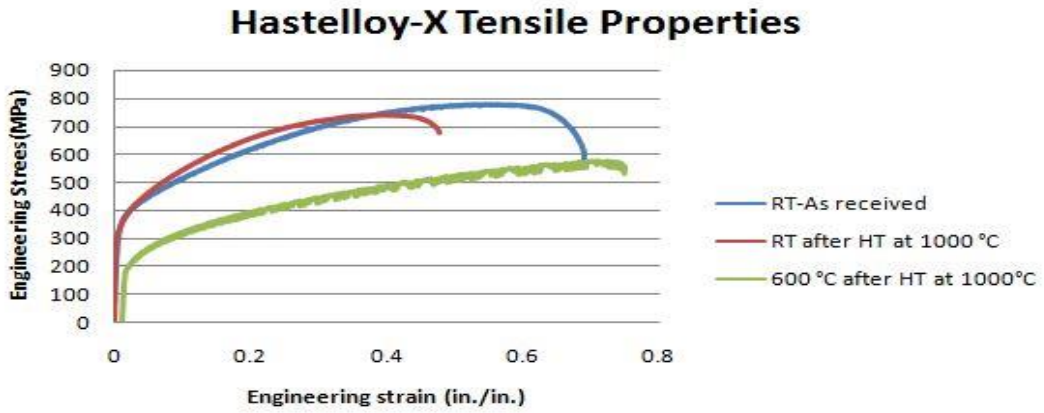

Figure 74. Hastelloy-X stress vs. strain at room temperature for as-received, after heat treatment at 1000 °C and high temperature after heat treatment at 1000 °C.

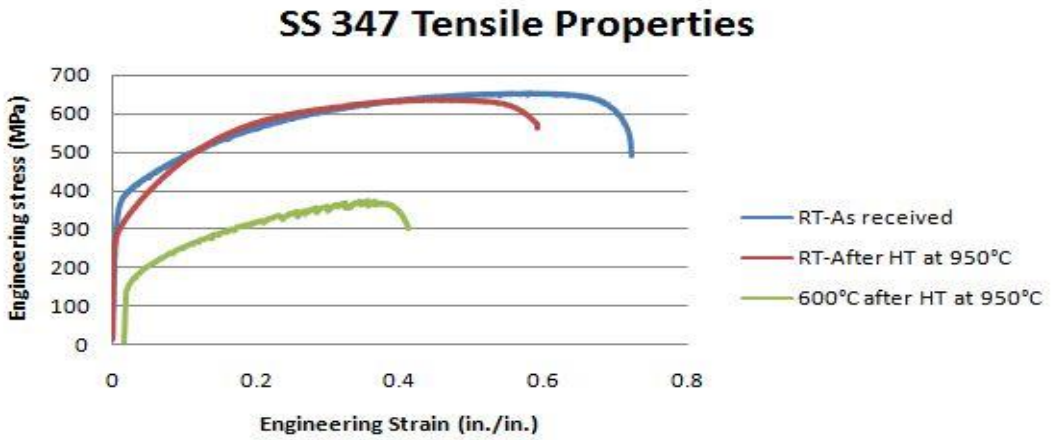

Figure 75.SS 347 stress vs. strain at room temperature for as-received, after heat treatment at 1000 °C and high temperature after heat treatment at 1000 °C.

Table 2.Tensile Properties for Hastelloy X and SS 347.

		Hastelloy-X	SS 347
Room temperature-As received (RT-AR)	Yield Strength	330	357
	Tensile Strength	775	652
	% area reduction	58	56
	% Elongation	64	71
Room temperature- After Heat treatment (RT-HTMT)	Yield Strength	300	255
	Tensile Strength	740	630
	% area reduction	42	68
	% Elongation	50	70
600°C- After Heat treatment (HT-HTMT)	Yield Strength	190	150
	Tensile Strength	575	370
	% area reduction	37.5	44
	% Elongation	37.5	31

For Hastelloy X there was a 58%, 42% and 37.5 % reduction in area at RT-AR, RT-HTMT and HT-HTMT respectively, while elongation was 64%, 50% and 37.5 % at RT-AR, RT-HTMT and HT-HTMT, respectively. For SS 347 there was a 56%, 68% and 44 % reduction in area at RT-AR, RT-HTMT and HT-HTMT, respectively, while elongation was 71%, 70% and 31% at RT-AR, RT-HTMT and HT-HTMT, respectively. Moreover, comparing the tensile properties of each material at different conditions with RT-AR, there is a reduction of 9% in yield strength and 4% in UTS for RT-HTMT, 42% in yield strength and 25% in UTS at HT-HTMT for Hastelloy X. Tensile tests done at room temperature after heat treatment shows very minor

reduction in tensile properties; however, literature reports decrease of 38% in UTS and 25% in yield strength at 600 °C [98].

The yield strength reduction at 600 °C is the same as seen in literature while the UTS reduction was slightly higher. For SS 347, a reduction of 29% in yield strength and 3% in UTS at RT-HTMT while there was reduction of 58% in yield strength and 43% in UTS at HT-HTMT. There was a significant reduction in yield strength for RT-HTMT when compared to RT-AR but reduction in tensile strength was very minor. The product data sheet from Allegheny Technologies Incorporate (ATI), shows 36% and 43% reduction in yield strength and UTS, respectively, at 649 °C when compared to room temperature. In the current study a higher reduction of 58% in yield strength compared ATI's product data while the reduction in UTS of 43% was observed, which is similar for SS 347 tensile properties as compared to ATI's product data shown in Table 3. The higher reduction in yield strength could be due to heat treatment performed on the sample prior to testing at 600 °C, which could also be the case for higher reduction seen in UTS for Hastelloy X when compared data in literature.

Table 3. Typical elevated tensile properties for ATI 347[99].

Test temperature (°C)	Yield strength (MPa)	Ultimate tensile strength (MPa)	% Elongation
20	250	640	45
204	250	505	36
427	205	475	30
538	190	435	27
649	160	360	26

The tensile results under different conditions indicate that for Hastelloy X and SS 347 there is loss in mechanical properties after exposure to the high temperature by heat treatment and also tensile tests performed at high temperature. High temperature tensile tests show serrated stress-strain curves, likely due to Portevin-Le Chatelier (PLC) effect in the non-linear region. This type of behavior has been reported for Hastelloy X at temperatures between 200 °C to 650 °C [100], but there is lack of high temperature study for PLC effect on SS 347. This effect occurs due to dynamic strain aging (DSA) as a result of interaction between dislocations and solute atoms during plastic deformation[101]. It has been reported that DSA can affect properties and ductility, it can be seen that ductility for both materials has decreased at 600°C. The serration are classified type A, B, C, D and E based on its appearance, and the serrations of Hastelloy X and SS 347 are likely to be type B and type A, respectively. Type A serrations are locking serrations characterized by an abrupt rise in stress and then drop to or below the general level of the stress strain curve. Type B serrations are characterized by small oscillations about the general level of the stress-strain curve that occur in quick succession.

The tensile strength values obtained in the high temperature test were then used to estimate the stress level to use for fatigue tests using the Basquin's equation, as mentioned in the experimental procedure chapter. The fatigue behavior observed from these tests will be discussed next.

5.6. Fatigue Life and Fractography

The matrix of test conditions and resulting fatigue lives are shown in Table 4. The fractured samples were then cut to a size of around 10 cm to perform fractography using Scanning Electron Microscopy (SEM).

Table 4 Testing condition and fatigue lives.

Material	Testing condition	Temp	Stress	Sample Tested	Cycles to failure
Hastelloy X	I) Heat treatment at 1000 °C- No ablation	600 °C	440MPa	HX-HT-NA-1	73,989
				HX-HT-NA-2	80,737
	II) Heat treatment at 1000 °C after ablation			HX-HT-A-1	190,069
				HX-HT-A-2	63,954
	III) Heat treatment at 1000 °C before and after ablation			HX-HTBA-A-1	80,641
				HX-HTBA-A-2	45,438
SS 347	I) No ablation - Heat treated at 950 °C		340MPa	SS-HT-NA-1	Run out-5 million cycles
				SS-HT-NA-2	Run out-3 million cycles
	III) Heat treatment at 950°C before and after ablation			SS-HTBA-A-1	133,501
				SS-HTBA-A-2	333,095

In the discussion below each testing condition is denoted by (I, II, III). The "no ablation" condition (I) should show the material response in the absence of FOD when exposed to high temperature to provide a baseline for comparison to other conditions. Condition (II) heat treatment after the ablation was meant to provide a closer reproduction of AORA's system condition, as metals will be exposed to high temperatures for long periods of time following FOD, which evidence suggests is intermittent in AORA's system. Condition (III) heat treatment before and after ablation mimics the actual scenario that AORA component experience when FOD and high temperature are frequent processes. Two samples were tested for each condition as shown in Table 4. Experiments for SS 347 using condition (II) were not performed since condition (III) is more likely to occur in AORA's turbine rotor and there are no SS347 components there.

A comparison of the fatigue life results for Hastelloy X from Table 4 between condition II (heat treatment after ablation), III (heat treatment before and after ablation) with I (no ablation) indicates that for condition II the fatigue life for HX-HT-A-2 is lower that for HX-HT-A-1, which could be due to statistical variability or due to effects of the heat treatment and higher fatigue life for HX-HT-A-1 could be due to shot peening effect of particles producing compressive stresses. For condition (III) sample HX-HTBA-A-2 has the lowest life among all condition suggesting an effect of FOD; however, the fatigue life for sample HX-HTBA-A-1 is similar to that seen in condition I. The average fatigue life for non-ablated Hastelloy X samples was ~77,000 and ~95,000 cycles for all the ablated samples. It can be said that ablation tends to have less effect on fatigue life or produce a mild increase in life for Hastelloy X due to possible shot peening like effect created by impacting particles.

For SS 347 the fatigue life in condition (III) heat treatment before and after ablation is substantially lower than the fatigue life for condition (I) no ablation, this reduction in fatigue life is most likely due to effects of FOD. The higher life of SS 347 under no ablation suggest that without FOD it can sustain the stress level with higher life due to absence of impact induced stress concentration, change in local geometry and microstructure. The no ablation-samples for SS347 lasted for more than 3 million cycles and did not fail even at 340 MPa. This long life might be associated with strain hardening of the material at the test temperature, which could lead to increases on yield strength and make the loading essentially elastic. Other potential effects include heterogeneity on stress and strain distributions due to variable cross-section of the sample and the presence of a thick oxide layer due to the heat treatment, leading to changes on the surface condition. Further studies would be necessary to elucidate this behavior, but they are beyond the scope of this work.

Fractography was performed on all samples taken to final failure to look for further evidence to elucidate the failure mechanisms. In that regard, some common features associated to fatigue cracking were observed on the all the fracture surfaces, such as 1) a distinct crack nucleation site with a fairly flat fracture surface, which is typical of stage 1 crack growth (shortly after nucleation) when cracks usually propagate crystallographically along a slip plane[64]. In this stage grain boundaries, inclusions and precipitates can serve as a road blocks for crack propagation[64]. 2) As crack length increases the stress intensity factor K increases as well given that the tests were carried out under load control. This leads to significant slip developing at the crack tip. This is typical of stage 2 crack growth, which is controlled by plastic blunting of the crack tip and leads to the development of beach marks that show the evolution of

the crack front as it propagates and within beach marks one can see striations, which represent crack advance per cycle and are always parallel to the crack front and perpendicular to the crack front direction[64]. 3) Finally, a distinct final fracture region showing dimples and plastic deformation could be observed, which occurs when the crack length is long enough to have the maximum stress intensity factor come close to the fracture toughness of the material, and final failure occurs by sudden crack growth and overloading. This is called stage 3[64].

Crack growth analysis from stage 2 striation and fracture surface features are discussed next for Hastelloy X and SS 347.

5.7.Crack growth analysis and fractographic examination

The characteristic features of fracture surfaces can provide information about crack growth rates as well as possible damage mechanisms. The orientation of the striations suggests the direction of crack growth and the striation spacing gives a good estimate of the crack growth rate per cycle at that particular location[102]. The striation spacing was measured by using high magnification images taken via SEM at three different location of stage 2 along with ImageJ software. The locations selected for striation analysis were: the region around the first observed beachmark, the region between the first observed beach mark and final fracture and the region near final fracture. By highlighting an area of interest a linear distance was measured in the direction of crack propagation, dividing this length by the number of striations lying in that measured area of interest length gives the average striation spacing, which is also the average crack growth rate at that location[102].

Effects of temperature on fracture appearance can be significant and can result in the change of fracture mode[103],but when the material has a tendency to exhibit phase change or precipitation at specific temperatures, it is often difficult to isolate the effects of dominant fracture mechanisms [103]. Some features observed in all the fatigue tested samples are also discussed by using examples from each testing condition.

Hastelloy X

I) No ablation

Two samples were tested for condition (I) no ablation after heat treatment at 1000 °C to establish a baseline of the fatigue behavior. The fractography images are only shown for sample HX-HT-NA-1 in Figures 76 and 79, whereas crack growth rates for samples HX-HT-NA-1 and HX-HT-NA-2 are reported. Fracture features that were common for all three Hastelloy X conditions are shown in Figure 77 and 78 by taking examples from non-ablated Hastelloy X samples.

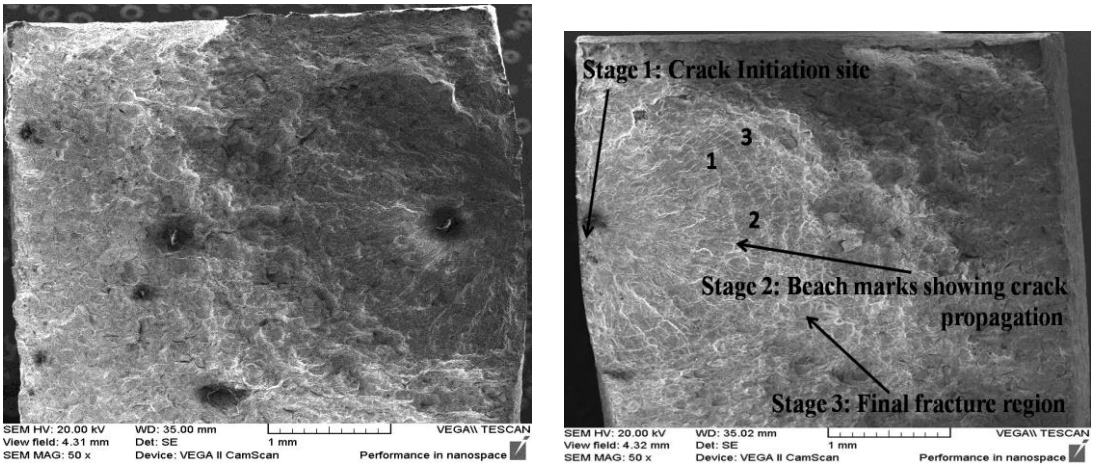

(a) (b)

Figure 76.Fracture surfaces for sample HX-HT-NA-1, condition (I)-Heat treatment at 1000 °C-No ablation. (a) General fracture surface appearance. (b) Matching fracture surface with different crack growth stages labeled.

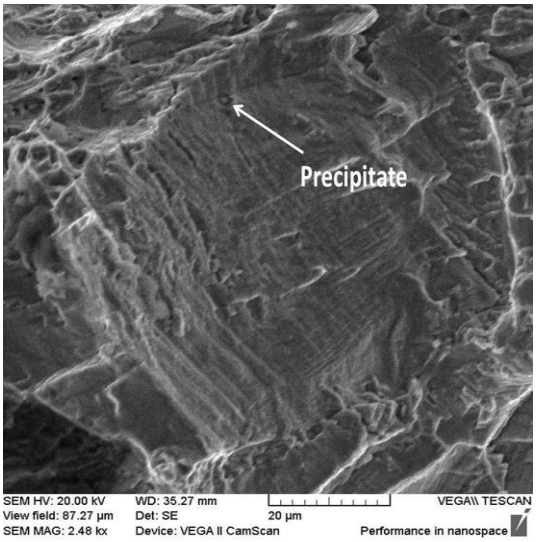

Figure 77. Feature near first beach mark for sample HX-HT-NA-2.

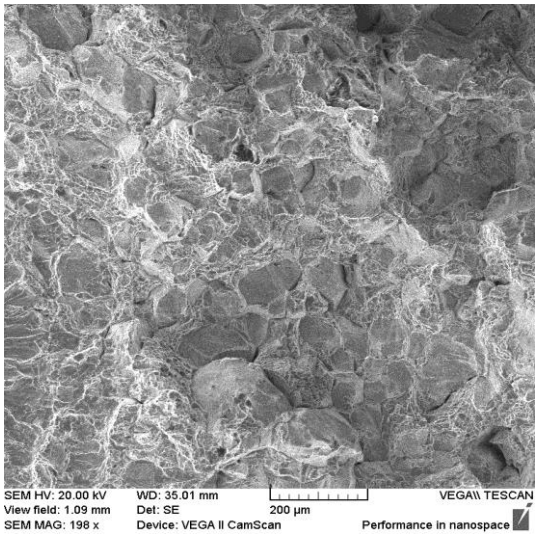

Figure 78. Feature near fracture area for sample HX-HT-NA-1

As can be seen in Figure 76b, the crack initiation site is near the edge of the specimen, which is typical of fatigue crack nucleation[64], and the region corresponding to stage 1 can be identified as being cleavage-like and the orientation of the facets reveals the direction of crack propagation. In high strength metallic alloys under high cycle fatigue most of the total life is spent in initiating a stage 1 crack[64]. Some light beach marks can also be seen as shown in Figure 76b, which appear due to crack arrest as the crack stops growing for some cycles when it encounters an obstacle. Precipitates, inclusions and discontinuities were observed in stage 2 as shown in Figure 77. These features could have emerged during the heat treatment and possibly played a role in crack propagation as can be seen that around particles the striation spacing is wider. As the crack reached near stage 3 there was some transgranular fracture revealed by grain boundary facets and grain separation, as shown in Figure 78. These could be due to creep related damage.

The area by locations 1,2 and 3 shown in Figure 76b, which is towards the end of stage 1 and marks the beginning of stage 2, is shown at high magnification in

Figure 79 and shows the typical striations that appear during stage 2. These locations were selected such that "1" represents the area around the first beach mark observed, "2" represents the area between first beach mark and final fracture region and "3" is an area between the final beach mark observed and the final fracture region.

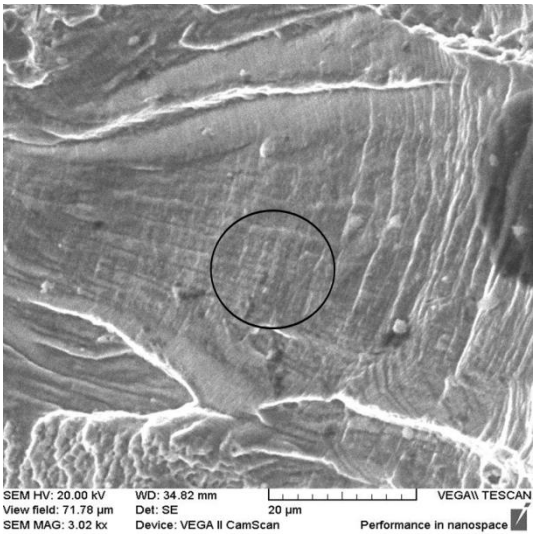

(a)

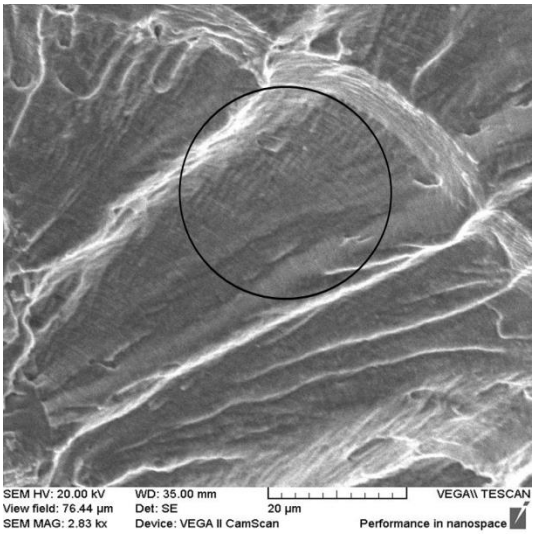

(b)

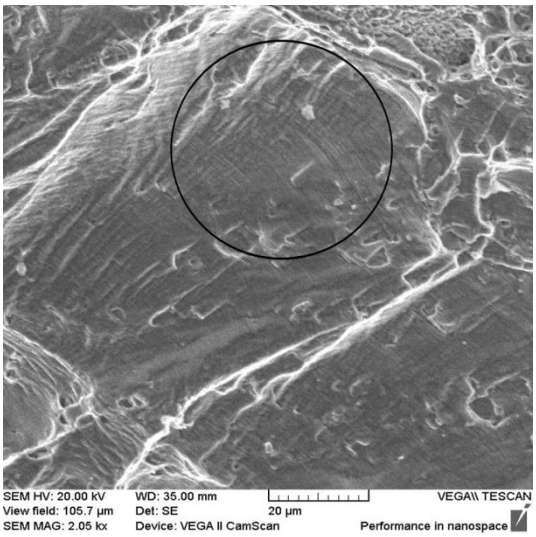

(c)

Figure 79. (a)High magnification image of location “1” in Figure 76b. (b)High magnification image of location “2” in Figure 76b, (c)High magnification image of location “3” in Figure 76b.

As mentioned earlier the orientation of the striations suggests the direction of crack growth and the striation spacing gives a good estimate of the crack growth rate per cycle at that particular location. The striation spacing enclosed by the circle shown in Figures 79a, 79b and 79c for locations 1, 2 and 3, respectively, was calculated using the method mentioned above for the two samples tested HX-HT-NA-1 and HX-HT-NA-2 with condition (I)-no ablation-heat treatment at 1000 °C and is shown in Table 5. After reaching the critical crack length the fracture surface had dimples and also coalescence of microvoids, both of which are typical features of ductile failure due to overloading (stage 3)[64].

Table 5.Crack growth rate (CGR) at different locations for Hastelloy X condition (I)-Heat treatment at 1000 °C-No ablation.

Sample	1(μm/cycle)	2(μm/cycle)	3(μm/cycle)	Final crack length (mm)	Cycles to failure
HX-HT-NA-1	0.75	0.69	0.87	2.08	73,989
HX-HT-NA-2	0.86	1.37	1.3	2.19	80,737

In Table 5 it can be seen that CGR for sample HX-HT-NA-1 was lower at location 2 compared to location 1 and increased at location3. This decrease in CGR could be due to effect of crack closure during which crack growth retardation occurs. Ideally it is expected that CGR would increase as the crack propagates so another interpretation of the decrease in CGR at location for sample HX-HT-NA-1could be due to the fact that current method for crack growth analysis gives an estimate of CGR at the specific location chosen and the microscopic CGR could be different from the overall CGR. For sample HX-HT-NA-2 the CGR increases as crack propagated from location 1 to location 2 and was nearly the same at location 3. As expected for both samples the CGR was highest at location 3; however; sample HX-HT-NA-2 had

a higher crack growth rate compared to Sample HX-HT-NA-1, although sample HX-HT-NA-2 had a higher fatigue life than sample HX-HT-NA-1. A longer period of crack nucleation and a longer final crack length for sample HX-HT-NA-2 are likely to explain the difference.

II) Heat treatment at 1000 °C after ablation

Two samples were tested for condition (II) heat treatment at 1000 °C after ablation, fractographic crack growth analysis is shown only for sample HX-HT-A-1 in Figure 80 while crack growth rates for both samples HX-HT-A-1 and HX-HT-A-2 are reported. Common fracture surface features observed between the first beach mark and the final fracture region for all the conditions are described in Figure 81 by using the results of a Hastelloy sample with heat treatment at 1000°C after ablation as an example.

Figure 80 shows the fracture surfaces of the Hastelloy-X sample, condition (II) heat treatment after ablation. It can be clearly seen that there was a river-like pattern merging at the bottom right corner shown in Figure 80a, which is indicative of the crack initiation site. The crack initiation site was on the opposite side of the ablated surface. Figure80ashowsclearly the three regions of initiation (stage 1), beach marks (stage 2) and final ductile fracture (stage 3). Figure 81 shows common features observed in Hastelloy X for all conditions. In particular, the images show secondary cracks, either trans- or intergranular, which can affect the crack propagation rate at that particular location. Figure 82 shows locations 1, 2 and 3 from Figure 80a, selected for crack growth analysis.

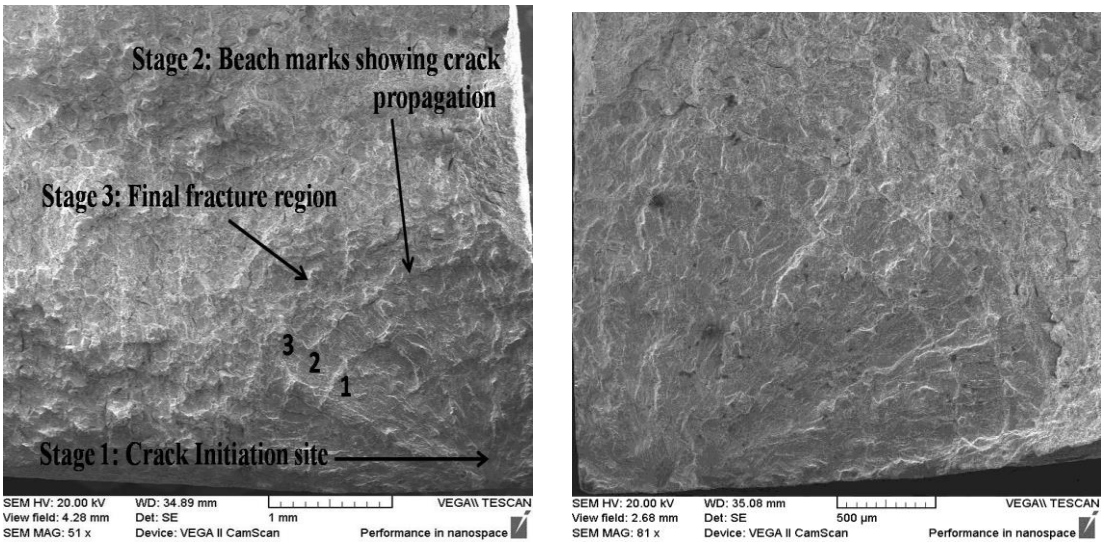

(a) (b)

Figure 80. Fracture surface for the Hastelloy X sample HX-HT-A-1, condition (II)-Heat treatment at 1000°C after ablation. (a) Different crack growth stages marked on the surface. (b) Matching fracture surface on the other side of the sample.

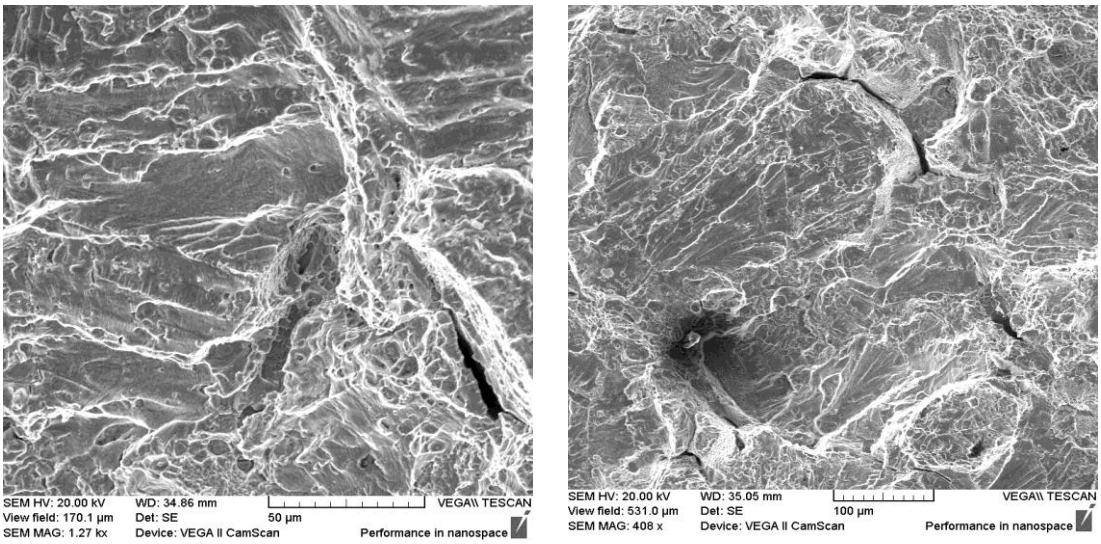

Figure 81. Sample HX-HT-A-1, heat treated after ablation, region near middle beach mark (location "2" in Figure 80a).

The beach marks shown in Figure 82 were analyzed using SEM at magnifications above 3000x to find and characterize fatigue striations at locations 1, 2 and 3

respectively. As mentioned above, striation spacing provides information on crack growth rate per cycle and results are shown in Table 6.

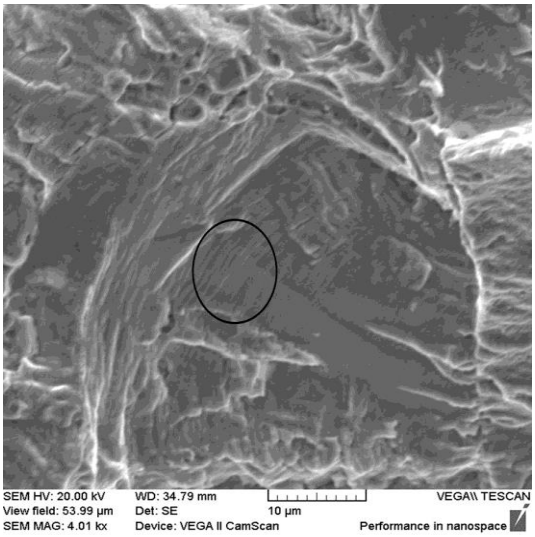

(a)

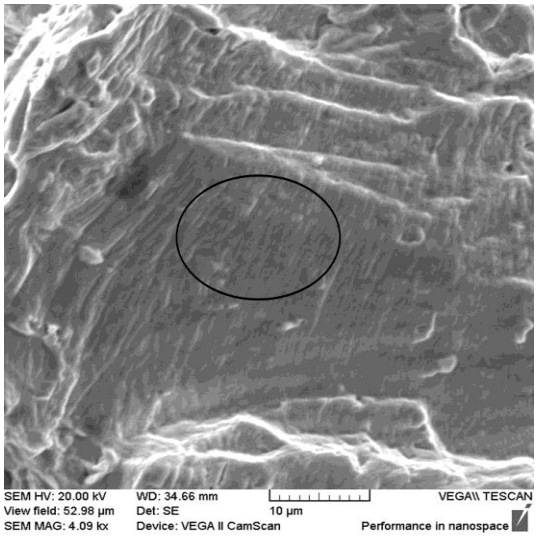

(b)

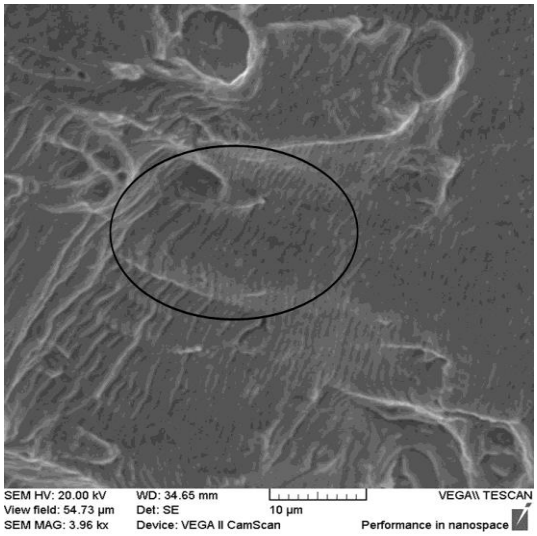

(c)

Figure 82. (a) High magnification image of location 1 in Figure 80a, (b) High magnification image of location 2 in Figure 80a, (c) High magnification image of location 3 in Figure 80a. Striations lying in the oval region were used for CGR analysis.

Table 6. Crack growth rate (CGR) at locations 1,2 and 3 for Hastelloy X, condition (II)-Heat treatment at 1000°C after ablation.

Sample	1(µm/cycle)	2(µm/cycle)	3(µm/cycle)	Final crack length (mm)	Cycles to failure
HX-HT-A-1	0.66	0.74	1.04	2.28	190,069
HX-HT-A-2	1.02	0.70	0.83	2.16	63,954

As mentioned before locations 1,2 and 3 were chosen based on the occurrence of beach marks and do not reflect the distance from the crack initiation site. It is reported in the literature that FOD can accelerate the CGR compared to samples without FOD due to effect of stress concentrations and residual stresses, but in the current FOD experiments the depth of the ablation region was shallow and consequently the residual stress field is likely to be small, which suggest that CGR at locations 1, 2 and 3 are outside the influence of FOD. The effect of FOD on fatigue life might be more on a reduction on the number of cycles needed to initiate a crack[66],due to the presence of residual stresses from the impacting particles even after heat treatment or due to governing effect of stress concentration and not FOD. Also, the crack initiation site for sample HX-HT-A-2 was away from the ablation, but on the same surface as the ablation, the ablation was likely to be responsible for reducing the number of cycles required to initiate the crack, while for sample HX-HT-A-1 the crack initiated on the opposite surface to the ablation surface, which suggests that ablation was not an effective as a crack initiator for sample HX-HT-A-1, so it had a higher number of cycles to failure. The CGR at location 1 for sample HX-HT-A-2 is higher as compared to sample HX-HT-A-1, which could have resulted in a lower number of cycles to failure for this sample.

III) Heat treatment at 1000 °C before and after ablation

Two samples were tested for condition (III) heat treatment at 1000 °C before and after ablation, but fractography results are shown only for sample HX-HTBA-A-1 in Figure 83, while crack growth rates for both samples HX-HTBA-A-1 and HX-HTBA-A-2 are reported. High magnification images of locations 1,2 and 3 in Figure 83a are shown in Figures 84a, 84b and 84c, respectively. Common features observed near the crack initiation site for all the samples are shown in Figure 85, using sample HX-HTBA-A-1 as an example.

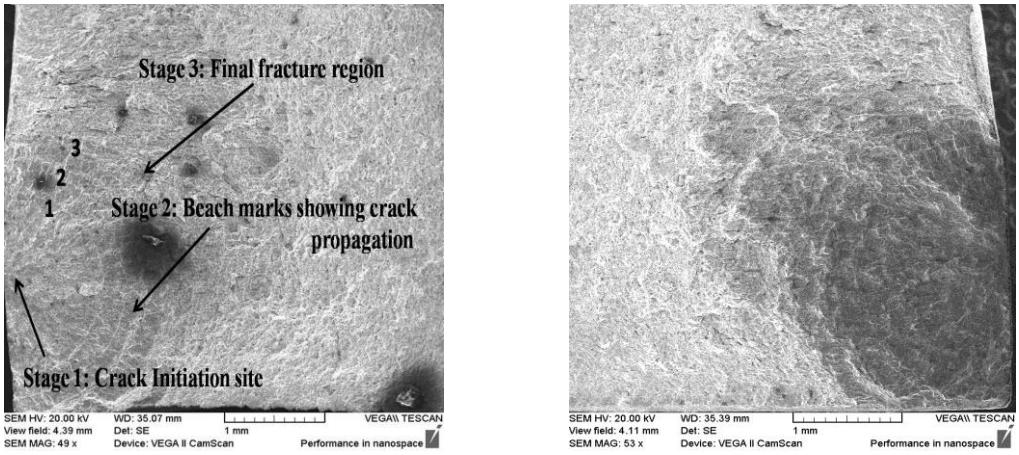

(a) (b)

Figure 83. Fracture surface for Hastelloy X sample HX-HTBA-A-1, condition (III)-heat treatment at 1000°C before and after ablation. (a) Different crack growth stages marked on the surface. (b) Matching fracture surface on the other side of the sample.

Similar trends regarding different fatigue stages were observed for this testing condition. The site near crack initiation always had cleavage-like facets. The local crack propagation direction is different due to different local crystallographic orientation, but the overall crack propagation can be traced by the river-like patterns also the misalignment of cleavage-like planes at grain boundaries could cause stage 1 cracks to tilt or twist, the fracture would reinitiate with a series of parallel steps[104]. As the crack propagates towards stage 2, several planes join and form higher steps

resulting in fewer facets near the beginning of stage 2. Crack growth rates are shown in Table 7 as measured from locations 1, 2 and 3 shown in Figure 83 (a) for samples HX-HTBA-A-1 and HX-HTBA-A-2 tested with condition (III)-Heat treatment at 1000 °C before and after ablation along with CGR results for conditions I and II.

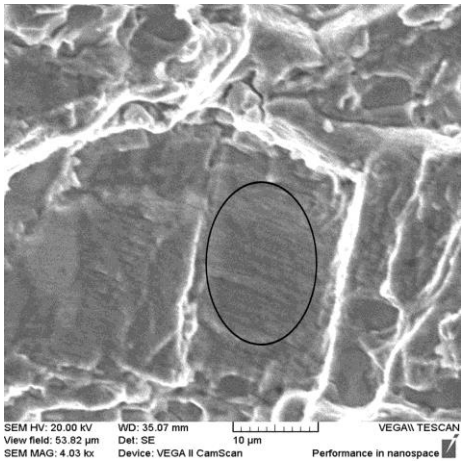

(a)

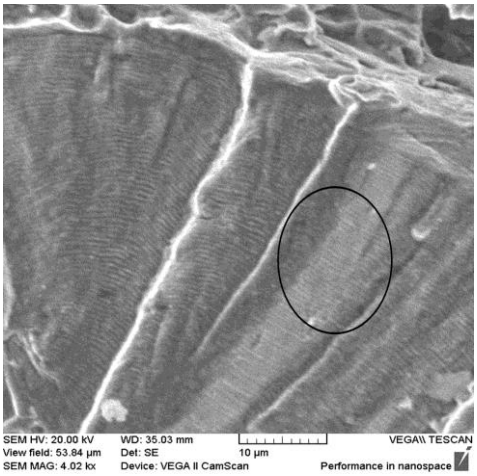

(b)

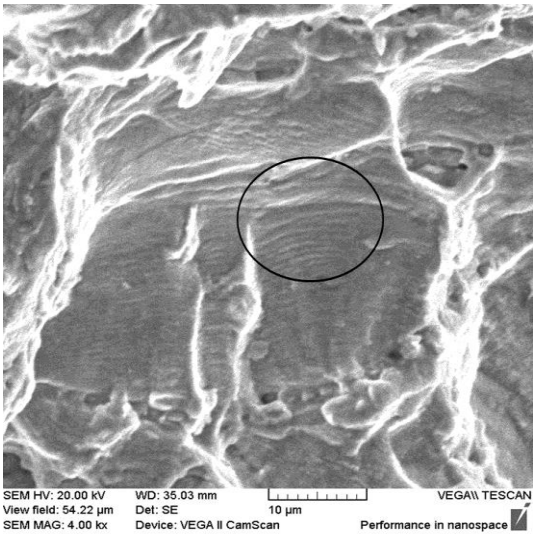

(c)

Figure 84. (a) High magnification image of location 1 in Figure 83, (b) High magnification image of location 2 in Figure 83, (c) High magnification image of location 3 in Figure 83.

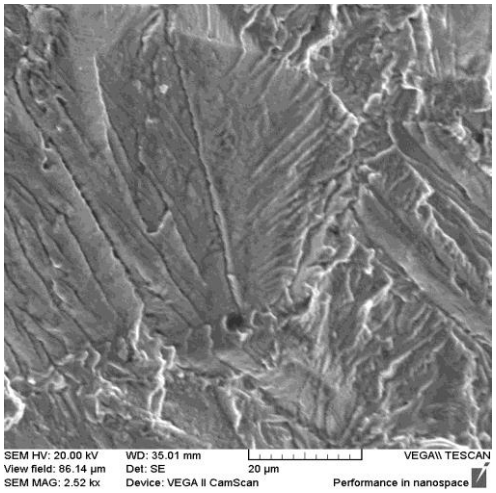

Figure 85. Hastelloy X sample HX-HTBA-A-1, heat treated at 1000°C before and after shooting, near crack initiation.

Table 7. Crack growth rate (µm/cycle) at locations 1, 2 and 3 for Hastelloy X condition I- Heat treatment at 1000°C after ablation-No ablation, condition (II) Heat treatment at 1000°C after ablation and condition (III) Heat treatment at 1000°C- before and after ablation.

Condition	Sample	1	2	3	Final crack length (mm)	Cycles to failure
I	HX-HT-NA-1	0.75	0.69	0.87	2.08	73,989
	HX-HT-NA-2	0.86	1.37	1.3	2.19	80,737
II	HX-HT-A-1	0.66	0.74	1.04	2.28	190,069
	. HX-HT-A-2	1.02	0.70	0.83	2.16	63,954
III	HX-HTBA-A-1	0.75	0.55	0.93	2.19	80,641
	HX-HTBA-A-2	1.27	0.95	0.84	2.46	45,438

As discussed above no direct correlation could be established on effects of ablation on CGR among all conditions, particularly given that the crack initiation sites for samples HX-HTBA-A-1 and HX-HTBA-A-2 were on the surface opposite the ablation. Nonetheless, the presence of the latter seems to be responsible for reducing the number of cycles to nucleate a crack in sample HX-HTBA-A-2 resulting in a shorter fatigue life, but it might not have been as effective for HX-HTBA-A-1,

resulting in a higher number of cycles. For conditions (II) and (III) one sample from each condition sample HX-HT-A-2 and sample HX-HTBA-A-2 had crack growth rate greater than 1µm/cycle at location 1 and their corresponding fatigue life were lower when compared to other samples in its respective testing condition and condition (I)- no ablation, while the sample HX-HT-A-1 and sample HX-HTBA-A-1 had fatigue lives almost the same or higher than condition (I) - no ablation, which suggests that heat treatment process may not have removed the residual stresses. Sample HX-HTBA-A-2 had the highest CGR at location 1 among all samples and had the shortest fatigue life which could be due to a lower number of cycles required to nucleate the crack and consequently low fatigue life. The residual stresses generated due to impacting particles and effectiveness of heat treatment in removing these residual stresses needs to be addressed. To evaluate the magnitude of residual stress generated by the ablation and the effectiveness of heat treatments to remove them can be verified by performing fatigue experiment on ablated sample with and without heat treatment and by measuring the residual stresses.

The damage mechanisms observed on the fracture surface along with the CGR analysis suggest that a mixed mode of damage is occurring, i.e., inter- and transgranular.

Stainless steel 347

Heat treatment at 950° C before and after ablation.

Crack growth analysis along with damage mechanisms are discussed in this section for SS 347. Two samples were tested with condition (III)- Heat treatment at 950 °C before and after ablation for this material. Fractography results are shown only for

sample SS-HTBA-A-1 in Figures86 and 87, but crack growth rate results for samples SS-HTBA-A-1 and SS-HTBA-A-2 are reported.

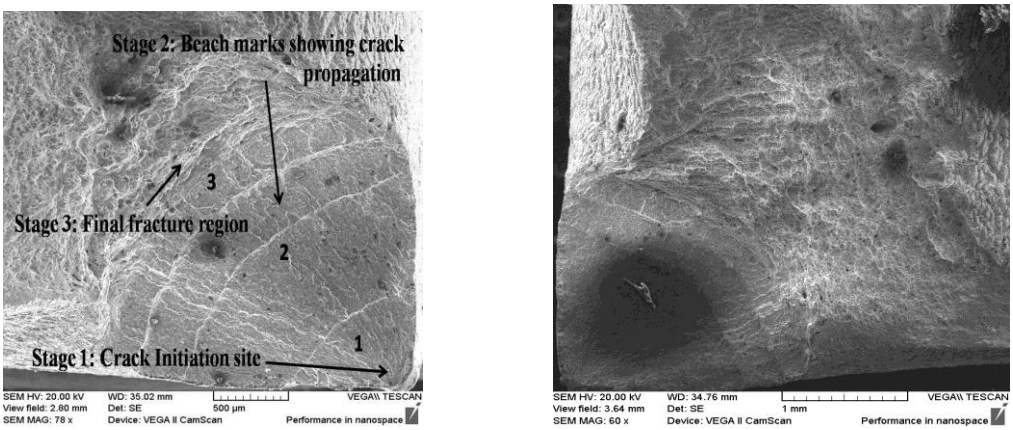

(a) (b)

Figure 86. Fracture surface for the SS 347 sample SS-HTBA-A-1 condition (III)-Heat treatment at 950 °C- before and after ablation. (a) Different crack growth stages marked on the surface. (b) Matching fracture surface on the other side of the sample.

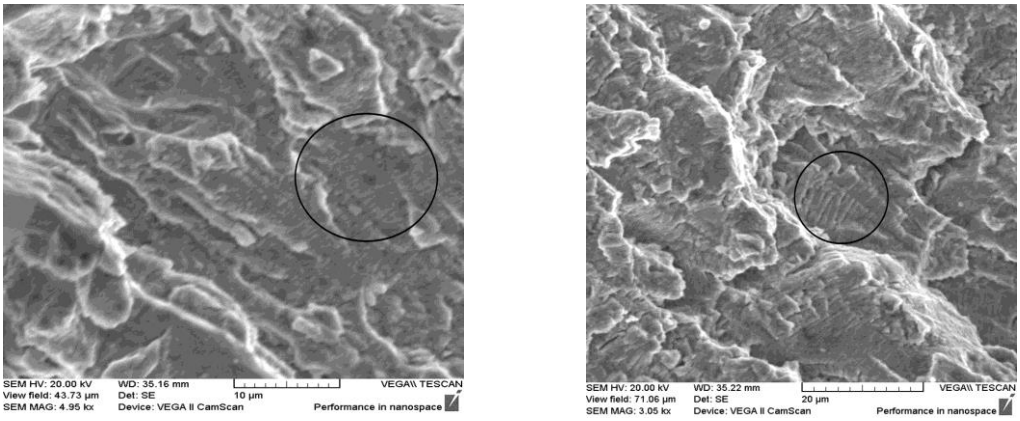

(a)

(b)

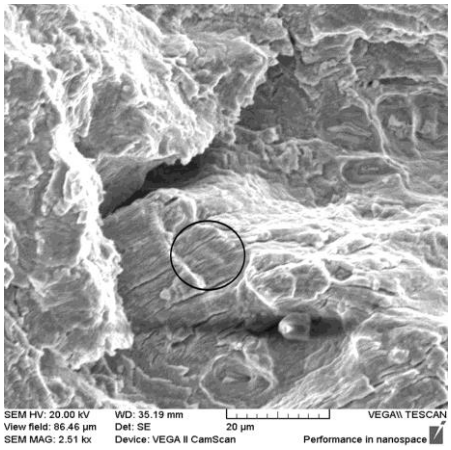

(c)

Figure 87. (a) High magnification image of location 1 in Figure 86. (b) High magnification image of location 2 in Figure 86.(c) High magnification image of location 3 in Figure 86.

Fatigue behavior in terms of fatigue stages 1,2 and 3 for SS 347 was similar to the Hastelloy X samples, except that the first appearance of beach mark was at 0.6 mm from the crack initiation site compared to Hastelloy X, which had the first appearance of beach marks at a distance greater than 1 mm. This suggests that stage 2 started at a shorter crack length in SS 347 than Hastelloy-X. Moreover, striations were poorly defined and were not consistent at locations selected. The CGR results are shown in Table 8 for SS 347 condition (III) Heat treatment at 950 °C-before and after ablation. Note from Table 4 that fatigue tests for SS 347 condition (I)- Heat treatment at 950 °C no-ablation, lasted in the range of million cycles before it was stopped. Given that the sample was not taken to failure, no fractography could be performed, which means that CGR measurements are not available.

Table 8. Results for CGR in SS 347 samples under condition (III) Heat treatment at 950 °C-before and after ablation.

Sample	1(µm/cycle)	2(µm/cycle)	3(µm/cycle)	Final crack length (mm)	Cycles to failure
SS-HTBA-A-1	0.57	0.85	1.04	2.25	133,501
SS-HTBA-A-2	0.59	0.74	1.21	2.47	333,095

The effect of ablation can be clearly seen for SS 347 since the samples with ablation lasted 10^5 to $3x10^5$ cycles as compared to SS 347 samples with no ablation, which lasted > $3x10^6$cycles without breaking. Even though the crack initiation site was on opposite to the ablation surface, the most likely reason for reduced fatigue life is the combined effect of FOD and heat treatment and could have possibly reduced the cycles required to nucleate the crack. The CGR results in Table 8 show the expected increasing trend from location 1 to location 3 and final fracture at crack lengths of 2.25 mm and 2.47 mm, respectively. The CGR analysis used in this study gives a rough estimate, but to get accurate data for crack growth rate direct monitoring of crack length with respect to cycles would be needed. Figures 88, 89 and 90 show typical fracture features observed for SS 347 samples under condition (III) Heat treatment at 950 °C-before and after ablation.

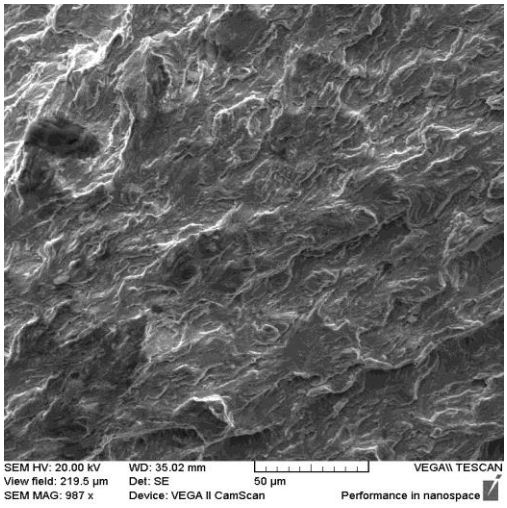

Figure 88.Fractography for SS347 sample SS-HTBA-A-1, heat-treated before and after ablation, near crack initiation.

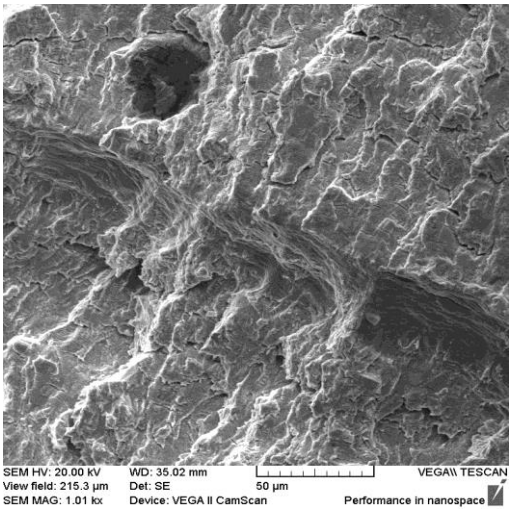

Figure 89.Fractography for SS347 sample SS-HTBA-A-2, heat-treated before and after ablation. Secondary cracks near location "2" of Figure 86a.

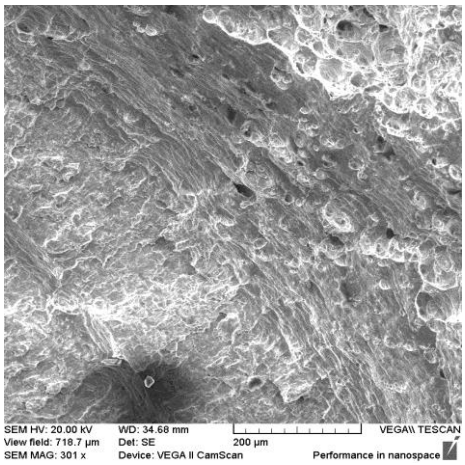

Figure 90.Fractography for SS347 sample SS-HTBA-A-2, heat-treated at 950 °C before and after ablation, showing dimples at final fracture region.

The SS 347 samples also had a transgranular mode of crack initiation and propagation in stage 1 as shown in Figure 88. In stage 2, shown in Figure 89, there were more poorly defined striations than compared to stage 2 of Hastelloy X, which is also evident from the striations observed at locations 1,2 and 3. This could be due to extensive secondary cracking present in the matrix phase[105], which is consistent with the high level of load used. Near stage 3, as shown in Figure 90, coalescence of

dimples can be seen, but they were not seen in Hastelloy X, instead it had transgranular mode of fracture at stage 3. An EDS analysis was conducted on fracture surfaces of Hastelloy X and SS 347 in order to study any secondary phase particles, i.e., precipitates or inclusions present on the crack surface. Observations made during this study are discussed next.

5.8 Precipitate/inclusion analysis

Small particles in the matrix were observed in stages 2 and 3 in all Hastelloy X samples. Figure 91 shows the appearance of one such particle, as well as an EDS point analysis showing high chromium content for the particle, while the point analysis for the matrix material near it shows higher Ni content, as shown in Figure 92, so this particle could be a $M_{23}C_6$-type chromium carbide, also particles with Mo content were observed that could be M_7C-type precipitates. These particles could have played a role in altering crack propagation due to difference in ductility of particles as can be seen in Figure 93a.

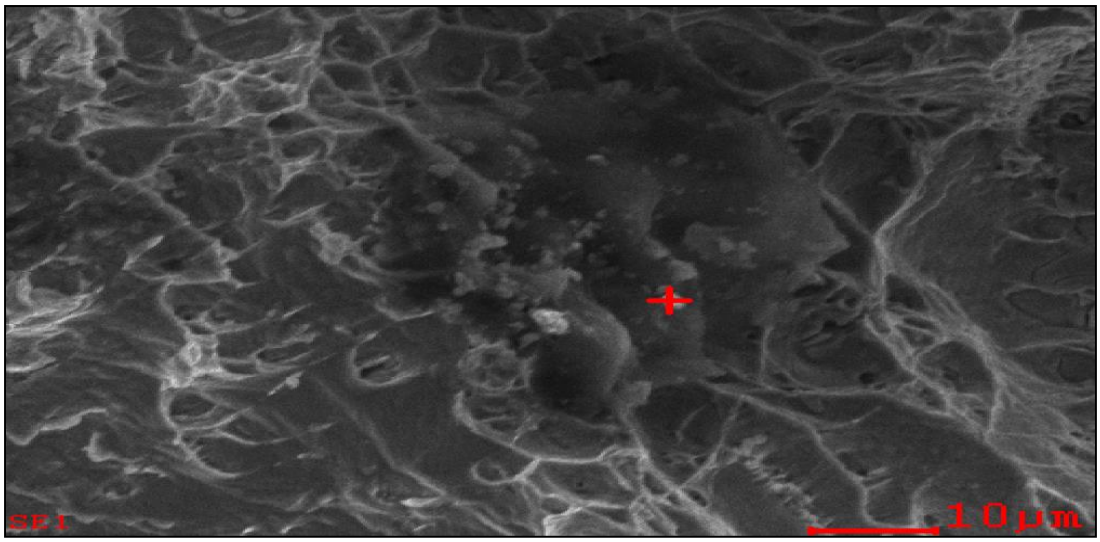

(a)

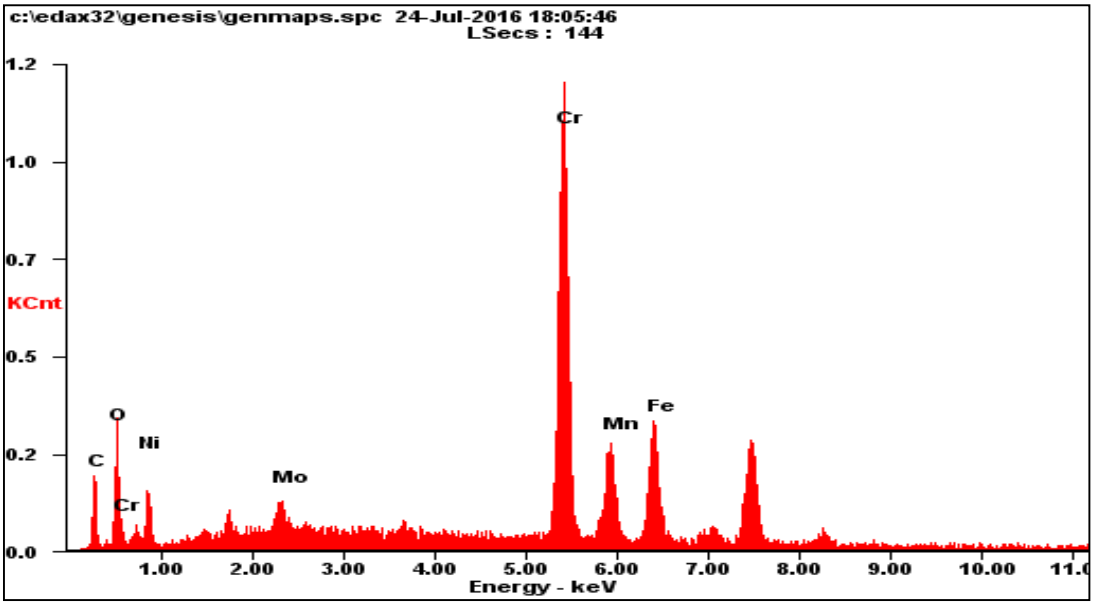

(b)

Figure 91.Hastelloy X sample, non-ablated. a) Fractography showing particle. b) EDS point analysis of the particle.

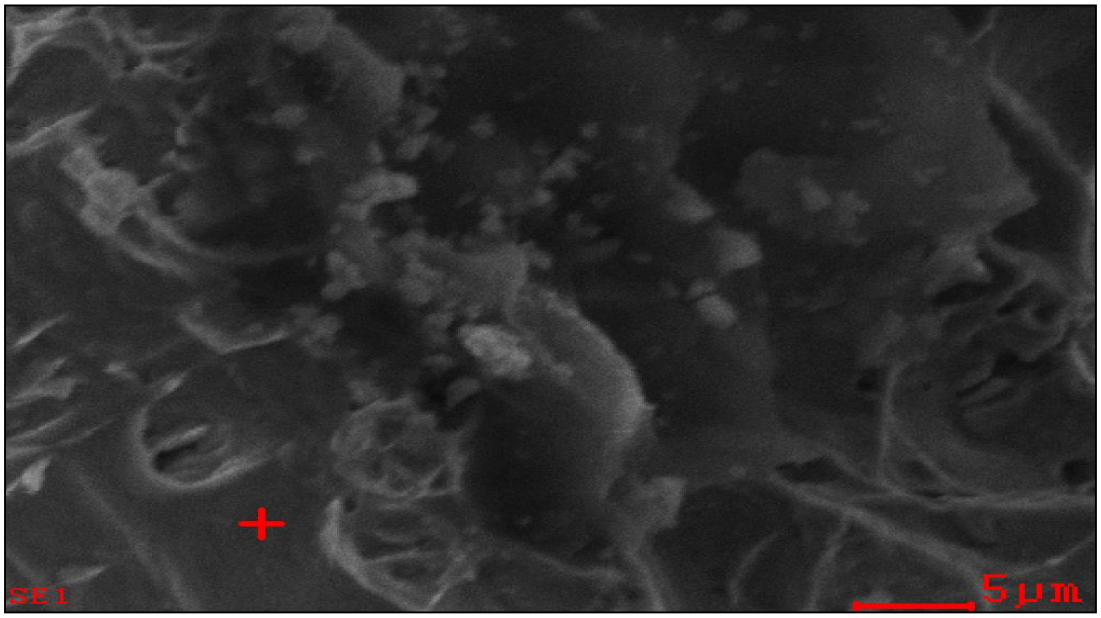

(a)

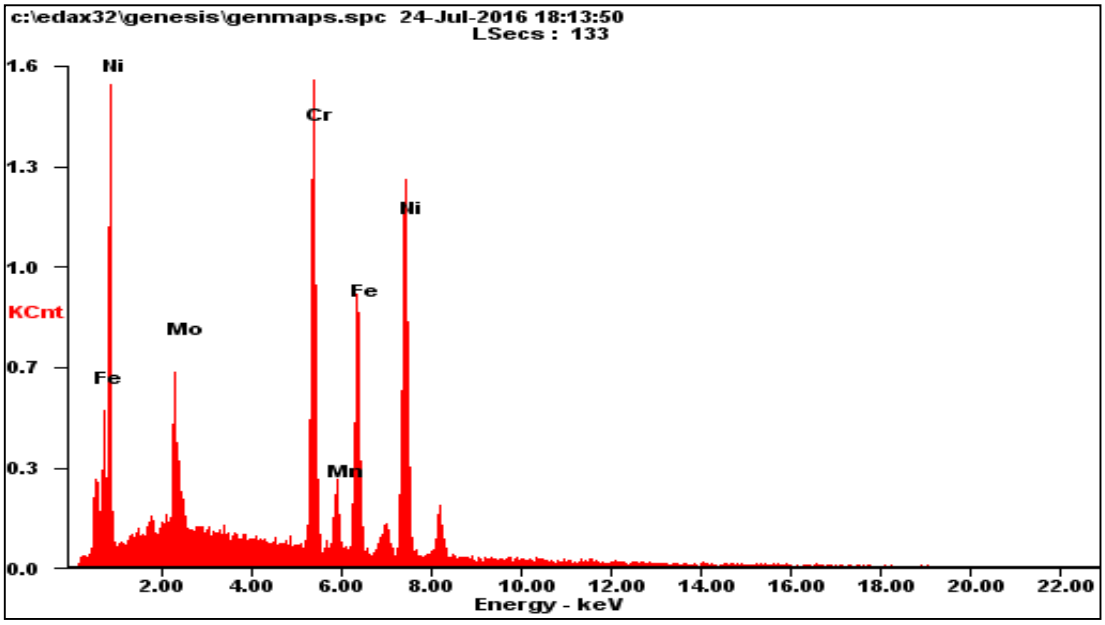

(b)

Figure 92.Hastelloy X sample, non-ablated. a) Fractography showing matrix material. b) EDS point analysis of matrix material.

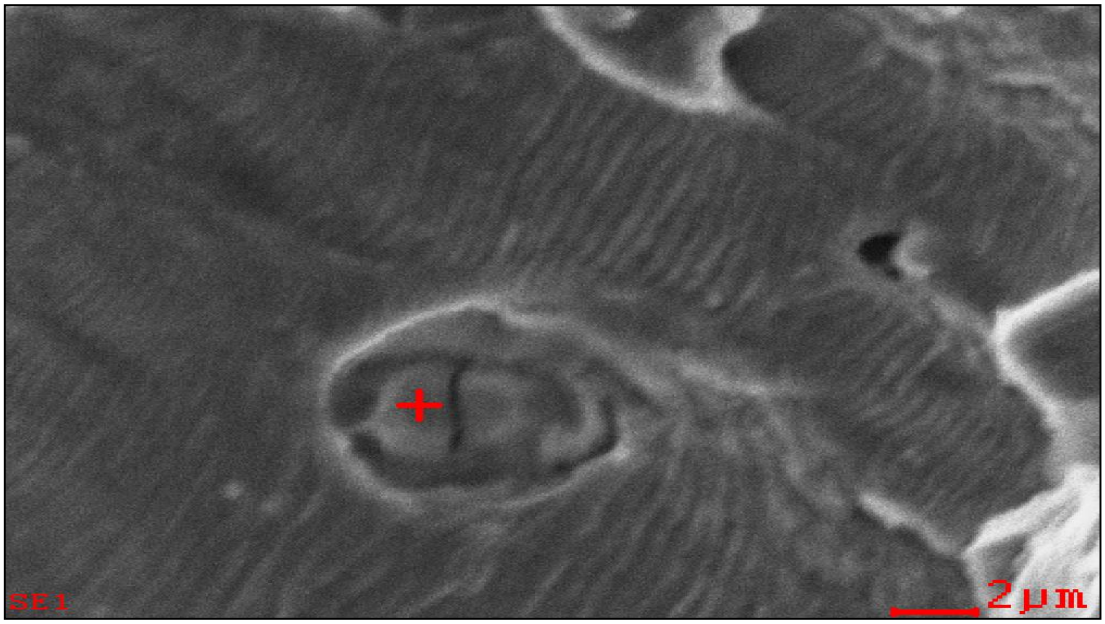

(a)

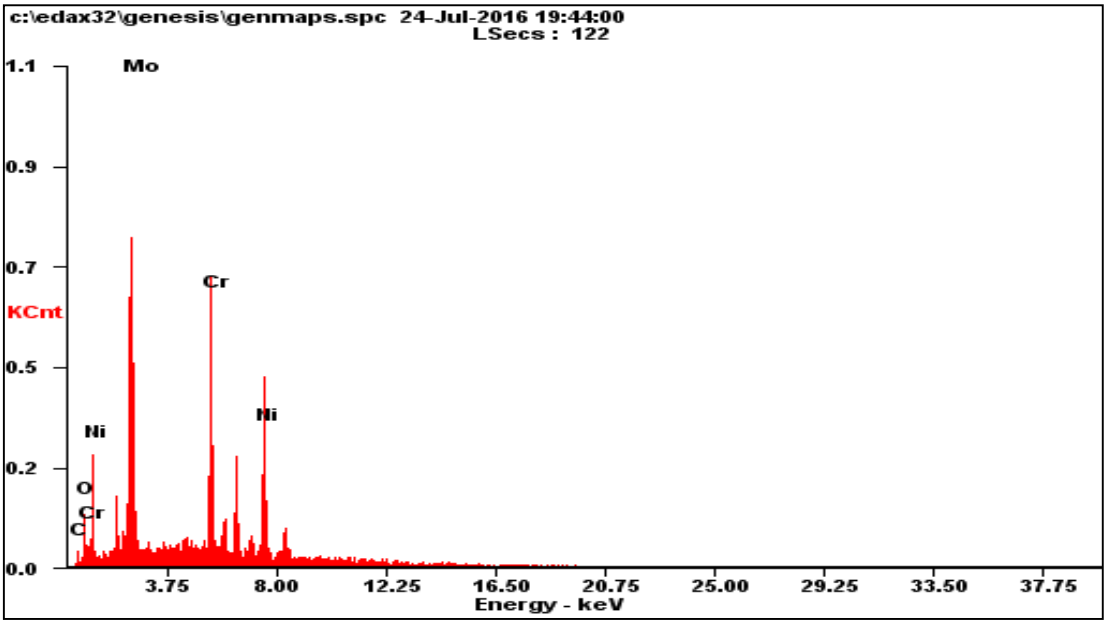

(b)

Figure 93. Hastelloy X sample, heat-treated at 1000°C after ablation. a) Fractography showing fractured particle. b) EDS point analysis of the particle.

In SS 347 precipitates observed were likely to be chromium rich $M_{23}C_6$ type as suggested by the tall chromium peak in the EDS point scan shown in Figure 94. Interestingly niobium-rich particles were observed more frequently than chromium-rich ones, Figure 95 shows the high niobium content of one such particle, which can be expected since niobium and tantalum are added to SS 347 for stabilization and preventing chromium carbide precipitation[55].

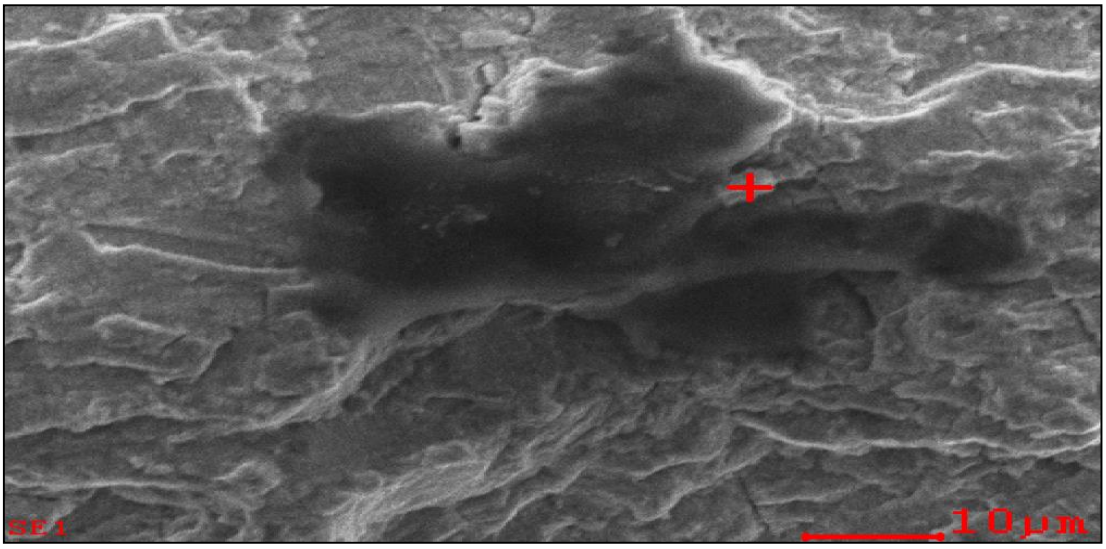

(a)

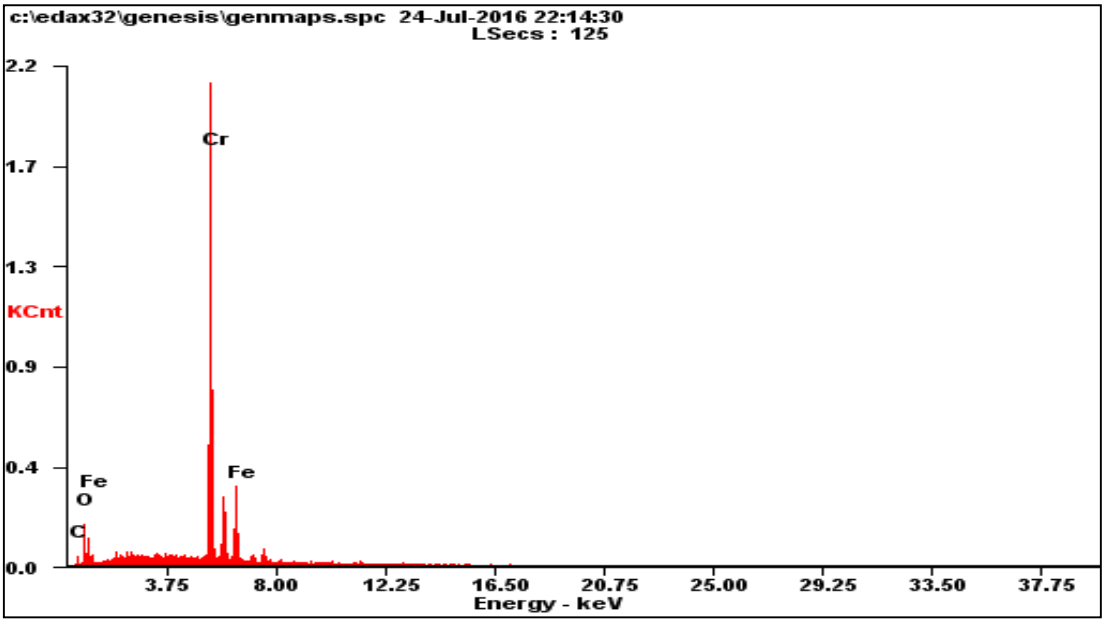

(b)

Figure 94.Sample of SS 347 heat treated at 1000 °C before and after ablation. a) Fractography showing particle on the fracture surface. b) EDS point analysis for the particle.

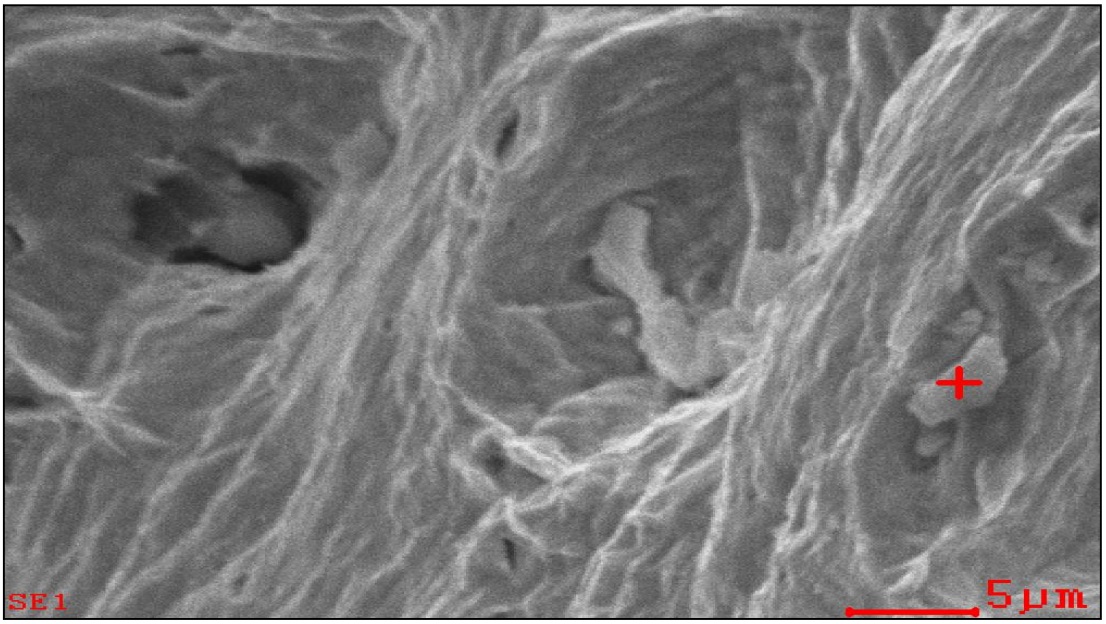

(a)

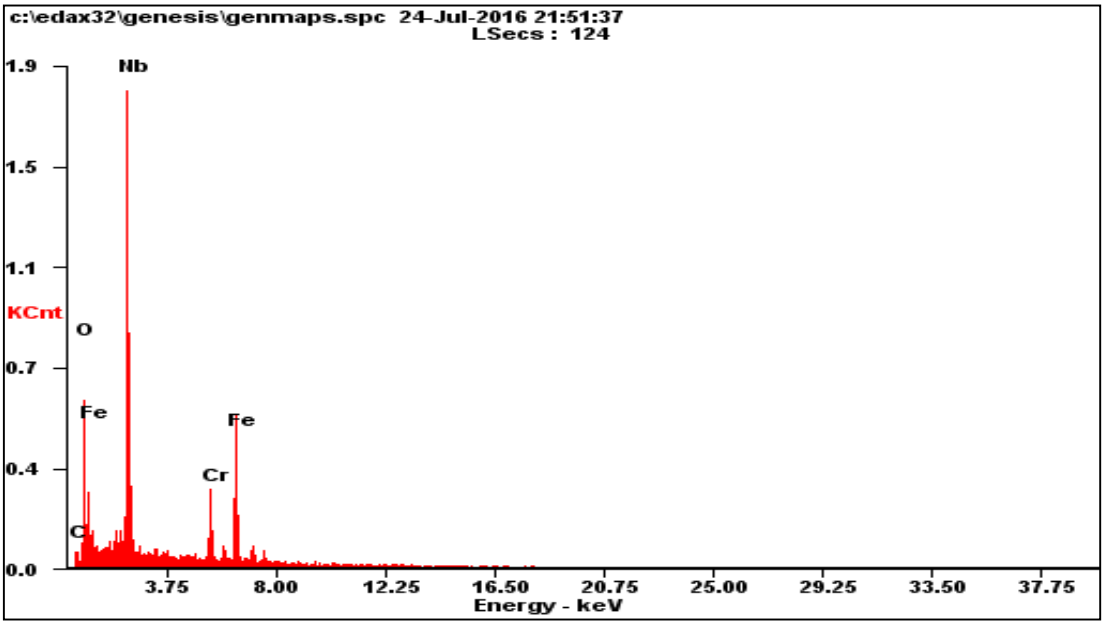

(b)

Figure 95. Sample of SS 347 heat-treated at 950 °C before and after ablation. a) Fractography showing particle on the fracture surface. b) EDS point analysis for the particle.

The particles observed for Hastelloy X and SS 347 can act as obstacles to dislocation movement and pin grain boundaries to prevent them from sliding and these mechanisms improve tensile and creep strength. The dislocations can only move

around particles by either cutting or by passing the particles by the high stress than required to move dislocation in matrix phase. Though these particles help increasing the strength of the materials, they can be detrimental depending on the particle size, distance between particles and volume fraction of the particles present. They also interact with the propagating crack, as can be seen clearly in Figure 93a, where striations can be seen to go around a broken particle. Broken particles such as this can also play a role on crack nucleation[106]. It is likely that the heat treatments increased the size of the particles, making them more susceptible to cracking [106]. In addition, broken particles can act as nucleation sites, and can also help the propagating crack [103].To know the precise effects and mechanisms by which the precipitates and inclusions affect fatigue life in this case, a statistical analysis of precipitate sizes before and after heat treatments would need to be conducted, which would benefit substantially from the use of Transmission Electron Microscopy, which provides high resolution and reveals interaction between dislocations and precipitates in matrix phase. Unfortunately, this is beyond the scope of this work.

The discussion provided so far centered on fracture surfaces, but in the next section a macroscopic analysis of the damage on the ablation surface is offered.

5.9 Macroscopic damage observations

Hastelloy X and SS 347

Ablation regions were analyzed using SEM and also at low magnification using stereo optical microscopy for Hastelloy X and SS 347 samples. Figure 96 shows the surface appearance for Hastelloy X heat treated after ablation.

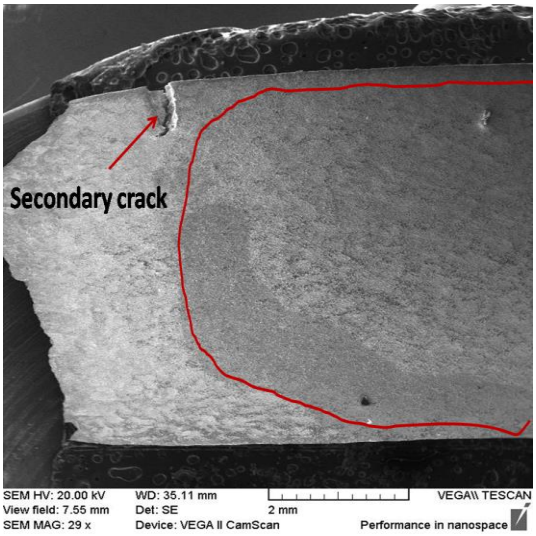

Figure96.Samples of Hastelloy X heat-treated after ablation (ablation region enclosed in the red curve).

A large secondary crack was observed right outside the ablation region as shown in Figure 96, which is consistent with crack nucleation behavior observed around FOD craters [68,69]. The outside surface for Hastelloy X sample under condition (III), i.e., heat-treated before and after ablation is shown in Figure 97a. Just like the sample for condition (II), a cluster of secondary cracks right outside the ablation area was observed.

Figures 97b and 97c show high magnification images from the middle area of the ablated region and from the rim (boundary of ablation), respectively, and at both locations secondary cracks were observed. Few secondary cracks were observed on the other side of the ablation as shown in figure 97d, the presence of secondary cracks all around the rim of the ablation can possibly grow and merge to form a large crack or can help removing a piece of material.

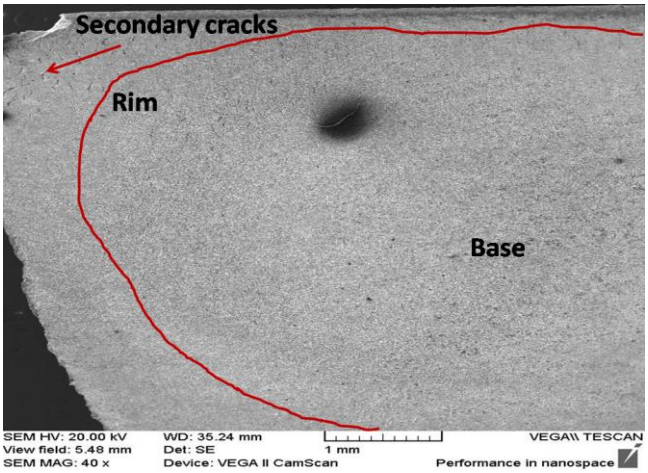

(a)

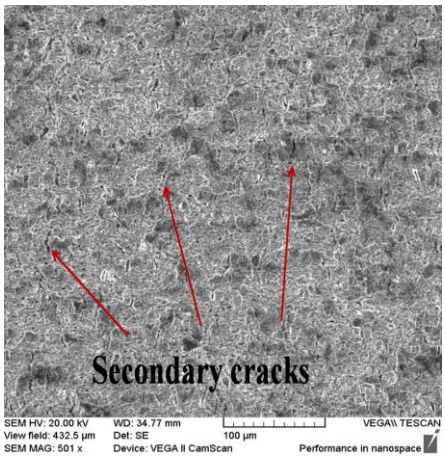

(b)

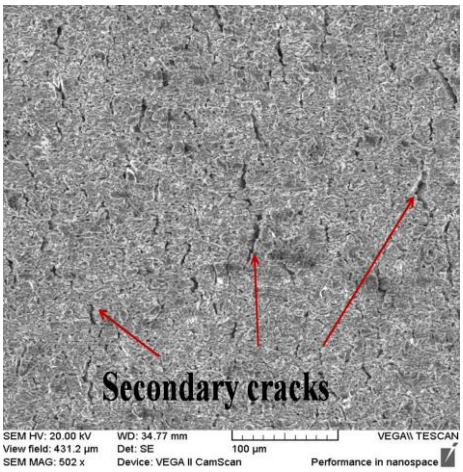

(c)

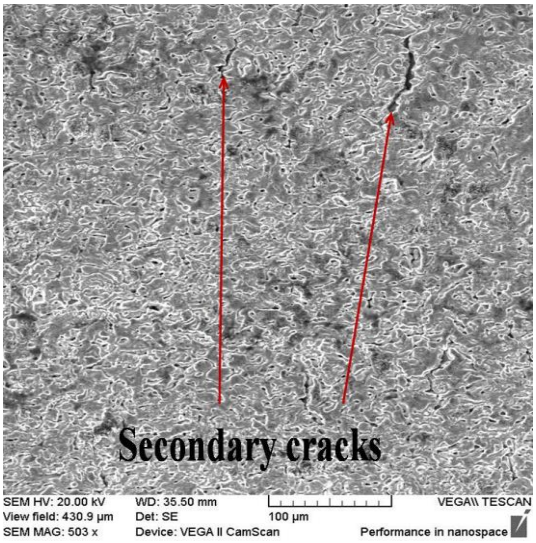

(d)

Figure 97. Hastelloy X heat-treated before and after ablation a) Macroscopic view of ablation area enclosed by red mark and secondary cracks outside the rim. (b) Secondary crack at the middle (base) of the ablation region. (c) Secondary cracks at

the left side rim of the ablation region. (d) Secondary cracks at the right side (other side) rim of the ablation region.

It can be said that the secondary crack at the rim were wide with high crack density while at the middle (base) cracks were narrow and had less crack density. Similar cracking patterns were observed for condition (II) Hastelloy X-heat treated after ablation at the rim and the middle area of the ablation region, but were not as wide as observed for Hastelloy X condition (III). These wide spread secondary cracks were not observed on the non-ablated Hastelloy X sample as can be seen in Figure 98. However, small cracks were occasionally observed that could have failed to grow and propagate, also the other sample tested under the same condition had a surface secondary crack that failed to propagate.

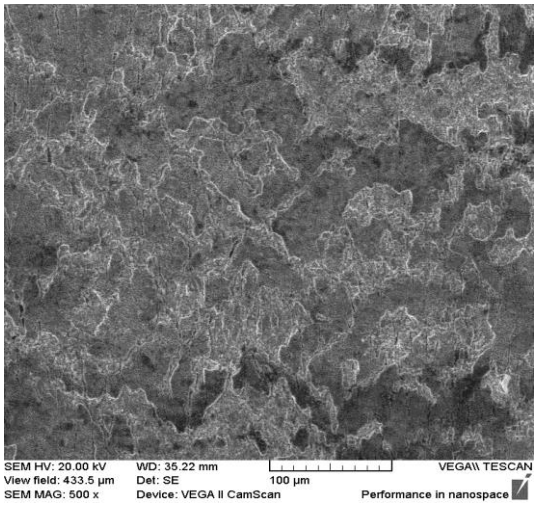

Figure 98. Hastelloy X no-ablation sample.

Note from Table 4 that SS 347 samples with no ablation lasted for more than 3 million cycles. One of them had a surface crack near the edge of the gauge length that did not propagate and it is shown in Figure 99. An examination of the surface for the SS 347 sample heat treated before and after ablation, shown in Figure 100,revealed

extensive damage and rust formation after the fatigue test, and SEM images showing secondary cracks on this surface are shown in Figure 101.

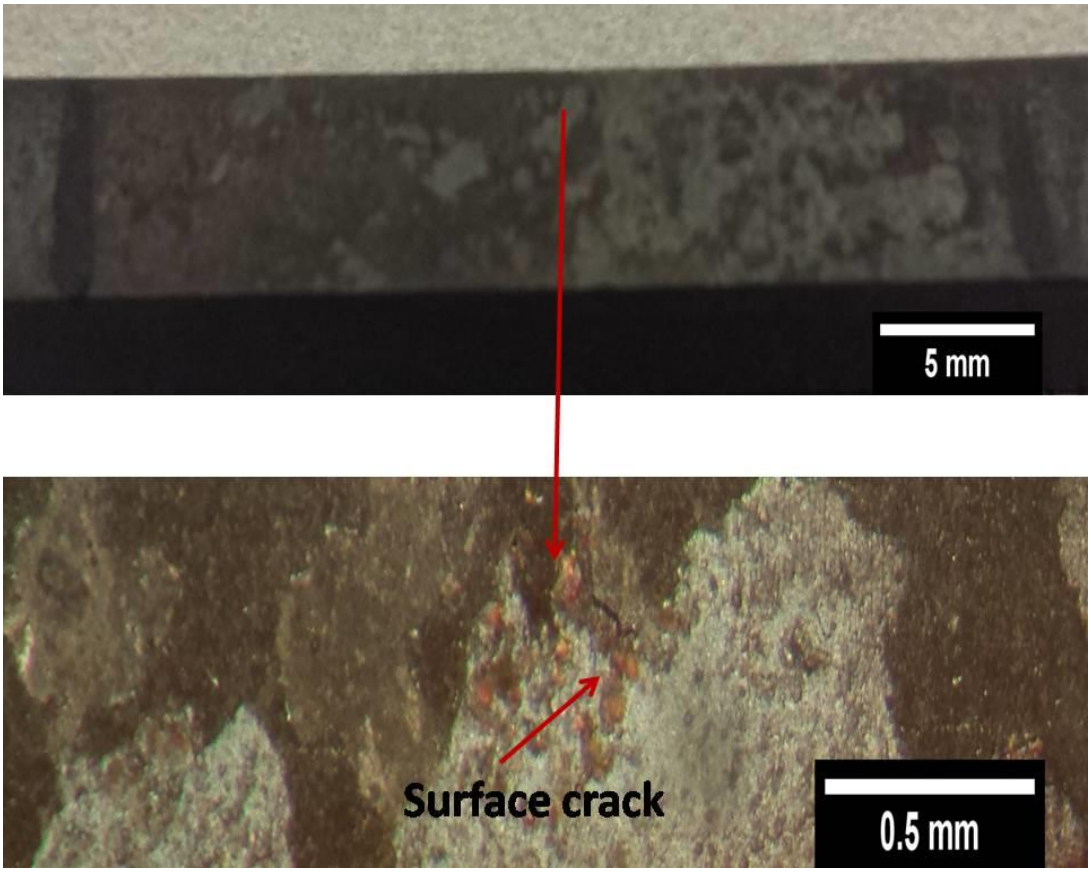

Figure 99. SS 347 sample heat treated, but with no ablation.

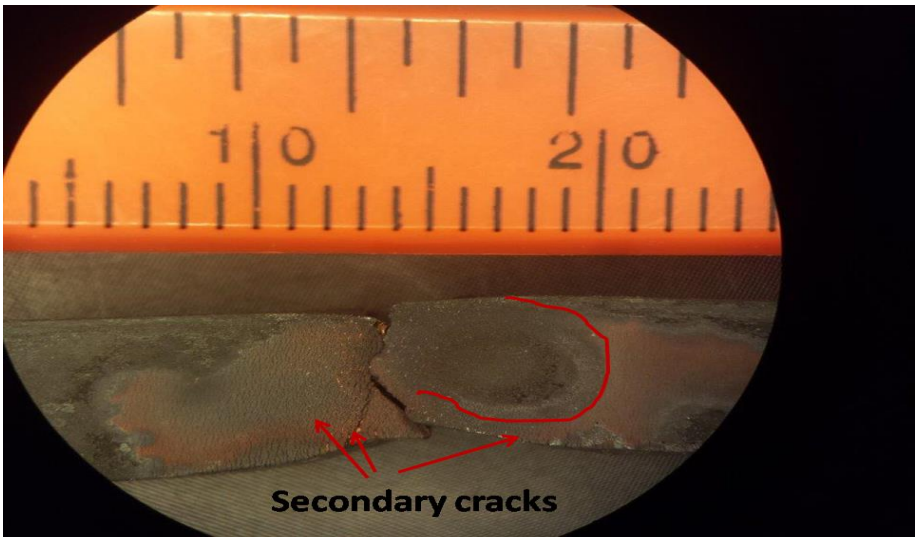

Figure 100. SS 347 sample heat-treated before and after ablation showing extensive secondary cracks and rusty surface appearance after the test.

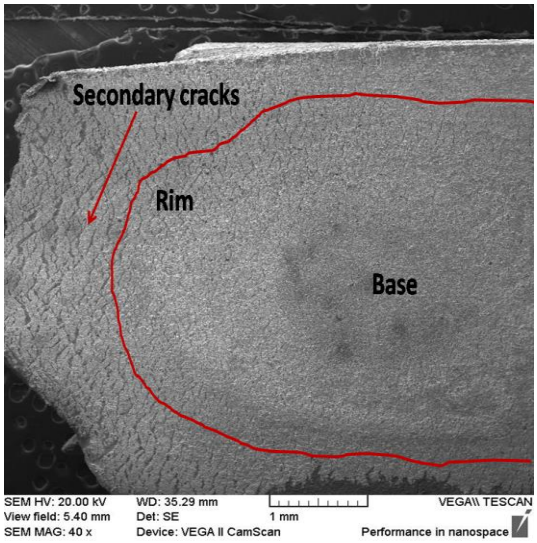
Secondary cracks
Rim
Base
SEM HV: 20.00 kV
View field: 5.40 mm
SEM MAG: 40 x
WD: 35.29 mm
Det: SE
Device: VEGA II CamScan
1 mm
VEGA\\ TESCAN
Performance in nanospace

(a)

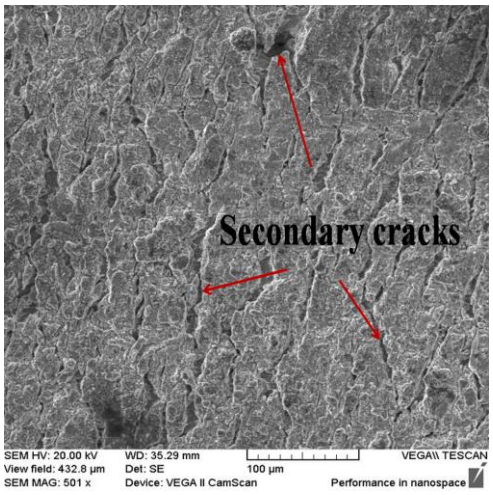
Secondary cracks
SEM HV: 20.00 kV
View field: 432.8 µm
SEM MAG: 501 x
WD: 35.29 mm
Det: SE
Device: VEGA II CamScan
100 µm
VEGA\\ TESCAN
Performance in nanospace

(b)

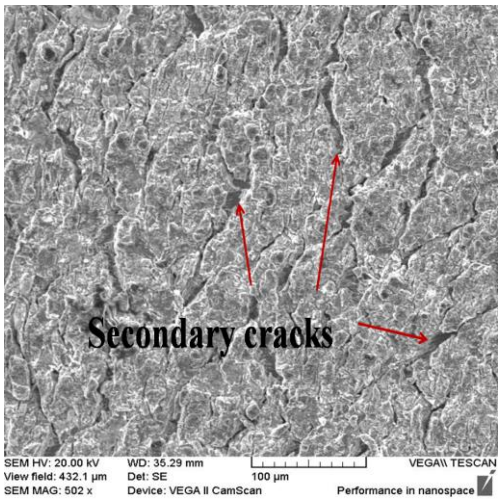
Secondary cracks
SEM HV: 20.00 kV
View field: 432.1 µm
SEM MAG: 502 x
WD: 35.29 mm
Det: SE
Device: VEGA II CamScan
100 µm
VEGA\\ TESCAN
Performance in nanospace

(c)

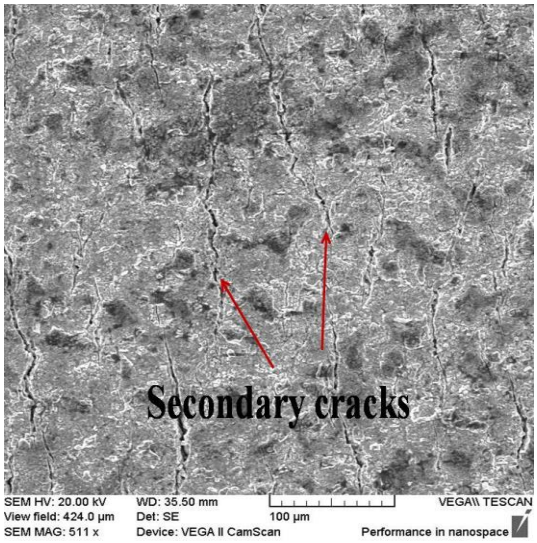

(d)

Figure 101.SS 347 sample heat-treated before and after ablation a) Macroscopic view showing secondary cracks and ablation region enclosed by red curve. b) Secondary crack at the middle region of the ablation. c) Secondary cracks at the left side rim of the ablation. (d) Secondary cracks at the right side rim (other side) of the ablation.

The macroscopic view of the SS 347 sample shown in Figure 101a suggests that FOD can create more damage on stainless steel 347 than in Hastelloy X. As was the case for the ablation region in Hastelloy X samples, secondary cracks at the middle region of the ablation area for SS 347 were narrower with low crack density as shown in Figure 101b and at the rim area the cracks were wider with high crack density, as shown in Figure 101c. These secondary cracks were present extensively around the rim and extended beyond it, Figure 101d shows different locations of secondary crack at the rim.

On non-ablated samples of Hastelloy X and SS 347 very few cracks were observed as compared to ablated samples, which could have failed to propagate during fatigue cycling. Depending on the impact velocity micro cracks at the rim of FOD site due to single spherical projectile at higher velocity (300m/s) can emerge[107]by material pile up due to plastic flow of the material, although in the current study a stream of multiple particles as projectiles was used, the secondary

cracks observed in the analysis done on the fractured samples at the rim were similar to those reported in the literature due to a single spherical projectile. However, in the current study these cracks were observed at ~200 m/s, and the occurrence of microcrack at the middle (base) of the ablation region does not seem to have been reported in the literature, but was observed in the case of Hastelloy X and SS 347, which suggests that the heat treatments were able to relieve the compressive residual stresses that arise there due to particle impacts, and the stress concentration at that location was able to favor cracking. The high density of microcracks observed, many of which were able to grow as long secondary cracks for samples with ablation (while samples without ablation did not have them), suggests that ablation is indeed causing multisite cracking, in addition to erosion of the surface, and also these crack could grow and coalesce to remove a piece of material, which is consistent with damage observed in AORA's turbine.

Residual stresses in the impact region can increase the local mean stress that causes fatigue and consequently accelerates the crack initiation and propagation depending on the impact velocity and loading condition [66], for single spherical projectile residual stresses region can be described as a tensile region around the bulk compressive residual stress due to balance between tensile and compressive stresses, as is the case for shot peening [66], surface area at the base of the impact and around the impact rim, i.e., the boundary of the impact area where chances of microcracks formation are higher due to material pile up. This is consistent with secondary cracks observed around the rim and at the shallow surface right at the base of the impact area in the analysis done on the fractured samples due to alumina particles.

As mentioned in section 2.5 of the introduction, at high applied stress and high impact velocity (300m/s), cracks tend to initiate at the crater rim, for low impact (200m/s) velocity cracks initiated at the base of the impact and at low applied stress and low impact velocity cracks initiated away from the impact area where tensile residual stresses are likely to be present. In the current study, the estimated velocity of ablation/impact was ~200 m/s, high applied stresses were used for fatigue testing, crack initiated on the same surface but outside from the ablation area for one Hastelloy X sample (HX-HT-A-2), while in all the other samples for both materials cracks initiated on the opposite surface to the ablated surface.

The crack initiation site observed in this study agrees only partially with reported effects of low velocity and low stresses level to initiate crack away from the impact, since crack initiated away from the impact at low velocity and high stress. The partial disagreement is thought to be due to the striking of alumina particles that can act as non-optimized shot peening and could create residual stress fields around the impact/ablation different from those reported in the literature with single particle impact. Also due to the heat treatment used in the ablation samples, the residual stress would tend to relax and the depth of the residual stress field would affect the fatigue property, but cracks are likely to initiate where high tensile residual stresses are present. However, the impact of particles at 23° angle is possibly favoring multisite cracking around the ablation site, which could also probably serve as a potential site for crack initiation. The presence of multisite damage is likely the key factor on reduction of fatigue life for SS 347 samples, as effective reductions of cross-section would take place and increase the overall stress level, as well as cause stress redistribution. This, combined with the fact that the secondary cracks arrested, might

partially explain why the fatal crack nucleated and propagated on the surface opposite to the ablation region.

6. CONCLUSIONS AND FUTURE WORK

This study initiated with preliminary characterization of materials by SEM, XRD and hardness tests, along with building a gas gun system that would allow to reach the end goal of performing an investigation of how foreign object damage produced by a stream of particles impacting metallic components at high velocity might affect high temperature fatigue performance of metallic alloys of interest to AORA under oxidizing conditions. The results from characterization and testing lead to the following conclusions:

- XRD and EDS analysis of debris found in AORA's system revealed that the most common phases present were Cristobalite, aluminum-silicon oxide and Corundum (Al_2O_3). Based on these findings and direct SEM imaging of particles present in the debris, it was concluded that 50 μm alumina particles would provide a good substitute to simulate FOD inside AORA's system in the lab.
- High temperature hardness test and tensile tests indicate that Hastelloy X and SS 347 an undergo significant deterioration in its mechanical properties when exposed to moderately high temperatures, well within their operating regimes, when exposed to very high temperatures beforehand.
- Hardness test, tensile test and fatigue test results indicate that SS 347 is highly susceptible to combined effect of damage caused by FOD and high temperature compared to Hastelloy X.
- Fatigue results for Hastelloy X samples tested under different conditions, i.e., heat treated at 1000 °C-no ablation (I), heat treated at 1000 °C-after ablation (II) and heat treated at 1000 °C-after ablation (III), suggest that FOD could be

playing a role to some extent in reducing the life of ablated samples to some extent, but needs a more detailed study,

- Fatigue results for SS 347 samples tested with heat treatments at 950°C-before and after ablation showed that effects from FOD are clear and are reducing the fatigue life as compared to samples heat treated at 950°C with no ablation.
- Fatigue loading in samples with FOD is creating multisite damage for Hastelloy X and SS 347 when compared to samples without FOD, which is consistent with the damage observed in AORA's system. The multisite damage can lead to the crack leading to final fatigue failure or small cracks could grow to merge and eventually remove pieces of material.

Based on the entire study and results obtained some suggestions for future work are made below:

- The lab scale FOD experiment can be conducted using a stream of particles aimed at a sample held at high temperature to simulate better the condition of temperature inside AORA's turbine. Heating the reservoir of gas used to propel the particles and the barrel of the gas gun should also improve the experiment.
- Increase the pressure of the gas used for ablation and switch it from nitrogen to helium to generate higher particle velocities at impact as seen in AORA's system, where impact velocities of 500 m/s can occur.
- A FEM model may be created for the impact made by gas gun to obtain a numerical solution of residual stress fields generated by striking of particles and can also be verified by performing residual stress measurement via X-ray diffraction.

- A fatigue test program with larger number of samples needs to be carried out under each condition. This can be coupled with monitoring of crack growth with respect to number of cycles to generate accurate da/dN vs. ΔK crack growth curves so that nucleation and propagation lives can be estimated, and the effects of ablation on nucleation can be understood better.

REFERENCES

[1] O. Behar, A. Khellaf, and K. Mohammedi, “A review of studies on central receiver solar thermal power plants,” *Renew. Sustain. Energy Rev.*, vol. 23, pp. 12–39, 2013.

[2] Z. En, “Solar energy in progress and future research trends,” *Prog. Energy Combust. Sci.*, vol. 30, pp. 367–416, 2004.

[3] B. F. Towler, “Solar Power,” in *The Future of Energy*, 2014, pp. 161–185.

[4] V. Devabhaktuni, M. Alam, S. Shekara, S. Reddy, R. C. Green, D. Nims, and C. Near, “Solar energy : Trends and enabling technologies,” *Renew. Sustain. Energy Rev.*, vol. 19, pp. 555–564, 2013.

[5] M. Romero-Alvarez and Eduardo Zarza, “Concentrating Solar Thermal Power,” *Handb. Energy Effic. Renew. Energy*, vol. 20070849, pp. 21.1–21.97, 2007.

[6] I. Dincer, “Renewable energy and sustainable development : a crucial review,” vol. 4, pp. 157–175, 2000.

[7] P. Viebahn, Y. Lechon, and F. Trieb, “The potential role of concentrated solar power (CSP) in Africa and Europe-A dynamic assessment of technology development, cost development and life cycle inventories until 2050,” *Energy Policy*, vol. 39, no. 8, pp. 4420–4430, 2011.

[8] S. K. G T Machinda, S P Chowdhury, R Arscott, “Concentrating Solar Thermal Power Technologies : A Review,” in *2011 Annual IEEE India Conference (2011)*, 2011, pp. 1–6.

[9] H. Gunerhan, A. Hepbasli, and U. Giresunlu, “Environmental Impacts from the Solar Energy Systems,” *Energy Sources, Part A Recover. Util. Environ. Eff.*, vol. 31, no. 2, pp. 131–138, 2008.

[10] H. Scheer, “Solar energy’s economic and social benefits,” *Sol. Energy Mater. Sol. Cells*, vol. 38, no. 1–4, pp. 555–568, 1995.

[11] M. Rodriguez, “The Social and Economic Impacts of Clean Energy Technology Exportation,” in *IFRI Energy Center*, 2012.

[12] P. Schwarzbözl, R. Buck, C. Sugarmen, A. Ring, M. J. Marcos Crespo, P. Altwegg, and J. Enrile, "Solar gas turbine systems: Design, cost and perspectives," *Sol. Energy*, vol. 80, no. 10, pp. 1231–1240, 2006.

[13] H. L. Zhanga and G. C. , J. Baeyens b, J. Degreve, "Concentrated solar power plants : Review and design methodology," *Renew. Sustain. Energy Rev.*, vol. 22, pp. 466–481, 2013.

[14] T. Fend, "High porosity materials as volumetric receivers for solar energetics," *Opt. Appl.*, vol. 40, no. 2, pp. 271–284, 2010.

[15] "www.aora-solar.com." .

[16] H. Müller-Steinhagen and F. Trieb, "Concentrating solar power - A review of the technology," *Q. R. Acad. Eng.*, vol. 18, pp. 43–50, 2004.

[17] J. Karni, a. Kribus, R. Rubin, and P. Doron, "The 'Porcupine': A Novel High-Flux Absorber for Volumetric Solar Receivers," *J. Sol. Energy Eng.*, vol. 120, no. 2, p. 85, 1998.

[18] A. L. Ávila-Marín, "Volumetric receivers in Solar Thermal Power Plants with Central Receiver System technology: A review," *Sol. Energy*, vol. 85, no. 5, pp. 891–910, 2011.

[19] Prashant Karhade, "Concentrated Solar Thermal Technology – Part II," 2015. .

[20] C. K. Ho and B. D. Iverson, "Review of high-temperature central receiver designs for concentrating solar power," *Renew. Sustain. Energy Rev.*, vol. 29, pp. 835–846, 2014.

[21] V. B. T. Goli, K C, S.V. Kondi, "Principles and Working of Microturbine," *IJIERT*, no. Speical Issue, February, pp. 1–7, 2015.

[22] R. H. Staunton and R. Ozpineci, "Microturbine power conversion technology review," pp. 1–30, 2003.

[23] M. A. Rosa do Nascimento, L. de Oliveira Rodrigues, E. Cruz dos Santos, E. E. Batista Gomes, F. L. Goulart Dias, E. I. Gutiérrez Velásques, and R. A. Miranda Carrillo, "Micro Gas Turbine Engine: A Review," *Prog. Gas Turbine Perform.*, pp. 107–141, 2013.

[24] N. S. Hiroshi Saito, John Latcovich, Mike Fusselbaugh, Mialn Dinets, Koichi Hattori, “Micro Gas Turbines, Risks and Markets,” in *IMIA Conference*, 2003.

[25] P. Stinton, David and A. Karnitz, Michael, “MICROTURBINE MATERIALS FY 1999 Prepared by : For : Department of Energy Energy Efficiency and Renewable Energy,” *Progr. Manag.*, 1999.

[26] R. J. E. Glenny, J. E. Northwood, and a. B. Smith, “Materials for Gas Turbines,” *Int. Mater. Rev.*, vol. 20, no. 1, pp. 1–28, 1975.

[27] Stephen Gillette, “Microturbine Technology Matures,” 2010. .

[28] T. Shukla, “Micro gas turbine Engine: A Review,” vol. 2, no. 3, pp. 116–120, 2013.

[29] T. H. Hyde, L. Xia, A. A. Becker, and W. Sun, “Fatigue, Creep And Creep/Fatigue Behaviour of a Nickel Base Superalloy at 700°C,” *Fatigue Fract. Eng. Mater. Struct.*, vol. 20, no. 9, pp. 1295–1303, 1997.

[30] J. Peters and R. Ritchie, “Foreign-object damage and high-cycle fatigue of Ti–6Al–4V,” *Mater. Sci. Eng. A*, vol. 321, pp. 597–601, 2001.

[31] S. M. Marandi, K. Rahmani, and M. Tajdari, “Foreign object damage on the leading edge of gas turbine blade,” *Trans. Famena*, vol. 33, pp. 65–75, 2014.

[32] T. J. Carter, “Common failures in gas turbine blades,” *Eng. Fail. Anal.*, vol. 12, no. 2, pp. 237–247, 2005.

[33] “Geddes, Blaine, Leon, Hugo, and Huang, Xiao. Superalloys : Alloying and Performance. Materials Park, OH, USA: A S M International, 2010. ProQuest ebrary. Web. 22 November 2015. Copyright © 2010. A S M International. All rights reserved.,” no. November, 2015.

[34] J. Pelleg, *Mechanical Properties of Materials*. .

[35] X. Geddes, Blaine, Leon, Hugo, and Huang, “Superalloys : Alloying and Performance. Materials Park, OH, USA: A S M International, 2010. ProQuest ebrary. Web. 22 Novemb,” no. November, 2015.

[36] C. H. Lund, “Physical metallurgy of nickel-base superalloys,” 1961.

[37] C. T. Sims, “A History of Superalloy Metallurgy for Superalloy Metallurgists,” *Superalloys 1984*, pp. 399–419, 1984.

[38] S. S. Handa, “Precipitation of Carbides in a Ni-based Superalloy,” 2014.

[39] T. M. Pollock and S. Tin, “Nickel-Based Superalloys for Advanced Turbine Engines: Chemistry, Microstructure and Properties,” *J. Propuls. Power*, vol. 22, no. 2, pp. 361–374, 2006.

[40] A. Pineau and S. D. Antolovich, “High temperature fatigue of nickel-base superalloys - A review with special emphasis on deformation modes and oxidation,” *Eng. Fail. Anal.*, vol. 16, no. 8, pp. 2668–2697, 2009.

[41] M. J. Donachie, “Superalloy: A Technical Guide (2nd Edition). Materials Park, OH, USA: ASM International, 2000. ProQuest ebrary. Web. 14 November 2015. Copyright © 2000. ASM International. All rights reserved.,” in *Superalloy: A Technical Guide (2nd Edition)*, no. November, 2015, pp. 25–39.

[42] M. J. Donachie, “Superalloys: A Technical Guide (2nd Edition). Materials Park, OH, USA: ASM International, 2000. ProQuest ebrary. Web. 14 November 2015. Copyright © 2000. ASM International. All rights reserved.,” in *Superalloys: A Technical Guide*, no. November, 2015, pp. 211–286.

[43] A. M. Weinberg, “Oak Ridge National Laboratory.,” *Science*, vol. 109, no. 2828, pp. 245–248, 1949.

[44] Y. L. Lu, L. J. Chen, G. Y. Wang, M. L. Benson, P. K. Liaw, S. A. Thompson, J. W. Blust, P. F. Browning, A. K. Bhattacharya, J. M. Aurrecoechea, and D. L. Klarstrom, “HOLD-TIME EFFECTS ON LOW-CYCLE-FATIGUE BEHAVIOR OF HASTELLOY® X SUPERALLOY AT HIGH TEMPERATURES,” *Mater. Sci.*, 2004.

[45] Y. Lu, “High-temperature low-cycle-fatigue and crack-growth behaviors of three superalloys: HASTELLOY X, HAYNES 230, and HAYNES 188,” 2005.

[46] H. Suzuki, T. Iseki, and Y. Shoda, “High-Temperature Low-Cycle Fatigue Tests on Hastelloy X,” *J. Nucl. Sci. Technol.*, vol. 14, no. 5, pp. 381–386, 1977.

[47] J. C. Zhao, M. Larsen, and V. Ravikumar, “Phase precipitation and time-temperature-transformation diagram of Hastelloy X,” *Mater. Sci. Eng. A*, vol. 293, no. 1, pp. 112–119, 2000.

[48] H. U. Hong, I. S. Kim, B. G. Choi, H. W. Jeong, and C. Y. Jo, “Effects of temperature and strain range on fatigue cracking behavior in Hastelloy X,” *Mater. Lett.*, vol. 62, pp. 4351–4353, 2008.

[49] M. A. Arkoosh, “Elevated temperature ductility minimum in Hastelloy alloy X,” *Metall. Mater. Trans. A*, vol. 3, no. 8, pp. 2235–2240, 1972.

[50] M. Calmunger, *High-Temperature Behaviour of Austenitic Alloys, Influence of temperature and strain rate on mechanical properties and microstructural development*, no. 1619. 2013.

[51] R. Plaut, C. Herrera, and D. Escriba, “A short review on wrought austenitic stainless steels at high temperatures: processing, microstructure, properties and performance,” *Mater. …*, vol. 10, no. 4, pp. 453–460, 2007.

[52] “MatWebMaterial Property Data.” [Online]. Available: http://www.matweb.com/search/datasheet.aspx?MatGUID=4e35f212628b4157ab10f943169e1423.

[53] Y. Hosoi, “Introduction to stainless steel.,” *J. Japan Inst. Light Met.*, vol. 37, no. 9, pp. 624–635, 1987.

[54] I. Nikulin, R. Kaibyshev, and V. Skorobogatykh, “High temperature properties of an austenitic stainless steel,” *J. Phys. Conf. Ser.*, vol. 240, p. 012071, 2010.

[55] J. Erneman, M. Schwind, H. O. Andrén, J. O. Nilsson, a. Wilson, and J. Ågren, “The evolution of primary and secondary niobium carbonitrides in AISI 347 stainless steel during manufacturing and long-term ageing,” *Acta Mater.*, vol. 54, no. 1, pp. 67–76, 2006.

[56] I. Finnie, “Some observations on the erosion of ductile metals,” *Wear*, vol. 19, no. 1, pp. 81–90, 1972.

[57] G. Sundararajan and M. Roy, “Solid particle erosion behaviour of metallic materials at room and elevated temperatures,” *Tribol. Int.*, vol. 30, no. 5, pp. 339–359, 1997.

[58] Y. I. Oka, H. Ohnogi, T. Hosokawa, and M. Matsumura, “The impact angle dependence of erosion damage caused by solid particle impact,” *Wear*, vol. 203–204, pp. 573–579, 1997.

[59] S. Bahadur and R. Badruddin, “Erodent particle characterization and the effect of particle size and shape on erosion,” *Wear*, vol. 138, no. 1–2, pp. 189–208, 1990.

[60] A. Misra and I. Finnie, “On the size effect in abrasive and erosive wear,” *Wear*, vol. 65, no. 3, pp. 359–373, 1981.

[61] M. Liebhard and A. Levy, “The effect of erodent particle characteristics on the erosion of metals,” *Wear*, vol. 151, no. 2, pp. 381–390, 1991.

[62] N. Gat and W. Tabakoff, “Some effects of temperature on the erosion of metals,” *Wear*, vol. 50, no. 1, pp. 85–94, 1978.

[63] I. M. Hutchings and a. V. Levy, “Thermal effects in the erosion of ductile metals,” *Wear*, vol. 131, no. 1, pp. 105–121, 1989.

[64] “Fatigue,” in *Elements of Metallurgy and Engineering Alloys*, 2008, pp. 243–265.

[65] X. Chen and J. W. Hutchinson, “Particle impact on metal substrates with application to foreign object damage to aircraft engines,” *J. Mech. Phys. Solids*, vol. 50, no. 12, pp. 2669–2690, 2002.

[66] J. O. Peters, B. L. Boyce, a. W. Thompson, R. O. Ritchie, and O. Roder, “Role of foreign-object damage on thresholds for high-cycle fatigue in Ti-6Al-4V,” *Metall. Mater. Trans. A*, vol. 31, no. 6, pp. 1571–1583, 2000.

[67] X. Chen and J. W. Hutchinson, “Foreign object damage and fatigue crack threshold: Cracking outside shadow indents,” *Int. J. Fract.*, vol. 107, no. 1, pp. 31–51, 2001.

[68] J. O. Peters, B. L. Boyce, X. Chen, J. M. McNaney, J. W. Hutchinson, and R. O. Ritchie, “On the application of the Kitagawa-Takahashi diagram to foreign-object damage and high-cycle fatigue,” *Eng. Fract. Mech.*, vol. 69, no. 13, pp. 1425–1446, 2002.

[69] M. D. Chapetti, “On fatigue behavior of small cracks induced by foreign-object damage in ti-6al-4 v,” *Icf11*, no. 1, pp. 4–9, 2005.

[70] J. O. Peters and R. O. Ritchie, “Foreign-object damage and high-cycle fatigue : role of microstructure in Ti – 6Al – 4V,” vol. 23, pp. 413–421, 2001.

[71] P. Duó, J. Liu, D. Dini, M. Golshan, and a. M. Korsunsky, “Evaluation and analysis of residual stresses due to foreign object damage,” *Mech. Mater.*, vol. 39, no. 3, pp. 199–211, 2007.

[72] J. Ding, R. F. Hall, J. Byrne, and J. Tong, “Fatigue crack growth from foreign object damage under combined low and high cycle loading. Part I: Experimental studies,” *Int. J. Fatigue*, vol. 29, no. 7, pp. 1339–1349, 2007.

[73] T. Nicholas, S. R. Thompson, W. J. Porter, and D. J. Buchanan, “Comparison of fatigue limit strength of Ti-6Al-4V in tension and torsion after real and simulated foreign object damage,” *Int. J. Fatigue*, vol. 27, no. 10–12, pp. 1637–1643, 2005.

[74] X. Chen, “Foreign object damage on the leading edge of a thin blade,” *Mech. Mater.*, vol. 37, pp. 447–457, 2005.

[75] R. Pandey and M. Deshmukh, “Shot peening and its impact on fatigue life of engineering componets,” *Int. Conf. Shot Peen. Blast Clean.*, no. i, pp. 1–20, 2001.

[76] A. Niku-Lari and IITT.France, “An overview of Shot Peening,” *Intl Conf Shot Peen. Blast Clean.*, pp. 1–25, 1996.

[77] E. R. de los Rios, A. Walley, M. T. Milan, and G. Hammersley, “Fatigue crack initiation and propagation on shot-peened surfaces in A316 stainless steel,” *Int. J. Fatigue*, vol. 17, no. 7, pp. 493–499, 1995.

[78] B. J. Foss, S. Gray, M. C. Hardy, S. Stekovic, D. S. McPhail, and B. A. Shollock, “Analysis of shot-peening and residual stress relaxation in the nickel-based superalloy RR1000,” *Acta Mater.*, vol. 61, no. 7, pp. 2548–2559, 2013.

[79] H. Lim, “Microstructural Explicit Simulation of Grain Boundary Diffusion in Depleted UO2,” 2011.

[80] J. Heath, “Energy Dispersive Spectroscopy,” 2015.

[81] University of California, “Introduction to Energy Dispersive X-ray Spectrometry (EDS),” pp. 1–12, 2015.

[82] B. L. Dutrow, “X-ray Powder Diffraction (XRD).” [Online]. Available: http://serc.carleton.edu/research_education/geochemsheets/techniques/XRD.html.

[83] M. Birkholz, *Thin Film Analysis by X-Ray Scattering*. 2006.

[84] “Bragg ’ s Law,” *Production*, vol. 5, no. 6, pp. 371–372, 1970.

[85] “Powder X-ray Diffraction.” [Online]. Available: http://chem.libretexts.org/Core/Analytical_Chemistry/Instrumental_Analysis/Diffraction/Powder_X-ray_Diffraction.

[86] Standard Test Method for Conducting Elevated Temperature Erosion Tests by Solid Particle Impingement Using Gas Jets, *ASTM Int.* pp. 1–15, 2015.

[87] Standard Test Method for Conducting Erosion Tests by Solid Particle Impingement Using Gas Jets 1, *ASTM Int.* pp. 1–6, 2015.

[88] H. Bernier, “Scaling and Designing Large-Bore Two-Stage High Velocity Guns,” in *High-pressure Shock Compression of Solids VIII: The Science and Technology of High-velocity Impact*, 2005, pp. 37–83.

[89] Standard Test Method for Microindentation Hardness of Materials, *ASTM Int.*, pp. 1–24, 2015.

[90] Sengupta, “Design for finite life.”

[91] M. M. M. K.Gopinath, “MAchine design II.”

[92] M. F. Ashby, “A first report on deformation-mechanism maps,” *Acta Metall.*, vol. 20, no. 7, pp. 887–897, 1972.

[93] R. K. Cheng, “Ultra-Clean Low-Swirl Burner for Heating and Power Systems What ’ s Special About Low-swirl Burner ?”

[94] “Obrazek.” [Online]. Available: https://www.sekogroup.com/en/our-products/power-generation/.

[95] E. Sánchez-González, P. Miranda, J. J. Meléndez-Martínez, F. Guiberteau, and A. Pajares, “Temperature dependence of mechanical properties of alumina up to the onset of creep,” *J. Eur. Ceram. Soc.*, vol. 27, no. 11, pp. 3345–3349, 2007.

[96] W. Blum, Y. J. Li, J. Chen, X. H. Zeng, and K. Lu, “On the Hall Petch relation between fow stress and grain site,” *Int. J. Mater. Res.*, vol. 97, no. 12, pp. 1661–1666, 2006.

[97] I. Finnie, “Some reflections on the past and future of erosion,” *Wear*, vol. 186–187, pp. 1–10, 1995.

[98] W. G. Kim, S. N. Yin, W. S. Ryu, J. H. Chang, and S. J. Kim, “Tension and creep design stresses of the ‘Hastelloy-X’ alloy for high-temperature gas cooled reactors,” *Mater. Sci. Eng. A*, vol. 483–484, no. 1–2 C, pp. 495–497, 2008.

[99] “ATI-SS 347 Technical Data Sheet,” vol. 3942, no. September 2005, pp. 3–11, 2013.

[100] T. Sakthivel, K. Laha, M. Nandagopal, K. S. Chandravathi, P. Parameswaran, S. Panneer Selvi, M. D. Mathew, and S. K. Mannan, “Effect of temperature and strain rate on serrated flow behaviour of Hastelloy X,” *Mater. Sci. Eng. A*, vol. 534, pp. 580–587, 2012.

[101] S.G. Hong and S.B. Lee, “The tensile and low-cycle fatigue behavior of cold worked 316L stainless steel: influence of dynamic strain aging,” *Int. J. Fatigue*, vol. 26, no. 8, pp. 899–910, 2004.

[102] R.Koterazawa, “Fractographic Study of Fatigue Crack Propagation,” *Trans. ASME*, 1973.

[103] D. E. Duvall, “Modes of fracture,” in *ASM handbook*, vol. 12, 2002, pp. 12–71.

[104] T. Zhai, A. J. Wilkinson, and J. W. Martin, “Crystallographic mechanism for fatigue crack propagation through grain boundaries,” *Acta Mater.*, vol. 48, no. 20, pp. 4917–4927, 2000.

[105] A. P. V. Kerline, “Fracture Modes,” in *ASM handbook*, vol. 12, 2010, pp. 12–71.

[106] A. Makas, J. Avallone, R. MacKinnon, I. Atodaria, and P. Peralta, “Variability on nucleation and growth of short fatigue cracks due to material anisotropy in aluminum 2024-T351,” *J. Intell. Mater. Syst. Struct.*, vol. 24, no. 17, p. 1045389X12468218, 2012.

[107] J. Peters and R. Ritchie, “Influence of foreign-object damage on crack initiation and early crack growth during high-cycle fatigue of Ti–6Al–4V,” *Eng. Fract. Mech.*, vol. 67, no. 3, pp. 193–207, 2000.

APPENDIX A

DOGBONE SPECIMEN POLISHING PROCEDURE USING SHERLINE END MILL

The following steps describes the procedure for polishing dog-bones(rectangular cross section) specimen using Sherline CNC End mill. It is advised to the first time user to read the instruction manual for Sherline CNC End Mill and Sherline software.

1) Collect all the necessary things required for polishing such as spring loaded tool attached with a small disc, polishing paper, polishing cloth/pad, water, alumina, colloidal silica, etc. If possible cover the metallic parts and the screw shown in figure A.1 with a plastic film or bag for preventing corrosion due to water.

2) Mark the mid-point of the gauge length and secure the specimen into the vise as shown in figure A.1 and ensure it is flat using dial indicator.

3) Mount the spring loaded tool into the spindle of the machine after attaching polishing paper to the disc as shown in the figure A.2 adjust X,Y and Z-axis to align center of the tool and the mid-point of the gauge length, then using Y-axis keep 0.2 inch distance between the edge of the specimen and the hole on the tool as shown in figure A.2. This will be the starting position, Z-axis can be used to adjust force being applied on the specimen. Place a container below the specimen to collect water. It is advised to start with very coarse paper e.g. 80 grit size if the sample surface is very rough or 240 grit size if the sample surface is moderately rough.

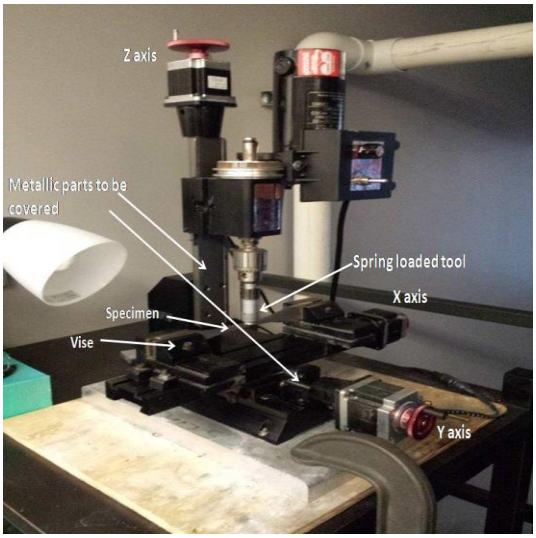

Figure A.1 Sherline CNC end mill

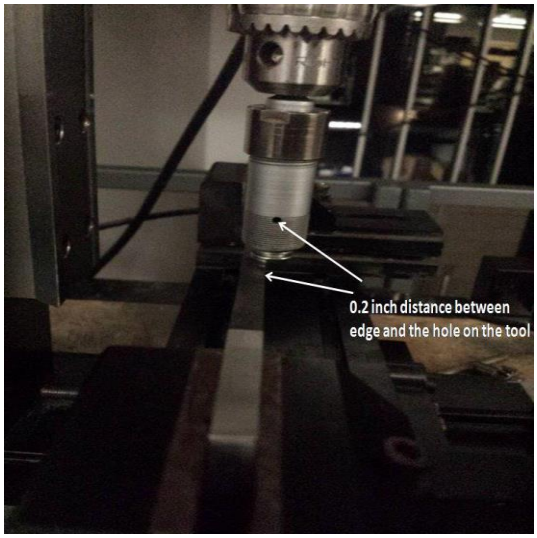

Figure A.2 Starting position for polishing

3) Open the Sherline CNC software and panel screen will appear as shown in figure A.3

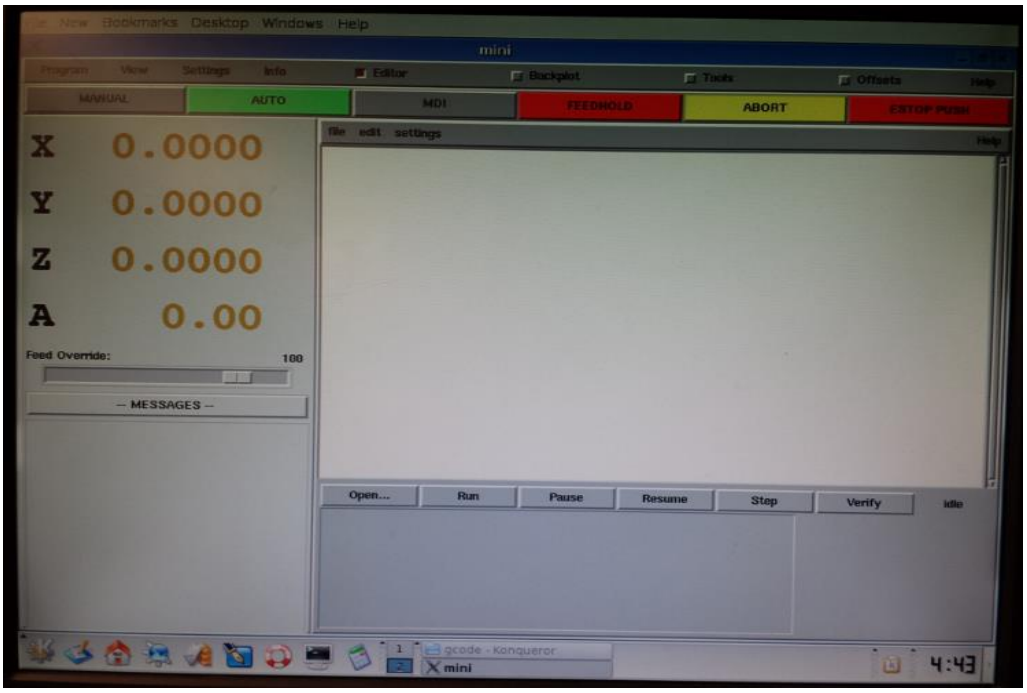

Figure A.3 Control panel screen

4) Go to "Editor" where a code can be written in the blank screen. One such example of the code is given below:

```
%
g01 g20 g40 g49 g90 f2
#1=1
o300 do
g01 x0.25 y0 z0 f10
g01 x0.25 y0.2625 z0 f10
g01 x-0.25 y0.2625 z0 f10
g01 x-0.25 y0.3875 z0 f10
g01 x0.25 y0.3875 z0 f10
g01 x0.25 y0.65 z0 f10
g01 x-0.25 y0.65 z0 f10
g01 x-0.25 y0.3875 z0 f10
g01 x0.25 y0.3875 z0 f10
g01 x0.25 y0.2625 z0 f10
g01 x-0.25 y0.2625 z0 f10
g01 x-0.25 y0 z0 f10
g01 x0 y0 z0 f10
#1=[#1-1]
o300 while [#1 GT 0]
%
```

5) Click file>Save and Load which loads the code and will be shown at the bottom of the screen, then turn on the motors for the X, Y and Z-axis using the toggle on/off switch.

6) Ensure X, Y and Z axis are set to zero on the left side of the screen. Click "AUTO" and then "Run", once the cycle starts turn on the spindle which rotates the spring loaded tool. This will start the polishing cycle, use water as required. This code performs one cycle and can be repeated as many time as required or the number written in the green can be changed to perform the desired number of cycles. Depending upon the length and width of the specimen to be polished the starting position of the tool and the code written in the red color can be changed by changing the X and Y co-ordinates.

7) The path or the pattern followed by the tool for polishing can be seen by clicking on "Backplot".

8) Once the surface has uniform scratches repeat the polishing cycles with lower grit size papers e.g., 600, 800, 1200. If further polishing is required, the cycles can be repeated using polishing pad with alumina, colloidal silica and diamond paste.

9) Repeat the same polishing steps for all the remaining sides.

10) Remove the sample after polishing, turn off the motors, clean the specimen and the machine after use, also apply lubricant to the metal parts where there are chances of water getting sprayed.

Suggestion:

- If the polishing paper comes off the disc anytime during the polishing cycle is running, click "Pause"/turn off the spindle rotation, raise the Z-axis using "Manual" mode, attach new polishing paper and bring Z-axis down to the position from where it was raised and click "Resume" to save time or the cycle can be abandoned to begin new cycle with X, Y and Z-axis set to starting position after attaching new polishing paper.